

Current Awareness Bulletin

of

SCHOLARLY ARTICLES PUBLISHED

BY

Faculty, Students and Alumni

~ January 2012 ~

DELHI TECHNOLOGICAL UNIVERSITY CENTRAL LIBRARY
(formerly Delhi College of Engineering, Bawana Road, DELHI)

PREFACE

This is the first Current Awareness Bulletin Service started by Delhi Technological University Library. The aim of the bulletin is to compile, preserve and disseminate information published by the Faculty, Students and Alumni for mutual benefits. The bulletin also aims to propagate the intellectual contribution of DTU as a whole to the academia. It contains information resources available in the internet in the form of articles, reports, presentation published in international journals, websites, etc. by the faculty and students of Delhi Technological University in the field of science and technology. The publication of Faculty and Students which are not covered in this bulletin may be because of the reason that either the full text was not accessible or could not be searched by the search engine used by the library for this purpose. To make the bulletin more comprehensive, the learned faculty and Students may provide their uncovered publication to the library either through email or in CD, etc.

This issue contains the information published during January 2012. The arrangement of the contents is alphabetical wise starting from A-Z. The Full text of the article which is either subscribed by the University or available in the web has been provided in this Bulletin.

CONTENTS

1. A Novel bacterial foraging technique for edge detection by **Om Prakash Verma, *Madasu Hanmandlu*, Puneet Kumar, **Sidharth Chhabra, *Akhil Jindal*
2. Emergent universe with scalar (or tachyonic) field in higher derivative theory
**C.P.Singh, *Vijay Singh*
3. Flow-based load-balancing architecture for the angle all-photonic network by
Imad Khazali and *#Anjali Agarwal*
4. FRW models with particle creation in Brans-Dicke theory by *C.P.Singh*
5. Fuzzy Approach to Nodal Reliability Ranking for radial Distribution Systems
by *#Roma Raina* and *#Mini Thomas*
6. Investigation of insecticidal activity of some α,β -unsaturated carbonyl
compounds and their synergistic combination with natural products against
phenacoccus solenopsis tinsley by Archana Rani, **Sapna Jain* and Ram Das
Gautam.
7. Power-Law Expansion and Scalar Field Cosmology in Higher Derivative
Theory by **C.P.Singh and *Vijay Singh*
8. Studies of Novel Chain Linked Biodegradable Polymers by **A.P.Gupta,*
**Anushu Dev and *Vimal Kumar*

*Faculty
#Alumni



A novel bacterial foraging technique for edge detection

Om Prakash Verma^{a,*}, Madasu Hanmandlu^b, Puneet Kumar^c, Sidharth Chhabra^a, Akhil Jindal^a

^a Delhi Technological University (Formerly Delhi College of Engineering), Delhi, India

^b Department of Electrical Engineering, IIT Delhi, Delhi, India

^c Advanced Systems Laboratory, Hyderabad, India

ARTICLE INFO

Article history:

Received 11 February 2010

Available online 12 March 2011

Communicated by H.H.S. Ip

Keywords:

Ant Colony System

Bacterial foraging

Derivative

Direction probability matrix

Edge detection

ABSTRACT

A new approach for edge detection using a combination of bacterial foraging algorithm (BFA) and probabilistic derivative technique derived from Ant Colony Systems, is presented in this paper. The foraging behavior of some species of bacteria like *Escherichia coli* can be hypothetically modeled as an optimization process. A group of bacteria search for nutrients in a way that maximizes the energy obtained per unit time spent during the foraging. The proposed approach aims at driving the bacteria through the edge pixels. The direction of movement of the bacteria is found using a direction probability matrix, computed using derivatives along the possible directions. Rules defining the derivatives are devised to ensure that the variation of intensity due to noise is discarded. Quantitative analysis of the feasibility of the proposed approach and its comparison with other standard edge detection operators in terms of kappa and entropy are given. The effect of initial values of parameters of BFA on the edge detection is discussed.

© 2011 Elsevier B.V. All rights reserved.

1. Introduction

Detection of edges in an image is a very important step for the image understanding. Indeed, high-level processing tasks such as image segmentation and object recognition, etc. directly depend on the quality of the edges detected. Moreover, the generation of an accurate edge map becomes a very critical issue when the images are corrupted by noise.

Edges in an image are marked with discontinuity or significant variation in intensity or gray levels. The methods of identifying the intensity discontinuity associated with edges in an image are normally based on the calculation of the intensity gradient in the whole image. The underlying idea of most edge detection techniques is the computation of a local first or second derivative operator, followed by some regularization technique to reduce the effects of noise.

Canny's method (Canny, 1986) for the edge detection counters the noise problems, wherein an image is convolved with the first-order derivatives of Gaussian filter for smoothing in the local gradient direction followed by the edge detection using thresholding. Marr and Hildreth (1980) propose an algorithm that finds edges at the zero-crossings of the image Laplacian. Non-linear filtering techniques for edge detection also have witnessed much advancement through the SUSAN method (Smith and Brady, 1997), which works by associating a small area of neighboring pixels with similar brightness to each center pixel. Existing edge

detectors like Gradient operator and the Laplacian Operator are based on the assumption that edges in the images are step functions in intensity. Prewitt detector (Raman and Sobel, 2006) uses the local gradient operators which only detect edges having certain orientations and perform poorly on blurred or noisy images. Different algorithms for the fuzzy based edge detection are proposed in Cheung and Chan (1995), Kuo et al. (1997), Russo (1998), El-Khamy and S. (2000). Abdallah and Ayman (2009) introduce a fuzzy logic reasoning strategy for the edge detection in the digital images without determining a threshold.

Most of the existing operators are confronted with a huge search space for the detection of edges. Considering an image of size 1024 by 1024 pixels, the required solution space is of the order of $2^{1024 \times 1024}$. Therefore the task of edge detection is time consuming and memory exhausting without the optimization.

A novel bacterial-derivative based algorithm that exploits the foraging behavior of bacteria to collectively detect edges in an image is developed in Passino (2002), Liu and Passino (2002). Bacterial foraging optimization algorithm (BFAO) has already been applied in the optimal control engineering, harmonic estimation (Mishra, 2005), transmission loss reduction (Tripathy et al., 2006), machine learning (Kim and Cho, 2005), active power filter design (Mishra and Bhende, 2007), color image enhancement (Hanmandlu et al., 2009), etc.

Bacteria foraging is an optimization process where bacteria seek to maximize the energy by eating up as many nutrients as they can. Nutrients in our case correspond to tracing the edge pixels. Bacteria move by either tumbling or swimming. In the classical approach, the direction of movement is decided randomly while

* Corresponding author. Tel.: +91 1127294672; fax: +91 1127871023.

E-mail addresses: opverma@dce.ac.in, opverma.dce@gmail.com (O.P. Verma).

tumbling and every direction is equally preferred. In our method, a probabilistic approach, inherited from Ant Colony System (Dorigo and Gambardella, 1997; Verma et al., 2009), is used. This causes the bacterium to move along the direction, where the probability of finding a nutrient (edge) is highest. The proposed algorithm also distinguishes between the local variations due to noise and image structures, using a derivative. Another important characteristic of bacteria's life cycle is swarming. In our approach, swarming is not only dependent upon other bacteria's positions but also on the clique of its current position.

The proposed approach is well suited to address the uncertainty introduced while extracting the edge information from the image data. The innovative aspect of this approach lies in the development of a noise-protected operator that combines the rules framed for the noise cancellation and edge detection in the same structure. The application of modified bacterial foraging in combination with a derivative approach leads to a minimal set of input data to be processed thus making the process faster and memory-efficient. As a result, the proposed approach outperforms the existing state-of-the-art techniques.

The paper is organized as follows: In Section 2 a brief introduction to bacterial foraging technique is provided to present the basic idea. A modification of this technique is discussed in Section 3. Section 4 presents the probabilistic derivative approach to find the direction of movement of a bacterium. An algorithm for the edge detection along with the pseudo code is developed in Section 5. Section 6 gives the experimental results followed by the conclusions in Section 7.

2. Bacterial foraging technique

A new evolutionary technique, called bacterial foraging scheme appeared in Passino (2002), Liu and Passino (2002). Foraging can be modeled as an optimization process where bacteria seek to maximize the energy obtained per unit time spent during foraging. In this scheme, an objective function is posed as the effort or a cost incurred by the bacteria in search of food. A set of bacteria tries to reach an optimum cost by following four stages: Chemo taxis, swarming, reproduction, and elimination and dispersal. To start with, there will be as many solutions as the number of bacteria. So, each bacterium produces a solution iteratively for a set of optimal values of parameters. Gradually all the bacteria converge to the global optimum.

In the chemo taxis stage, the bacteria either resort to a tumble followed by a tumble or make a tumble followed by a run or swim. This is the movement stage of bacteria accomplished through swimming and tumbling. On the other hand, in swarming, each *Escherichia coli* bacterium signals another bacterium via attractants to swarm together. This is basically the cell to cell signaling stage. Furthermore, in the reproduction the least healthy bacteria die and of the healthiest, each bacterium splits into two bacteria, which are placed at the same location. While in the elimination and dispersal stage, any bacterium from the total set can be either eliminated or dispersed to a random location during the optimization. This stage prevents the bacteria from attaining the local optimum.

Let θ be the position of a bacterium and $J(\theta)$ be the value of the objective function, then the conditions $J(\theta) < 0$, $J(\theta) = 0$, and $J(\theta) > 0$ indicate whether the bacterium at location θ is in nutrient-rich, neutral, and noxious environments, respectively. Basically, chemo taxis is a foraging behavior that implements a type of optimization where bacteria try to climb up the nutrient concentration (find the lower values of $J(\theta)$), avoid noxious substances, and search for ways out of neutral media (avoid being at positions θ where $J(\theta) \geq 0$). This is just like a type of biased random walk.

3. The modified bacterial foraging technique for edge detection

The original bacterial foraging (BF) technique Liu and Passino (2002) is now modified to make it suitable for the edge detection. The nutrient concentration at each position, i.e. the cost function is calculated using a derivative approach. The implications in lieu of modifications of the technique for the edge detection are furnished here.

3.1. Search space

The 2-dimensional search space for bacteria consists of the x and y -coordinates (i.e. discrete values) of a pixel in an image. Being limited by the image dimensions, i.e. horizontal and vertical pixels of the image, the search space is finite.

3.2. Chemotaxis

This is a very important stage of BF. It decides the direction in which the bacterium should move. Depending upon the rotation of the flagella, each bacterium decides whether it should swim (move in a predefined direction) or tumble (move in an altogether different direction). Our goal is to let the bacterium search for the edge pixels in an image. Another important goal is to keep the bacterium away from the noisy pixels.

As we are dealing with 2D discrete values of coordinates in an image with 8-connectivity of the neighborhood pixels, the probable directions to move for a bacterium from a particular pixel are: E, W, N, S, NE, SE, NW, SW. Out of these eight directions the bacterium of interest has to decide one direction that lead to an edge pixel but not a noisy pixel. A probabilistic derivative approach is used to find out the direction (one out of the eight possible directions) most suitable to hit upon an edge and to cut off the directions leading to noise. This is a major deviation in the chemotaxis step of BFA where the bacteria either tumble in a random direction or swim in the same direction as in the previous step. This is elaborated here.

Let $\theta^i(j, k, l)$ represent the position of the i th bacterium at j th chemotactic, k th reproductive and l th elimination-dispersal step. A pixel position in an image can be represented by the x and y -coordinates of the bacterium. So let $\theta^i(j, k, l)$ be the position of a bacterium in an array $\phi[m, n, i, j, k, l]$ where m, n represent the x - y coordinates of the bacterium.

The initial positions of the bacteria are selected randomly. They move on to the edge pixels during the run of the algorithm. The path is recorded only after a certain number of steps made by each bacterium.

The movement of the bacterium may be represented by

$$\theta^i(j+1, k, l) = \phi[m', n', i, j+1, k, l], \quad (1)$$

where m', n' are the coordinates to which the bacterium should move in order to reach the edge pixel by avoiding the noisy pixels. During the tumble, the direction is determined from

$$\theta^i(j+1, k, l) = \theta^i(j, k, l) + \frac{C(i) \cdot \Delta(i)}{\sqrt{\Delta(i)^T \Delta(i)}} \quad (2)$$

where $\Delta(i)$ indicates a random number in \mathbb{R}^2 and $C(i)$ is the length of a step size.

The above approach is modified to include a probabilistic derivative as explained in detail in Section 4.

3.3. Swarming

It is assumed that a bacterium relies on other bacteria. This property of bacterium is exploited here. In this step, the bacterium that has searched an optimum path, signals other bacteria so that

they can together reach the desired optimum path swiftly. As each bacterium moves, it releases an attractant to signal other bacteria to swarm towards it. Also, each bacterium releases a repellent to warn other bacteria by keeping a safe distance from them. Because of this, bacteria congregate into groups and move in a concentric pattern. This is achieved by using a cell to cell signaling function which combines both the attraction and repelling effects. Thus we have

$$J_{cc}(\theta^i(j, k, l), \theta(j, k, l)) = \sum_{t=1}^s j_{cc}^t(\theta^i, \theta^t) \\ = \sum_{t=1}^s \left[-d_{att} \exp \left(-w_{att} \sum_{m=1}^P (\theta_m^i - \theta_m^t)^2 \right) \right] \\ + \sum_{t=1}^s \left[h_{rep} \exp \left(-w_{rep} \sum_{m=1}^P (\theta_m^i - \theta_m^t)^2 \right) \right] \quad (3)$$

where θ^i is the location of i th bacterium, P is the number of dimensions of the optimization domain (here, $P = 2$), $\theta = \{\theta^i | i = 1, \dots, S\}$ represents the positions of the i th bacteria, θ_m^i is the m th component of θ^i , d_{att} is the measure of how much attractant is released, w_{att} is the diffusion rate, h_{rep} and w_{rep} are the magnitude and width of the repelling effect. Empirically, $d_{att} = 0.1$, $w_{att} = 0.2$, $h_{rep} = 0.1$, $w_{rep} = 10$ are found to be optimal.

It may be noted from Eq. (3) that this is basically a function of distance of the bacterium under consideration from all other bacteria. This function is now modified to make it dependent on the clique of the position (pixel) of the bacterium and its distance from other bacteria.

$$J_{cc}(\theta^i(j, k, l), \theta(j, k, l)) = f(\text{distance}) + f(\text{clique}) \quad (4)$$

The clique is defined as the local group of pixels around the pixel of interest. It is represented as

$$f(\text{clique}) = \mu \Delta_{\theta^i} \quad (5)$$

where μ is a constant (i.e. 1). This is introduced to make the value of cell to cell signaling function negative as the bacterium reaches an edge pixel, and Δ_{θ^i} is the function that uses the local intensity difference statistic at the pixel location given by $\theta^i \cdot \Delta_{\theta^i}$:

$$\Delta_{\theta^i} = \frac{V_c(I_{\theta^i})}{Z} \quad (6)$$

where, I_{θ^i} represents the pixel of interest in the image. If the pixel location is at (m, n) then

$$V_c(I_{\theta^i}) = V_c(I_{m,n}) |I_{m-2,n-1} - I_{m+2,n+1}| + |I_{m-2,n+1} - I_{m+2,n-1}| \\ + |I_{m-1,n-2} - I_{m+1,n+2}| + |I_{m-1,n+1} - I_{m+1,n+1}| \\ + |I_{m-1,n} - I_{m+1,n}| + |I_{m-1,n+1} - I_{m+1,n-1}| \\ + |I_{m-1,n+1} - I_{m+1,n-2}| + |I_{m,n-1} - I_{m,n+1}| \quad (7)$$

and Z is the normalization factor defined as

$$Z = \sum_{m=1:M} \sum_{n=1:N} V_c(I_{m,n}) \quad (8)$$

The modified form of cell to cell signaling for edge detection may be represented as

$$J_{cc}(\theta^i(j, k, l), \theta(j, k, l)) = \sum_{t=1}^s j_{cc}^t(\theta^i, \theta^t) \\ = \sum_{t=1}^s \left[-d_{att} \exp \left(-w_{att} \sum_{m=1}^P (\theta_m^i - \theta_m^t)^2 \right) \right] \\ + \sum_{t=1}^s \left[h_{rep} \exp \left(-w_{rep} \sum_{m=1}^P (\theta_m^i - \theta_m^t)^2 \right) \right] \\ - \mu \frac{V_c(I_{\theta^i})}{Z} \quad (9)$$

$J_{cc}(\theta^i(j, k, l), \theta(j, k, l))$ has its initial value the derivative at the pixel given by $\theta^i(j, k, l)$. The calculation of the derivative at a pixel (x, y) is explained in Section 4.1.

3.4. Reproduction step

After N_c chemotactic steps, a reproduction step begins its loop. Let N_{re} be the number of reproduction steps. For convenience, we assume that the number of bacteria S is a positive even integer. We choose

$$S_r = \frac{S}{2} \quad (10)$$

as the number of population members having sufficient nutrients so that they will reproduce (split up into two) with no mutations. For reproduction, the population is sorted in the ascending order of the accumulated cost (the higher cost indicates that a bacterium has not got as many nutrients during its lifetime of foraging and hence is not “healthy” and thus unlikely to reproduce); then the least healthy bacteria S_r die and each of the other healthiest bacteria S_r split up into two, which are placed at the same location. This method rewards bacteria that have encountered a lot of nutrients and allows us maintain a constant population size.

3.5. Elimination step

Let N_{ed} be the number of elimination-dispersal events and each bacterium in the population is subjected to elimination-dispersal with a probability P_{ed} . We assume that the frequency of chemotactic steps is greater than the frequency of reproduction steps, which is in turn greater than the frequency of elimination-dispersal events (e.g. a bacterium will take many chemotactic steps before reproduction, and several generations may take place before an elimination-dispersal event).

4. Finding the direction of movement using probabilistic derivative approach

4.1. Computing derivative value for a pixel

The procedure to find the nutrient concentration as well as the suitable direction in which the bacterium should move in order to find the edge pixels is now explained. The common feature between an erroneous pixel and a real edge pixel is that the intensity difference around both the pixels is high. It is very important to differentiate them properly in case the image is noisy; hence a derivative based approach is used. This restrains the bacterium from moving towards the noisy pixels.

Consider the neighborhood of a pixel (x, y) in Fig. 1(a). We consider positive X-axis as vertical downward and positive Y-axis as horizontal right side. A derivative at the central pixel position (x, y) in the direction D ($D = \{NW, W, SW, S, SE, E, NE, N\}$) is defined as the difference between the pixel of interest and its neighbor in the corresponding direction.

For example, the derivative at a pixel (x, y) in the north-west direction is given by

$$\partial_{(x,y)}^{NW} = I(x-1, y-1) - I(x, y) \quad (11)$$

where $I(x, y)$ is the intensity at pixel (x, y) .

The choice of the derivative is made from the intensities of pixels. Consider an edge passing through the pixel (x, y) in the NE-SW direction as in Fig. 1(b). Since it's an edge it should contain pixels at NE and SW positions as its constituents. Therefore, the derivative

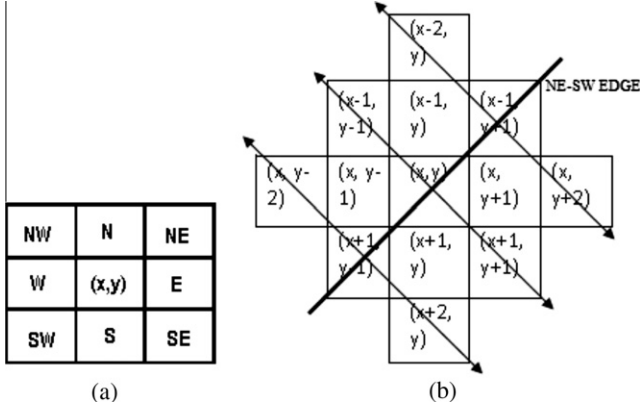


Fig. 1. (a) Pixel (x, y) with its 8-connectivity (b) The pixels to be considered for the edge in NE-SW direction.

values in the direction NW and SE (perpendicular to the edge) for the pixels at positions (x, y) , $(x+1, y-1)$ and $(x-1, y+1)$ should also be high (Verma et al., 2009). This greatly reduces the chances of selecting a noisy pixel. The number of noisy pixels is negligible as compared to the number of edge pixels. Thus, for the pixel (x, y) let ∂_1 be given by

$$\partial_1 = \partial_{(x,y)}^{NW}. \quad (12)$$

Similarly, we have at the neighboring pixels as

$$\partial_2 = \partial_{(x+1,y-1)}^{NW} = I(x+1, y-1) - I(x, y-2) \quad (13)$$

$$\partial_3 = \partial_{(x-1,y+1)}^{NW} = I(x-1, y+1) - I(x-2, y) \quad (14)$$

The average of the above three values can be taken as the net derivative value in NW direction, given by

$$\partial_{avg1} = \frac{(\partial_1 + \partial_2 + \partial_3)}{3} \quad (15)$$

Similarly, we calculate ∂_{avg2} as the average of $\partial_{(x,y)}^{SE}$, $\partial_{(x+1,y-1)}^{SE}$ and $\partial_{(x-1,y+1)}^{SE}$. Having these two net derivatives we are looking for an edge having the intensity difference in one region only. The maximum of these two is the derivative for the edge pixel at (x, y) in the direction NE-SW, denoted by

$$\partial_{NE-SW} = \max(\partial_{avg1}, \partial_{avg2}) \quad (16)$$

Similarly the derivatives along the remaining three directions are: ∂_{NW-SE} , ∂_{N-S} and ∂_{W-E} .

The final derivative at pixel (x, y) which is the maximum of the net derivatives obtained in all the four possible edge directions is:

$$\partial_{x,y} = \max(\partial_{W-E}, \partial_{NW-SE}, \partial_{NE-SW}, \partial_{N-S}) \quad (17)$$

Since our aim is to find the edge pixels, use is made of the observation that larger the value of $\partial_{x,y}$ more is the chance for a bacterium to reach an edge pixel. Therefore, the nutrient concentration at any position, (x, y) should be the function of $\partial_{x,y}$. So we have

$$[\eta_i] = \partial_{(x,y)} \quad (18)$$

Hence, higher the nutrient concentration along an edge more is the movement of bacteria along it.

4.2. Direction probability matrix

The concern here is to locate an edge pixel to which a bacterium should move from a given pixel. To do this we find the values of the derivatives for all the 8 neighborhood pixels around the pixel under consideration in terms of their nutrient concentration. Out of

the eight possible directions the next direction is found out using the transition matrix derived from the Ant Colony System (Dorigo and Gambardella, 1997; Verma et al., 2009).

In an artificial Ant Colony System, developed by imitating the real ant's behavior, ant chooses its next step for its movement depending upon the transition probability matrix which is a function of amount of pheromone discharged by ants on the path and the heuristic factor. The transition probability matrix at position i is given by:

$$\rho_{ij} = \left\{ \frac{([\tau_j(t)]^\alpha)([N_j]^\beta)}{\sum_{j \in allowed_j} ([\tau_j(t)]^\alpha)([N_j]^\beta)} \right\} \quad (19)$$

where, N_j is the heuristic factor, $\tau_j(t)$ is the pheromone concentration that gives the permissible directions in which an ant movement (in our case ant is replaced by bacterium) has to move; α and β are two parameters that control the relative importance of the two main factors: $\tau_j(t)$ and N_j .

In the proposed approach, pheromone concentration and α and β are taken to be unity. The heuristic factor N_j is taken as the nutrient concentration value η_j . Also, from Eq. (18), nutrient concentration is high along the direction of an edge. Thus the probability of movement along the direction $i \rightarrow j$ is calculated from:

$$\rho_{ij} = \left\{ \frac{[\eta_j]}{\sum_{j \in allowed_j} ([\eta_j])} \right\} \quad (20)$$

A random direction is selected for the movement, with ρ_{ij} as the probability of selection of direction $i \rightarrow j$

$$\Delta(k) = \text{rand}(\rho_{ij} \forall j \in allowed_j) \quad (21)$$

where, $\Delta(k)$ is the direction vector for the k th bacterium at position i and $allowed_j$ is the set of possible moves for the bacterium. This random direction gives the direction of movement out of the eight possible directions. Suppose the current location is $[x, y]$, step size is unity and the random direction selected is NW then the next location of bacteria would be $[x-1, y-1]$.

5. The algorithm and pseudo code

5.1. Algorithm

[Step 1] Initialize the parameters n , S , N_c , N_{re} , N_{ed} , P_{ed} , $C(i)$ ($i = 1, 2, \dots, S$), $F(i)$, $\theta^i(1, 1, 1)$, $V_c(I)$, $J(i, 1, 1, 1)$)

where

n : dimension of the search space(2),

S : the number of bacteria in the population,

S_r : bacteria split ratio,

N_c : chemotactic steps,

N_{re} : the number of reproduction steps,

N_{ed} : the number of elimination-dispersal events,

N_s : swim length,

P_{ed} : elimination-dispersal with probability,

$C(i)$: the size of the step taken in the direction specified by the tumble(unit),

$F(i)$: flag bit for each pixel indicating whether it has already been traversed or not,

$V_c(I)$: is the clique matrix for the image I .

$\theta^i(1, 1, 1)$: initial positions of the bacterium selected randomly.

$J(i, 1, 1, 1)$: Initialized derivative value at the pixel given by $\theta^i(1, 1, 1)$.

[Step 2] Elimination-dispersal loop: $l = l + 1$

[Step 3] Chemotaxis loop: $j = j + 1$

- [a] For $i = 1, 2, \dots, S$, take a chemotactic step for bacterium i as follows.
 [b] Compute the fitness function, $J(i, j, k, l)$.

Let, $J(i, j, k, l) = J(i, j, k, l) + J_{cc}(\theta^i(j, k, l), \theta(j, k, l))$ (i.e. add on the cell-to cell attractant–repellant profile to simulate the swarming behavior)

- [c] Tumble: Find the directions of possible movement from the derivative value and compute the direction probability matrix using:

$$\rho_{ij} = \left\{ \frac{[\eta_j]}{\sum_{j \in \text{allowed}_j} ([\eta_j])} \right\}$$

Now select a random direction using Eq. (21) and find the next direction of movement.

- [d] Reproduction loop:

For each possible direction, $k = k + 1$.

- [e] Move: Let

$$\theta^i(j+1, k, l) = \theta^i(j, k, l) + C(i) \frac{\Delta(i)}{\sqrt{\Delta^T(i) \Delta(i)}}$$

This results in a step of size $C(i)$ in the direction of the tumble for bacterium i . In our case Eq. (1) is used where (m', n') is found out using the step size movement along the direction of tumble.

- [f] Compute $J(i, j+1, k, l)$ and let $J(i, j, k, l) = J(i, j, k, l) + J_{cc}(\theta^i(j, k, l), \theta(j, k, l))$
 [g] Swim
 (i) Let $m = 0$ (counter for swim length).
 (ii) While $m < N_s$ (if have not climbed down too long).
 • Let $m = m + 1$.
 • If $J(i, j+1, k, l) > J_{last}$

then update $\theta^i(j+1, k, l)$ as done in step 3(e). Use this $\theta^i(j+1, k, l)$ to compute the new $J(i, j+1, k, l)$ as in step 3[f]

- Else, let $m = m + 1$

- [h] Go to next bacterium $(i+1)$ if $i \neq S$ (i.e., go to [b] to process the next bacterium).
 [Step 4] If $j < N_c$, go to Step 3[e]. In this case, continue chemotaxis, since the life of bacteria is not over.
 [Step 5] Reproduction:
 [a] For each $i = 1, 2, \dots, S$, let

$$J_{health}^i = \sum_{j=1}^{N_{c+1}} J(i, j, k, l)$$

be the health of the bacterium i (a measure of how many nutrients it got over its lifetime and how successful it was at avoiding the noxious substances).

Sort bacteria and chemotactic parameters $C(i)$ in the ascending order of the cost J_{health} (higher cost means lower health). [b] The S_r bacteria with the highest J_{health} values die and the remaining S_r bacteria with the best values split (this process is performed by the copies that are placed at the same location as that of their parents).

[Step 6] If $k < N_{re}$, go to Step 3[e]. This means that the number of specified reproduction steps is not reached, so the next generation of the chemotactic loop is started.

[Step 7] Elimination-dispersal: For $i = 1, 2, \dots, S$, eliminate and disperse each bacterium with probability P_{ed} . This results in the number of bacteria a constant. To do this, if a bacterium is

eliminated, simply disperse one to a random location in the optimization domain. If $l < N$, then go to Step 2; otherwise end.

5.2. Pseudo code

Bacteria_Edge (Image I)
 FOR each pixel in I

$$V_c(I_{m,n}) = |I_{m-2,n-1} - I_{m+2,n+1}| + |I_{m-2,n+1} - I_{m+2,n-1}| \\ + |I_{m-1,n-2} - I_{m+1,n+2}| + |I_{m-1,n-1} - I_{m+1,n+1}| \\ + |I_{m-1,n} - I_{m+1,n}| + |I_{m-1,n+1} - I_{m-1,n-1}| \\ + |I_{m-1,n+1} - I_{m-1,n-2}| + |I_{m,n-1} - I_{m,n+1}|$$

FOR (each bacterium $i = 1:S$)

$\theta^i(1, 1, 1) = \text{rand_post}()$

$J(i, 1, 1, 1) = \text{derivative_value}(\theta^i(1, 1, 1))$

END FOR

FOR (elimination-dispersal loop $l = 1:N_{ed}$)

FOR (reproduction-loop $k = 1:N_{re}$)

FOR (chemotactic-loop $j = 1:N_c$)

FOR (each bacterium $i = 1:S$)

Calculate

$J(i, j, k, l) = J(i, j, k, l) + J_{cc}(\theta^i(j, k, l), \theta(j, k, l))$

Set $J_{last} = J(i, j, k, l)$

Tumble:

Find the direction of possible movement from the direction probability matrix.

Move:

$\theta^i(j+1, k, l) = \varphi[m', n', i, j+1, k, l]$

Compute $J(i, j+1, k, l)$

$m = 0$

WHILE ($m < N_s$)

$m = m + 1$

IF ($J(i, j+1, k, l) < J_{last}$)

$J_{last} = J(i, j+1, k, l)$

Update $\theta(i, j+1, k, l)$

Recalculate $J(i, j+1, k, l)$

ELSE

$m = N_s$

ENDIF

END WHILE

END FOR (Bacterium)

END FOR (Chemotaxis)

Reproduction:

For given k and l , and each bacterium $i = 1, 2, \dots, S$

Sum:

$$J_{health}^i = \sum_{j=1}^{N_{c+1}} J(i, j, k, l)$$

Sort:

Sort bacteria and chemotactic parameters $C(i)$ in order of ascending cost J_{health} .

Split and Eliminate:

The S_r bacteria with the highest J_{health} values die and the remaining S_r bacteria with the best values split.

END FOR (Reproduction)

Disperse:

For $i = 1, 2, \dots, S$, with probability P_{ed} randomize a bacterium's position

END FOR (Elimination and Dispersal)

END

The pixels visited by the bacterium are considered to be the desired edge pixels. Thus, the path traced out by bacteria gives the edges.

6. Results

An edge detector can be evaluated based on two parameters. First, its accuracy in determining the edge pixels, and second, it should provide useful information in the form of meaningful edges.

The accuracy is ascertained using Relative Grading technique (Bryant and Bouldin, 1979). In this, a majority image is found using the results of other five edge detectors: Canny, Edison, Rothwell, Sobel, and SUSAN. Then a pixel-by-pixel comparison of the output of the proposed method is made with the true image.

A pixel in the majority image is an edge pixel, if the majority of the methods claim to have an edge pixel in its neighborhood, with at least one centered on it. For example, Fig. 5(h), shows the majority image obtained from Fig. 5(b)–(f).

A majority image is obtained from methods $1, 2, \dots, n$ as $M(\text{method1}, \text{method2}, \dots, \text{methodn})$.

The kappa (a measure of accuracy) (Cohen, 1960) for the pixel-to-pixel comparison between two images I_1 and I_2 is denoted by $k(I_1, I_2)$.

The information content of the output image is measured by using Shannon's entropy function (Shannon, 1948). It gives the indefiniteness in an image and is calculated from

$$H(I) = \sum_{i=0}^L p_i \log p_i \quad (22)$$

where, I stand for the Image. p_i is the frequency of pixels with intensity i . As we have binary levels a window of 3×3 centered at the pixel of concentration is considered as the intensity value.

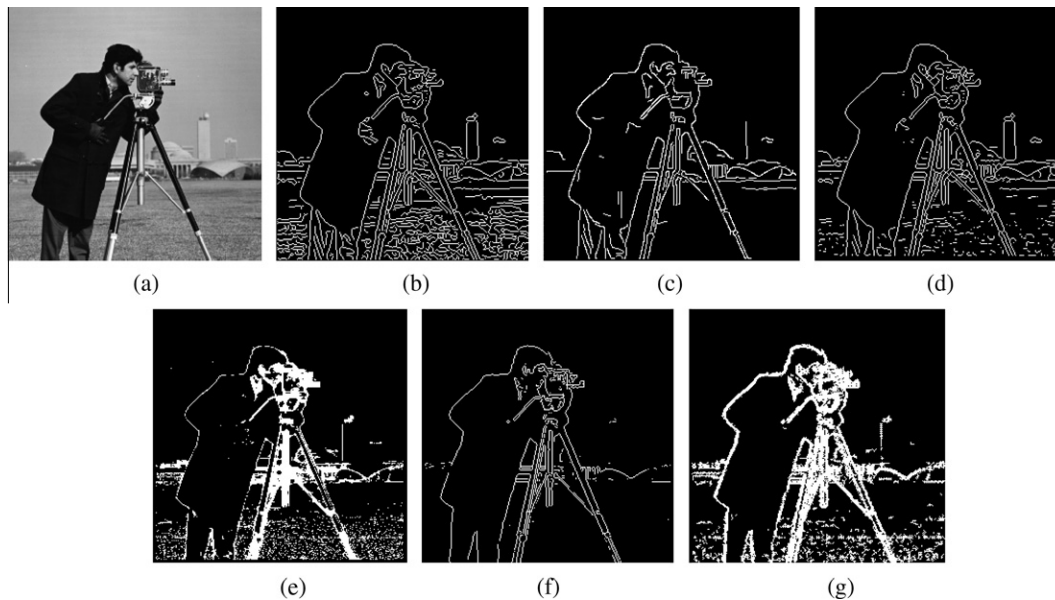


Fig. 2. (a) Original Cameraman image (b) Canny Edge Detector (c) Edison Edge Detector (d) Rothwell Edge Detector (e) SUSAN Edge Detector (f) Sobel Edge Detector and (g) The proposed approach.

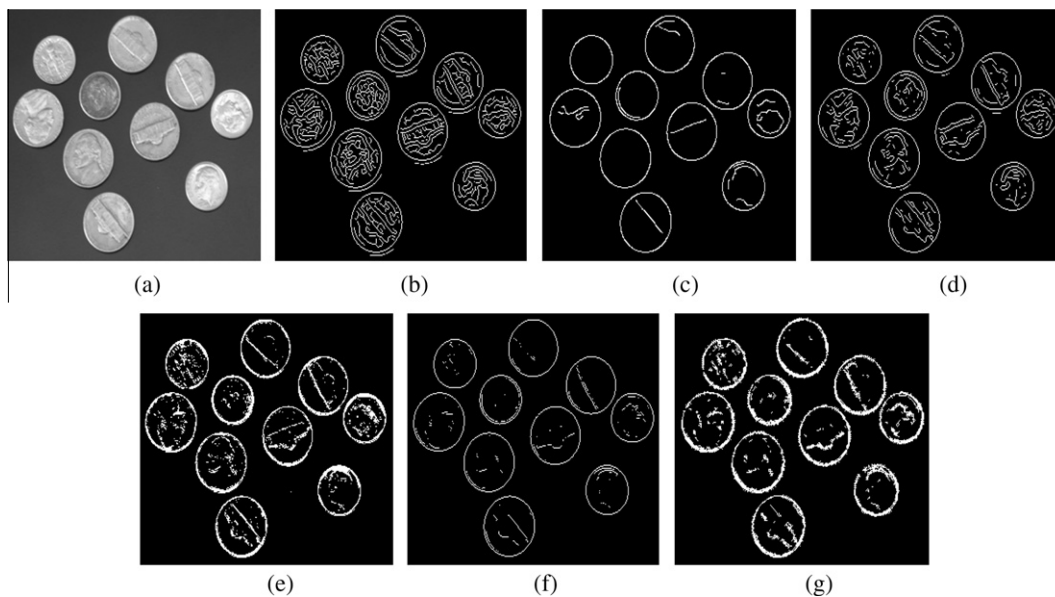


Fig. 3. (a) Original Coins image (b) Canny Edge Detector (c) Edison Edge Detector (d) Rothwell Edge Detector (e) SUSAN Edge Detector (f) Sobel Edge Detector and (g) The proposed approach.

6.1. Comparison with other techniques

The performance of the proposed technique is compared against that of the traditional edge detectors such as Canny, Edison, Rothwell, Sobel and SUSAN. The, traditional edge detectors are implemented using the MATLAB toolbox. The proposed method is also coded in the MATLAB. The parameters are taken as: $S = 100$, $S_r = 0.05S$, $N_s = 10$, $P_{ed} = 0.95$, $N_{ed} = 15$, $N_{re} = 1$, $N_c = 100$. The path traversed by a bacterium represents the edge pixels and is colored white on the black background.

For images in Figs. 2–6, the captions are as follows: (a) the original image, (b) the result of Canny Edge Detector, (c) the result of Edison Edge Detector, (d) the result of Rothwell Edge Detector, (e)

the result of SUSAN Edge Detector, (f) the result of Sobel Edge Detector, and (g) the result of the proposed approach.

It is observed that the edges are accurately detected. But our method lacks in presenting the complete edges. This is because of restrictions imposed on the maximum swim length for a bacterium. Also, thick edges can be seen due to bacteria moving parallel to an edge.

Table 1 shows the kappa values in a comparison of several edge detectors. The column 2 of Table 1 shows $k(M(C, E, R, So, Su), P)$, where, C stands for Canny, E for Edison, R for Rothwell, So for Sobel, Su for SUSAN, and P for the proposed method. It may be noted that the values of kappa around 0.5 indicate the poor performance.

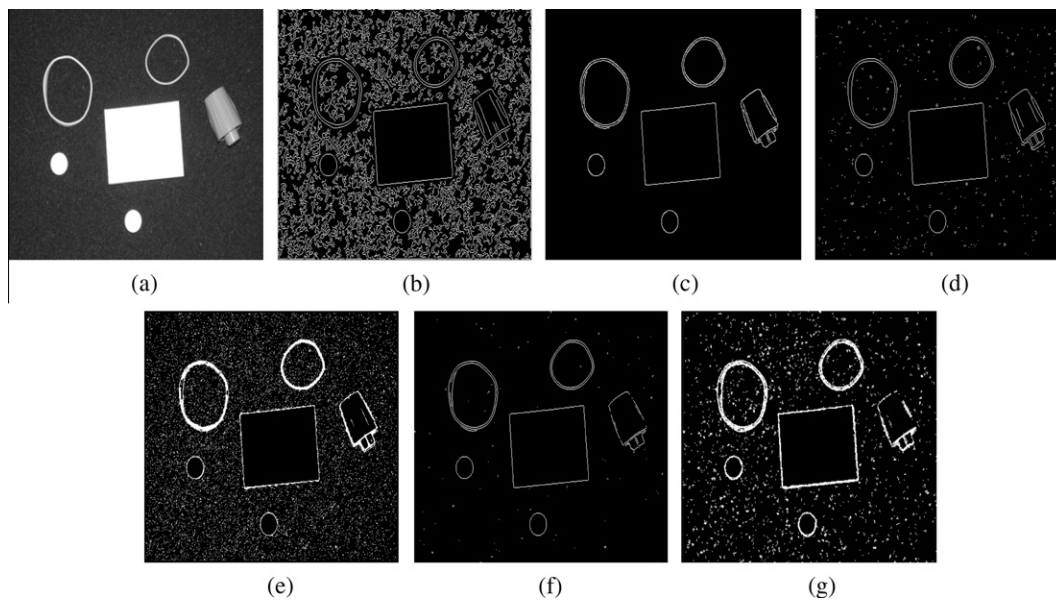


Fig. 4. (a) Original Pillsc image (b) Canny Edge Detector (c) Edison Edge Detector (d) Rothwell Edge Detector (e) SUSAN Edge Detector (f) Sobel Edge Detector and (g) The proposed approach.

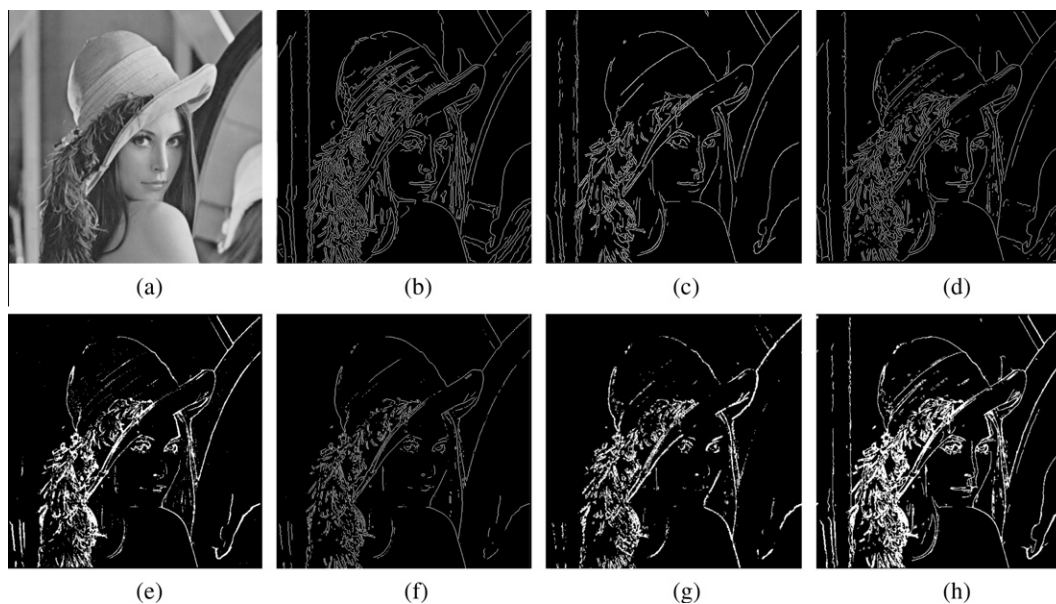


Fig. 5. (a) Original Lena image (b) Canny Edge Detector (c) Edison Edge Detector (d) Rothwell Edge Detector (e) SUSAN Edge Detector (f) Sobel Edge Detector (g) The proposed approach and (h) Majority image obtained using (b) to (f).

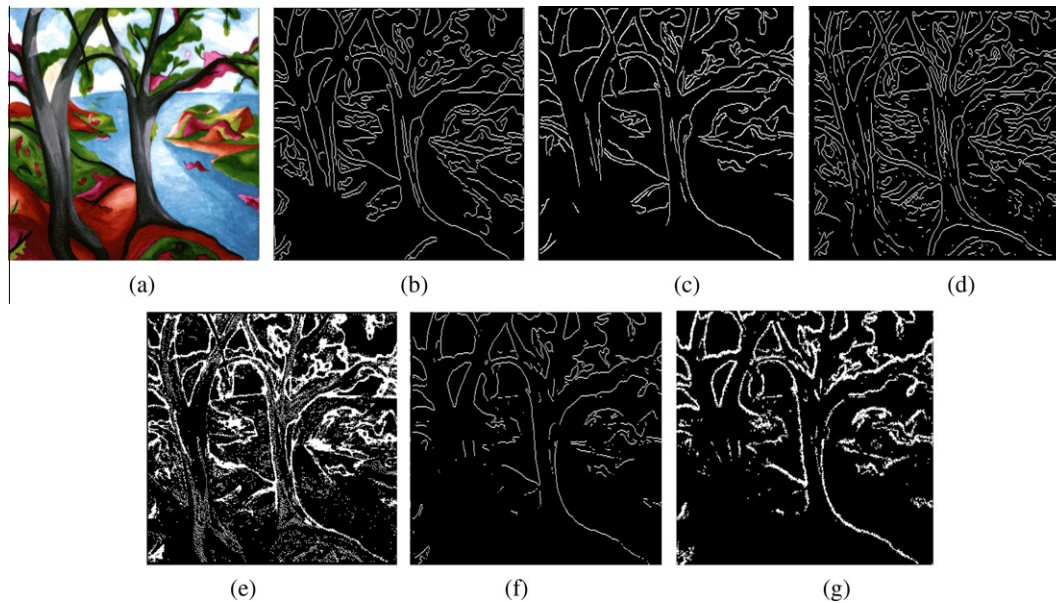


Fig. 6. (a) Original Trees image (b) Canny Edge Detector (c) Edison Edge Detector (d) Rothwell Edge Detector (e) SUSAN Edge Detector (f) Sobel Edge Detector and (g) The proposed approach.

Table 1

Kappa values for comparison with majority image. Column 2 Kappa for proposed edge detector's output comparison with $M(C, E, R, So, Su)$, Columns 3–7: A comparison of Kappa for the ratio, standard edge detector/the proposed edge detector with majority image from other detectors.

Image	Majority	Sobel/Prop.	Canny/Prop.	Edison/Prop.	Rothwell/Prop.	SUSAN/Prop.
Trees	0.4381	0.2802/0.4357	0.3751/0.5103	0.4243/0.4546	0.3349/0.5234	0.3771/0.4915
Lena	0.4594	0.3994/0.4567	0.3831/0.5163	0.4658/0.4996	0.4491/0.5172	0.4622/0.3884
Pillsetc	0.4792	0.3749/0.4744	0.0785/0.4967	0.4133/0.4755	0.4727/0.5016	0.2541/0.3505
Coins	0.5433	0.3878/0.5406	0.3577/0.6098	0.43/0.549	0.4504/0.6108	0.4835/0.4806
Cameraman	0.5953	0.3581/0.5895	0.3474/0.6272	0.3855/0.61	0.433/0.6309	0.4252/0.4198

The column 3 of Table 1 shows the ratio between M of So and M of P .

$$k(M(C, E, R, So, Su), So) / k(M(C, E, R, So, Su), P)$$

Similarly, the ratios due to other standard edge detectors are given in other columns.

It may be observed from Table 1 that the proposed method outperforms 4 out of 5 methods in all images. The results of the proposed method are poor with respect to Susan edge detector in three images viz. Lena, Coin and Camera man.

Table 2 shows the entropy values for the outputs of different methods on various images. A high entropy value signifies more randomness and less information. Sobel edge detector has the least value of entropy for all images and can be seen to have most appropriate edges. Edison edge detector also performs well. The edge detectors of Rothwell and Canny have a comparable performance over the proposed method but SUSAN edge detector performs

poorer than all. It is evident from the results that our method finds meaningful edges in most images but is partially successful in curbing noise as shown in Fig. 4(g).

6.2. Effects of parameter variation

We now discuss the effects of varying different parameters of the proposed method namely: S , S_r , N_s , P_{ed} , N_{ed} , N_{re} and N_c on the resultant image of cameraman.

The variation of parameters is judged by two measures: entropy and kappa. To calculate kappa, the output image is compared with the majority image obtained from other 5 methods as explained above. Moreover, it is well known that an optimum value of parameter is the one with less entropy and high kappa.

The results are of edge detection as shown in Fig. 7(a)–(g). We find that N_{re} and N_c have no considerable effect on the results. Both kappa and entropy remain constant. N_s , the swim length causes both entropy and kappa to decrease as it is increased. Decrease in kappa is gradual than the decrease in entropy. Change in bacteria split ratio (S_r) has no effect on kappa but entropy is significantly varied as can be seen in Figs. 7(b) and 8. In Fig. 7(b) we have taken different values of S_r from 0.15 to 0.55, where S is the number of bacteria. Change in N_{ed} causes entropy to drop after $N_{ed} = 10$. Though, kappa also drops but not significantly whereas in Fig. 7(a), we find that there is no change in entropy with change in number of bacteria (S) but kappa increases (Fig. 9(a) and (b)). It may also be noted that though increase in S is favorable here but it adds more burden on computing resources. Thus, an optimal

Table 2

Entropy values of different edge detector for multiple images.

Image	Edison	SUSAN	Rothwell	Canny	Sobel	Proposed
Trees	0.8682	1.7299	1.0936	0.9109	0.5791	0.8682
Lena	0.6777	0.7928	0.7438	0.8848	0.5303	0.7146
Pillsetc	0.2369	1.1692	0.3332	1.421	0.2265	0.7903
Coins	0.4992	0.8759	0.7201	0.9201	0.4821	0.86
Cameraman	0.6852	1.1499	0.8015	0.9931	0.5633	1.2212

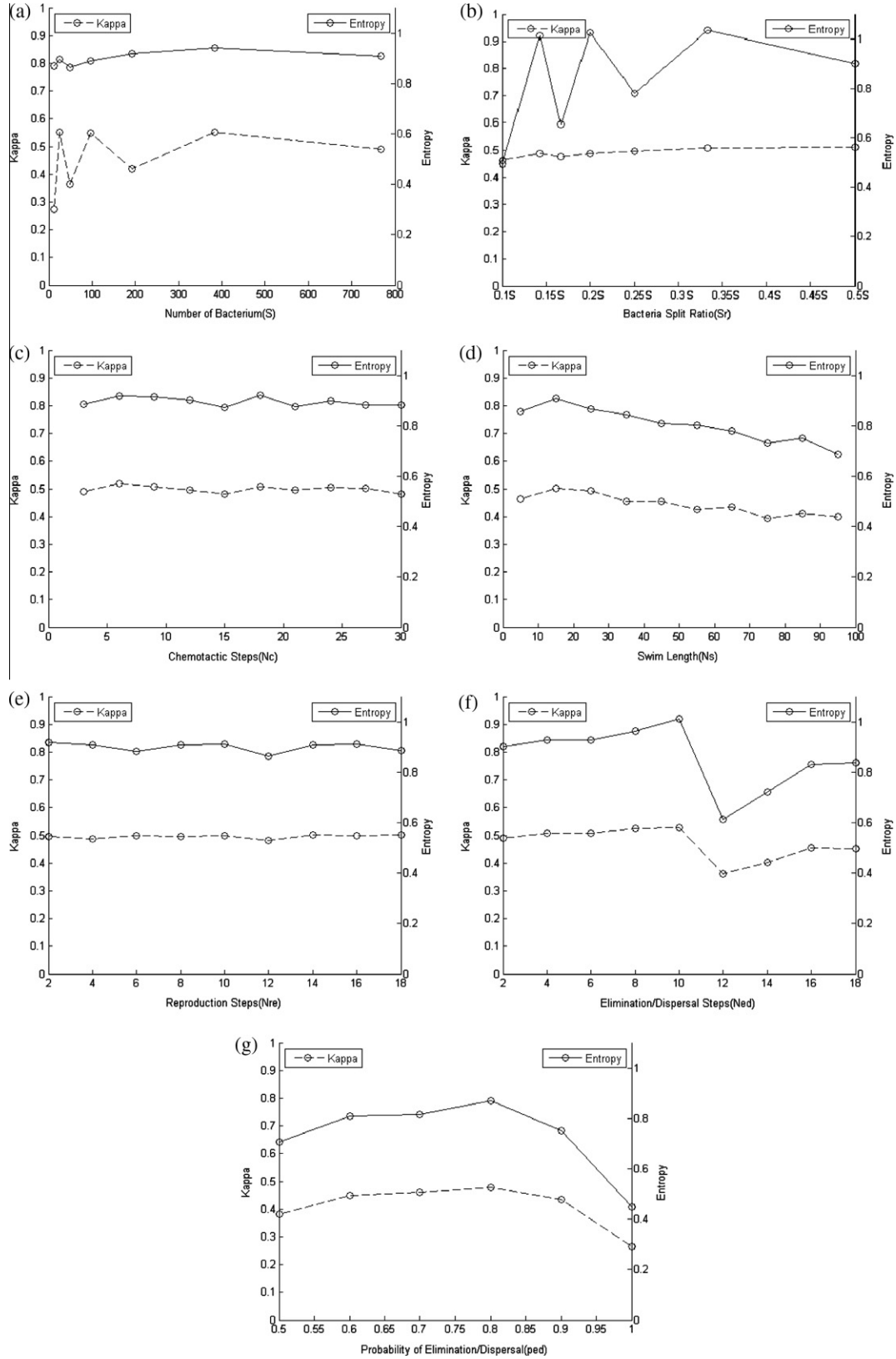


Fig. 7. Plot between Kappa and Entropy v/s initial values parameters (a) S (b) S_r (c) N_c (d) N_s (e) N_{re} (f) N_{ed} (g) P_{ed} .

trade-off has to be found between performance and resources. In Fig. 7(g), we observe that the shape of plots of both kappa and entropy is a parabola facing downwards and centered on 0.8. It also validates that a value of P_{ed} around 0.9 would be optimum.

7. Conclusion and future work

Edge detection is essential in many tasks of image processing. This study proposes a novel BF based approach for edge detection.

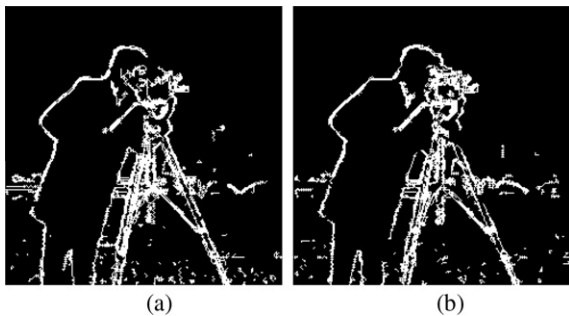


Fig. 8. Output images for the split ratio (a) $S_r = 0.25S$ (b) $S_r = 0.33S$.

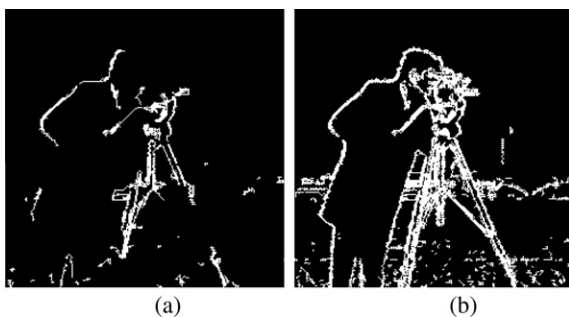


Fig. 9. Output images for the split ratio (a) $S = 12$ and (b) $S = 768$.

The proposed method finds robust edges even in the complex and noisy images. This work opens a new domain of research in the field of edge detection using bio-inspired algorithms.

The results of the proposed method are compared with those of other standard methods using kappa and entropy. Our method performs better than many other standard methods. The variation of several initial parameters on the output of the proposed edge detector is discussed. Their values are derived empirically. These values may also be found specifically for each image to gain maximum benefit. So a way to calculate the optimum values of all the parameters in less time needs to be investigated.

It is noted that our results show some disconnected edges. Since BFOA has been devised with the aim of finding global extremes, this error is expected. If a form of preferential treatment such that

pixels connected to edge pixels get an advantage is introduced then this problem can be mitigated. Also, some form of repellent need to be added to the path already traced by bacteria so that parallel/double edges are not formed.

References

- Abdallah, A.A., Ayman, A.A., 2009. Edge detection in digital images using fuzzy logic techniques. *World Academy of Sci. Eng. Technol.* 51, 178–186.
- Bryant, D.J., Bouldin, D.W., 1979. Evaluation of edge operators using Relative and absolute grading. In: *Proc. IEEE Comput. Soc. Conf. Pattern Recognition and Image Processing*, pp. 138–145.
- Canny, J.F., 1986. A computational approach to edge detection. *IEEE Trans. Pattern Anal. Machine Intell.* 8 (6), 679–698.
- Cheung, K., Chan, W., 1995. Fuzzy one –Mean algorithm for edge detection. *IEEE Internat. Conf. Fuzzy Systems*, 2039–2044.
- Cohen, J., 1960. A coefficient of agreement for nominal scales. *Educ. Psychol. Measure.* 20 (1), 37–46.
- Dorigo, M., Gambardella, L.M., 1997. Ant colony system: A cooperative learning approach to the traveling salesman problem. *IEEE Trans. Evol. Comput.*, 73–81.
- El-Khamy, S., El-Yamany, N., Lotfy, M., 2000. A modified fuzzy sobel edge detector. In: *Seventeenth National Radio Science Conf. (NRSC'2000)*, February 22–24, Minufia, Egypt, 2000.
- Hanmandlu, M., Verma, O.P., Kumar, N.K., Kulkarni, M., 2009. A novel optimal fuzzy system for color image enhancement using bacterial foraging. *IEEE Trans. Instrum. Measure.* 58 (8), 2867–2879.
- Kim, D.H., Cho, C.H., 2005. Bacterial foraging based neural network fuzzy learning. *IICAI*, 2030–2036.
- Kuo, Y., Lee, C., Liu, C., 1997. A new fuzzy edge detection method for image enhancement. *IEEE Internat. Conf. Fuzzy Systems*, 1069–1074.
- Liu, Y., Passino, K.M., 2002. Biomimicry of social foraging bacteria for distributed optimization models, principles and emergent behaviors. *J. Optim. Theory Appl.* 115 (3), 603–628.
- Marr, D., Hildreth, E.C., 1980. Theory of edge detection. *Proc. Roy. Soc. London B* 207, 187–217.
- Mishra, S., 2005. A hybrid least square-fuzzy bacterial foraging strategy for harmonic estimation. *IEEE Trans. Evol. Comput.* 9 (1), 61–73.
- Mishra, S., Bhende, C.N., 2007. Bacterial foraging technique-based optimized active power filter for load compensation. *IEEE Trans. Power Delivery* 22 (1), 457–465.
- Passino, K.M., 2002. Biomimicry of bacterial foraging for distributed optimization and control. *Control Systems Magazine, IEEE* 22 (3), 52–67.
- Raman, Maini, Sobel, J.S., 2006. Performance evaluation of prewitt edge detector for noisy images. *GVIIP J.* 6 (3).
- Russo, F., 1998. Edge detection in noisy images using fuzzy reasoning. *IEEE Trans. Instrum. Measure.* 47 (5), 1102–1105.
- Shannon, C.E., 1948. A mathematical theory of communication. *Bell Syst. Tech. J.* 27, 379–423. 623–656.
- Smith, S.M., Brady, J.M., 1997. SUSAN – A new approach to low level image processing. *Internat. J. Comput. Vision* 23 (1), 45–78.
- Tripathy, M., Mishra, S., Lai, L.L., Zhang, Q.P., 2006. Transmission loss reduction based on FACTS and bacteria foraging algorithm. *PPSN*, 222–231.
- Verma, O.P., Hanmandlu, M., Kumar, P., Srivastava, S., 2009. A novel approach for edge detection using ant colony optimization and fuzzy derivative technique. *Proc. IEEE, IACC*, 1206–1212.

Emergent universe with scalar (or tachyonic) field in higher derivative theory

C.P. Singh · Vijay Singh

Received: 10 November 2011 / Accepted: 5 January 2012
© Springer Science+Business Media B.V. 2012

Abstract We consider a spatially homogeneous and isotropic flat Robertson-Walker model filled with a scalar (or tachyonic) field minimally coupled to gravity in the framework of higher derivative theory. We discuss the possibility of the emergent universe with normal and phantom scalar fields (or normal and phantom tachyonic fields) in higher derivative theory. We find the exact solution of field equations in normal and phantom scalar fields and observe that the emergent universe is not possible in normal scalar field as the kinetic term is negative. However, the emergent universe exists in phantom scalar field in which the model has no time-like singularity at infinite past. The model evolves into an inflationary stage and finally admits an accelerating phase at late time. The equation of state parameter is found to be less than -1 in early time and tends to -1 in late time of the evolution. The scalar potential increases from zero at infinite past to a flat potential in late time. More precisely, we discuss the particular case for phantom field in detail. We also carry out a similar analysis in case of normal and phantom tachyonic field and observe that only phantom tachyonic field solution represents an emergent universe. We find that the coupling parameter of higher order correction affects the evolution of the emergent universe. The stability of solutions and their physical behaviors are discussed in detail.

Keywords Emergent universe · Scalar field · Tachyonic field · Modified theory of gravity

1 Introduction

Harrison (1967) described a model of closed universe filled with radiation in the presence of a cosmological constant, which asymptotically coincides with Einstein static model in infinite past. Ellis and Maartens (2004) considered the possibility of a similar cosmological solution in which there is no big-bang singularity and the universe effectively avoids a quantum regime for the space-time by staying large at all times. An interesting example of this scenario were given by Ellis et al. (2004) for a closed universe with a minimally coupled scalar field ϕ , which has a special form of interacting potential $V(\phi)$ and possibly the same ordinary matter with equation of state $p = \omega\rho$, where $-\frac{1}{3} \leq \omega \leq 1$. However, exact analytic solution was not presented in this model. A viable cosmological model should accommodate an inflationary phase in the early universe with a suitable accelerating phase at late time. In this way the search of singularity free inflationary model in the context of classical general relativity has recently led to the development of emergent universe (EU).

An emergent universe is a model of the universe in which there is no time-like singularity and having almost static behavior in the infinite past. The EU model eventually evolves from a static phase in the infinite past into an inflationary stage and finally it admits an accelerating phase at late time. In fact EU scenario can said to be a modern version and extension of the original Lamaitre-Eddington universe. In EU scenario, it is assumed that the initial conditions are specified such that the static configuration represents the past eternal state of the universe, out of which the universe slowly

C.P. Singh (✉) · V. Singh
Department of Applied Mathematics,
Delhi Technological University
(Formerly Delhi College of Engineering), Bawana Road,
Delhi 110 042, India
e-mail: cpsphd@rediffmail.com

V. Singh
e-mail: gtrcosmo@gmail.com

evolves into an inflationary phase. The salient features of an emergent universe may be summarized as: (1) the universe is almost static at the infinite past ($t \rightarrow -\infty$) and isotropic and homogeneous at large scales, (2) it is ever existing and there is no time-like singularity, (3) the universe is always large enough so that the classical description of space-time is adequate, (4) the universe may contain exotic matter so that the energy condition may be violated and (5) the universe is accelerating as suggested by recent measurements of distance of high red-shift type Ia-Supernovae.

Many authors have proposed EU model in different frameworks because it permits a universe which is ever existing and large enough so that the space-time may be treated as classical entities. Mukherjee et al. (2005) obtained solutions for Starobinsky model and examined the features of EU. Mukherjee et al. (2006) considered a general framework for emergent universe model filled with exotic matter by use of an effective equation of state $p = A\rho - B\sqrt{\rho}$, where A and B are constants. Campo et al. (2007) studied the emergent universe model in the context of a self-interacting Jordan-Brans-Dicke theory and showed that the model presents a stable past eternal static solution which eventually enters into a phase where the stability of the solution is broken leading to an inflationary period. Banerjee et al. (2007, 2008) discussed a model of EU in Brane-world scenario. Debnath (2008) studied the behavior of different stages of the evolution of EU filled with normal matter and a phantom field in general relativity. Beesham et al. (2009) studied the EU with sigma model and discussed the physical behavior in detail. Mukerji and Chakraborty (2010) discussed Einstein-Gauss-Bonnet theory in EU scenario. Paul et al. (2010, 2011) studied the range of the permissible values for the parameters associated with the constraints on exotic matter needed for an emergent universe. Paul and Ghose (2010) discussed the EU scenario in the Einstein-Gauss-Bonnet gravity with dilaton. Mukerji and Chakraborty (2011) studied the EU in Horařa gravity. Debnath and Chakraborty (2011) and Chakraborty and Debnath (2011) also studied the emergent universe in the context of various theories and found that the scenario can be realized fairly well.

Many observational and theoretical models have been considered to explain the accelerated expansion of the universe. The recent observations from type Ia supernovae (Riess et al. 1998, 2001, 2004; Schmidt et al. 1998; Perlmutter et al. 1999) associated with Large Scale structure (Tegmark et al. 2004) and Cosmic Microwave Background anisotropies (Spergel et al. 2003, 2007) have provided main evidence for this cosmic acceleration. The substance responsible for this accelerated expansion is usually called dark energy. Examples of dark energy models are vacuum energy (Sahni and Starobinsky 2000; Peebles and Ratra 2003; Padmanabhan 2003; Shapiro and Sola 2009) which has the

equation of state parameter $\omega = -1$, quintessence (Zlatev et al. 1999; Hao and Li 2002; Zimdahl et al. 2001; Guo and Zhang 2005), phantom (Caldwell 2002; Caldwell et al. 2003; Nojiri and Odintsov 2003a; Elizalde et al. 2004; Hao and Li 2005; Gonzalez and Quiros 2008), tachyon (Padmanabhan 2002; Melchiorri et al. 2003; Sami 2004a, 2004b) and references therein), etc. However, the fine-tuning problems related to the vacuum energy are still the problems with the available observations. Most of the dark energy models involve one or more scalar fields with various actions and with or without a scalar field potential. The equation of state parameter ω seems to be near less than -1 , and $-1.62 < \omega < -0.72$ (Tegmark et al. 2004). The accelerated expansion can be explained by the presence of a global cosmic scalar field slowly moving down to the potential minimum. Physical properties of dark energy with $\omega < -1$ differ markedly from the case when $\omega \geq -1$. For instance, it violates the energy dominance condition $\rho \geq |p|$. If $\omega \geq -1$, the dark energy density is not increasing (or even decreasing) as universe expands. If we allow $\omega \leq -1$, the dark energy density grows and becomes infinite at a finite time. There is another less evident consequence of $\omega < -1$: if dark energy density is really the phantom one, the evolution of the universe needs not to contain a Big Bang. The study of late universe however, remains open to address the present issues in other theories. Now a days the dark energy models such as quintessence, phantom and tachyon models are of great interest.

There are several other approaches to the theoretical descriptions of the accelerated expansion of the universe. In the past few years, a number of many modified theories such as $f(R)$ theory, here $f(R)$ is an arbitrary function of scalar curvature (for recent reviews see, Nojiri and Odintsov 2003b, 2006, 2007a, 2007b, 2011) have been proposed to explain the cosmological problems of the universe by modifying the Einstein gravitation theory. One of the attempts to modify Einstein theory of gravitation is the higher derivative (HD) theory, which is based on adding an additional term R^2 in gravitational action, i.e., $R + \alpha R^2$, where α is a coupling constant. Starobinsky (1980) studied the cosmological models in HD theory and showed that this theory admits inflation. The dynamics of higher order cosmology is related to scalar field. The cosmological models based on scalar field have a long history (see Capozziello et al. 2006), being used for exploration of possible inflationary scenario and for the description of dark energy models. Paul (1999) considered the cosmological model with scalar field in HD theory for power-law and exponential expansions of the universe. Ellis and Madsen (1991), Barrow and Saich (1993), Barrow and Mimoso (1994), and Mimoso and Wands (1995) have studied the cosmological models with perfect fluid and scalar field. Ibotombi et al. (2011) have studied FRW model filled with viscous fluid and zero rest-mass scalar-field in HD theory. Singh and Singh (2011) have studied FRW models with

scalar field in HD theory and have observed the inflationary scenario of the universe.

In this paper, it is of interest to study the emergent universe scenario in the presence of scalar field (or tachyonic field) minimally coupled to gravity with scalar potential in HD theory. The universe is chosen as a spatially homogeneous and isotropic flat Friedmann-Robertson-Walker (FRW) model. We discuss the possibility of emergent universe for normal and phantom scalar fields. We find the exact solution of field equations in normal and phantom scalar fields and observe that the emergent universe is not possible in normal scalar field as the kinetic term is negative. However, the emergent universe exists in scalar phantom field in which the model has no time-like singularity at infinite past. The equation of state parameter (EoS) is always less than -1 . The scalar potential increases from zero at infinite past to a flat value in late time. We also carry out a similar analysis in case of normal and phantom tachyonic fields and observe that only phantom tachyonic field solution has the behavior of emergent universe. We find that the coupling parameter of higher order correction affects the evolution of the emergent universe.

The paper is organized as follows. In Sect. 2.1 we present the basic gravitational action and the relevant field equations of higher derivative theory with scalar field (normal and phantom). The possibility of an emergent scenario is discussed in Sect. 2.2. In Sect. 3.1 we present the gravitational action and relevant field equations with tachyonic field (normal and phantom) in HD theory and the possibility of EU is discussed in Sect. 3.2. Finally, in Sect. 4 we summarize the results obtained in Sects. 2.2 and 3.2.

2 Scalar (normal and phantom) field

2.1 Gravitational action and field equations

The gravitational action for higher derivative theory of gravity with a scalar field ϕ , minimally coupled to gravity and matter fluid in the units $8\pi G = 1$ and $c = 1$, takes the following form (Starobinsky 1980)

$$I = - \int \left[\frac{1}{2} (R + \alpha R^2) + \frac{\epsilon}{2} \phi_{,\mu} \phi^{,\mu} + V(\phi) \right] \sqrt{-g} d^4x, \quad (1)$$

where R is the scalar curvature, $V(\phi)$ represents the relevant potential of the scalar field ϕ and $\epsilon = \pm 1$ correspond to normal or phantom scalar field, respectively, g is the determinant of the four dimensional metric and $\alpha > 0$ is the coupling constant.

Variation of the action (1) with respect to the metric tensor, $g_{\mu\nu}$ gives the following field equations

$$R_{\mu\nu} - \frac{1}{2} g_{\mu\nu} R + \alpha \left[2R \left(R_{\mu\nu} - \frac{1}{4} g_{\mu\nu} R \right) + 2(R_{\mu\nu} - g_{\mu\nu} \square R) \right] = -T_{\mu\nu}, \quad (2)$$

where a semi colon denotes the covariant derivative, \square is the covariant differential operator and $T_{\mu\nu}$ is the energy momentum tensor of scalar field which is given by

$$T_{\mu\nu} = \epsilon \phi_{,\mu} \phi_{,\nu} - g_{\mu\nu} \left[\frac{\epsilon}{2} \phi_{,\sigma} \phi^{,\sigma} + V(\phi) \right]. \quad (3)$$

The metric of a spatially homogeneous and isotropic flat Friedmann-Robertson-Walker (FRW) model is

$$ds^2 = dt^2 - a^2(t) [dr^2 + r^2(d\theta^2 + \sin^2\theta d\phi^2)], \quad (4)$$

where $a(t)$ is the scale factor.

The field equations (2) with energy momentum tensor (3) for the line element (4) in HD theory can be written as

$$3H^2 - 18\alpha[2\ddot{H}H - \dot{H}^2 + 6\dot{H}H^2] = \frac{\epsilon}{2}\dot{\phi}^2 + V(\phi), \quad (5)$$

$$2\dot{H} + 3H^2 - 6\alpha[2\ddot{H} + 12\ddot{H}H + 18\dot{H}H^2 + 9\dot{H}^2] = - \left[\frac{\epsilon}{2}\dot{\phi}^2 - V(\phi) \right]. \quad (6)$$

where $H = \frac{\dot{a}}{a}$ is the Hubble parameter and a dot denotes derivative with respect to cosmic time t .

The energy conservation equation for scalar field is given by

$$\epsilon\ddot{\phi} + 3\epsilon H\dot{\phi} = -V'(\phi), \quad (7)$$

where a prime denotes the derivative with respect to scalar field ϕ . The equation of state (EoS) parameter ω_ϕ for the scalar field is given by

$$\omega_\phi = \frac{\frac{\epsilon}{2}\dot{\phi}^2 - V(\phi)}{\frac{\epsilon}{2}\dot{\phi}^2 + V(\phi)}, \quad (8)$$

which generally varies with time. It is to be noted that the accelerating expansion is attributed to dark energy which is an exotic component with negative pressure, such as quintessence scalar field with equation of state $\omega_\phi > -1$ or phantom with $\omega_\phi < -1$ (Caldwell 2002; Sahni et al. 2002; Singh et al. 2003; Sami 2004a, 2004b).

As we see the field equations (5) and (6) are highly non-linear, therefore, in order to get the solution we confine our attention to the emergent universe for scalar field (normal or phantom) in HD theory, i.e., a universe in which the evolution of the scale factor is of the form (Ellis and Maartens 2004; Campo et al. 2007)

$$a = a_0(\beta + e^{\gamma t})^n, \quad (9)$$

where a_0 , β , γ and n are positive constants. This form of scale factor describes the EU scenario where the universe starts with a finite volume at infinite past, expands without encountering any singularity for any time t and finally, the universe becomes of infinite volume at future infinity.

For this choice of the scale factor, the Hubble parameter and its derivatives are given by

$$\begin{aligned} H &= \frac{n\gamma e^{\gamma t}}{\beta + e^{\gamma t}}, & \dot{H} &= \frac{n\beta\gamma^2 e^{\gamma t}}{(\beta + e^{\gamma t})^2}, \\ \ddot{H} &= \frac{n\beta\gamma^3 e^{\gamma t}(\beta - e^{\gamma t})}{(\beta + e^{\gamma t})^3} \\ \ddot{H} &= -\frac{n\beta\gamma^4(5e^{3\gamma t} - 2\beta e^{2\gamma t} - \beta^2 e^{\gamma t})}{(\beta + e^{\gamma t})^4} \end{aligned} \quad (10)$$

Here, H , \dot{H} are positive definite but \ddot{H} and \ddot{H} change their sign at $t = \frac{1}{\alpha} \log \beta$ and $t = \frac{1}{\gamma} \log \frac{\beta(1+\sqrt{6})}{5}$, respectively. All the four tend to zero as $t \rightarrow -\infty$. On the other hand as $t \rightarrow \infty$, the model becomes a de Sitter universe. The deceleration parameter q , which is defined as $q = -a\ddot{a}/\dot{a}^2$, is given by

$$q = -1 - \frac{\beta}{ne^{\gamma t}}, \quad (11)$$

which shows that q is an increasing function of t . As $t \rightarrow -\infty$, $q \rightarrow -\infty$ and as $t \rightarrow \infty$, q asymptotically tends to -1 . The Hubble parameter corresponding to (9) satisfies a first order differential equation given by

$$\dot{H} = \gamma H - \frac{1}{n} H^2. \quad (12)$$

2.2 Cosmological solution

Solving (5) and (6) by use of (9), we get

$$\begin{aligned} \epsilon \dot{\phi}^2 &= -\frac{2n\beta\gamma^2 e^{\gamma t}}{(\beta + e^{\gamma t})^2} - \frac{12n\alpha\beta\gamma^4}{(\beta + e^{\gamma t})^4} [(3n-1)e^{3\gamma t} \\ &\quad - (9n-4)\beta e^{2\gamma t} - \beta^2 e^{\gamma t}], \end{aligned} \quad (13)$$

and

$$\begin{aligned} V(t) &= \frac{n\gamma^2(3ne^{2\gamma t} + \beta e^{\gamma t})}{(\beta + e^{\gamma t})^2} - \frac{6n\alpha\beta\gamma^4}{(\beta + e^{\gamma t})^4} \\ &\quad \times [(18n^2 - 9n + 1)e^{3\gamma t} + 4(3n-1)\beta e^{2\gamma t} \\ &\quad + \beta^2 e^{\gamma t}]. \end{aligned} \quad (14)$$

In the following subsections, we examine the possibility of EU scenario for normal and phantom scalar fields, respectively.

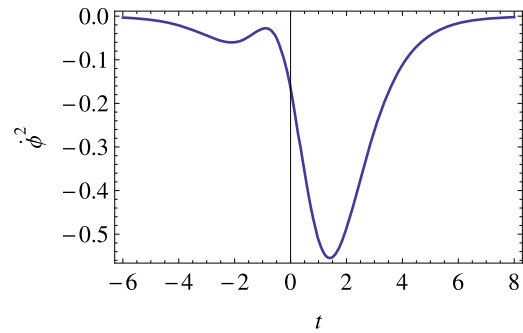


Fig. 1 $\dot{\phi}^2(t)$ versus t for $\beta = 1$, $\gamma = 1$, $n = 4/3$, and $\alpha = 1/12$

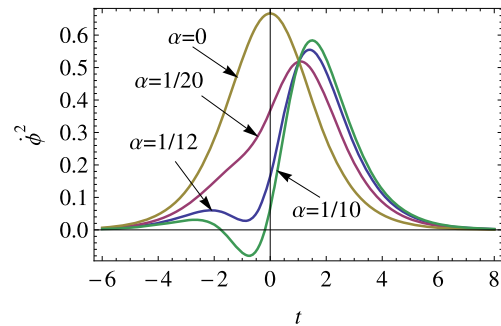


Fig. 2 $\dot{\phi}^2(t)$ versus t for $\beta = 1$, $\gamma = 1$ and $n = 4/3$

2.2.1 Normal scalar field ($\epsilon = +1$)

In the normal scalar field, (13) gives

$$\begin{aligned} \dot{\phi}^2 &= -\frac{2n\beta\gamma^2 e^{\gamma t}}{(\beta + e^{\gamma t})^2} - \frac{12n\alpha\beta\gamma^4}{(\beta + e^{\gamma t})^4} \\ &\quad \times [(3n-1)e^{3\gamma t} - (9n-4)\beta e^{2\gamma t} - \beta^2 e^{\gamma t}]. \end{aligned} \quad (15)$$

We observe that $\dot{\phi}^2$ is negative during the evolution of the Universe as shown in Fig. 1 and hence ϕ becomes imaginary. Therefore, the kinetic term ($\frac{1}{2}\dot{\phi}^2$) is negative in normal field but it must be positive. Therefore, the EU scenario is not possible for flat universe with normal scalar field in HD theory.

2.2.2 Phantom scalar field ($\epsilon = -1$)

In this case, (13) gives

$$\begin{aligned} \dot{\phi}^2 &= \frac{2n\beta\gamma^2 e^{\gamma t}}{(\beta + e^{\gamma t})^2} + \frac{12n\alpha\beta\gamma^4}{(\beta + e^{\gamma t})^4} \\ &\quad \times [(3n-1)e^{3\gamma t} - (9n-4)\beta e^{2\gamma t} - \beta^2 e^{\gamma t}]. \end{aligned} \quad (16)$$

The variation of $\dot{\phi}^2$ with t for some particular values of constant parameters and for different values of α is shown in Fig. 2. It is observed that $\dot{\phi}^2$ is positive for any time t starting with zero at infinite past for small values of α . It increases during the early time but decreases to zero at late

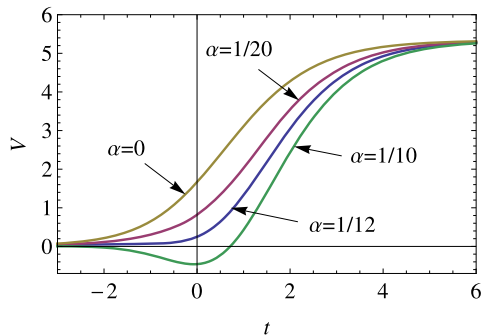


Fig. 3 $V(t)$ versus t for $\beta = 1$, $\gamma = 1$ and $n = 4/3$

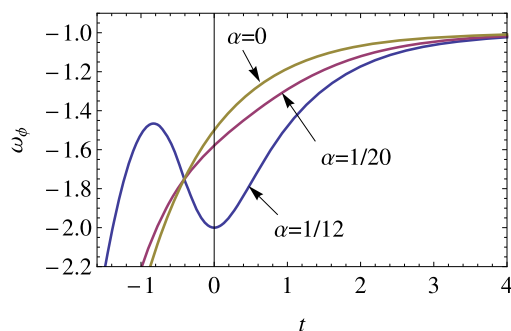


Fig. 4 ω_ϕ versus t for $\beta = 1$, $\gamma = 1$ and $n = 4/3$

time. We find that $\dot{\phi}^2$ increases sharply in general relativity ($\alpha = 0$) whereas it increases gradually to the maximum value and then decreases to zero for $\alpha = 1/20$ and $\alpha = 1/12$. The solutions are stable for small values of α for any time t . However, the solution is unstable for $\alpha = 1/10$, i.e., large values of α as shown in Fig. 2. Due to the complicated expression in (16), it is not possible to find out the range of instability of cosmic time.

Since the scalar potential $V(t)$ is independent of ϵ , therefore, the expression for $V(t)$ is same as given in (14). Now, it is very difficult to express the phantom field ϕ in closed form, so potential function V can not be expressed in terms of ϕ explicitly. In Fig. 3 the graph of scalar potential with time for some particular values of parameters shows that $V(t)$ grows from zero at infinite past for different values of α and becomes flat as $t \rightarrow \infty$. It grows slowly with the evolution of the universe due to the higher derivative term as compare to general relativity case ($\alpha = 0$). Therefore, the phantom field rolls to the maximum of its potential and then settles to a constant value in late time of evolution of the universe. We find that the scalar field density is also positive and zero at infinite past but increases with time and attains the maximum value in late time of the evolution. The model has no time-like singularity at infinite past and it evolves into an inflationary phase and accelerates at late time. From Fig. 4 we can see that the parameter of EoS of phantom field is always less than -1 , while it will approach to -1 in late time.

We conclude that the stability of the solution depends on the coupling parameter α i.e., the solution is stable for small values of α whereas it gives unstable solution for large values of α . The phantom field shows the characteristic of EU for a flat FRW model in HD theory.

2.2.3 Particular solution

Since the field equations in HD theory permit the emergent solution (9) where the Hubble parameter satisfies a first order differential equation (12). Let us consider the particular solution by taking the particular values $\gamma = \frac{1}{\sqrt{6\alpha}}$ and $n = \frac{2}{3}$ in (12). For these particular values, (12) becomes

$$\dot{H} = \frac{1}{\sqrt{6\alpha}}H - \frac{3}{2}H^2. \quad (17)$$

The scale factor is now given by

$$a = a_0 \left[\beta + e^{\frac{1}{\sqrt{6\alpha}}t} \right]^{\frac{2}{3}}. \quad (18)$$

The field equations (5) and (6) yield

$$\epsilon \dot{\phi}^2 = -\frac{4\beta}{9\alpha} \frac{e^{3\sqrt{\frac{1}{6\alpha}}t}}{(\beta + e^{\frac{1}{\sqrt{6\alpha}}t})^4}, \quad (19)$$

and

$$V(t) = \frac{2}{9\alpha} \frac{e^{3\sqrt{\frac{1}{6\alpha}}t}}{(\beta + e^{\frac{1}{\sqrt{6\alpha}}t})^3}. \quad (20)$$

For normal scalar field ($\epsilon = 1$), $\dot{\phi}^2$ is negative throughout the evolution for any positive values of α and hence it becomes imaginary. But for phantom scalar field ($\epsilon = -1$), $\dot{\phi}^2$ is positive throughout the evolution and hence the kinetic term is negative as expected. Taking $\epsilon = -1$ and considering the positive sign of $\dot{\phi}$ in (19) we integrate to get

$$\begin{aligned} \phi(t) = & 2e^{-\frac{3}{2}\sqrt{\frac{1}{6\alpha}}t} (\beta + e^{\frac{1}{\sqrt{6\alpha}}t}) \sqrt{\frac{2\alpha e^{3\sqrt{\frac{1}{6\alpha}}t}}{3\beta(\beta + e^{\frac{1}{\sqrt{6\alpha}}t})}} \\ & \times \left[(\beta + e^{\frac{1}{\sqrt{6\alpha}}t}) \tan^{-1} \left(\frac{e^{\frac{1}{2\sqrt{6\alpha}}t}}{\sqrt{\beta}} \right) - \sqrt{\beta} e^{\frac{1}{2\sqrt{6\alpha}}t} \right], \end{aligned} \quad (21)$$

where the integration constant is taken to be zero for simplicity.

The energy density ρ_ϕ and pressure p_ϕ for phantom scalar field are respectively given by

$$\rho_\phi = -\frac{\dot{\phi}^2}{2} + V(\phi) = \frac{2}{9\alpha} \frac{e^{\frac{4}{\sqrt{6\alpha}}t}}{(\beta + e^{\frac{1}{\sqrt{6\alpha}}t})^4}, \quad (22)$$

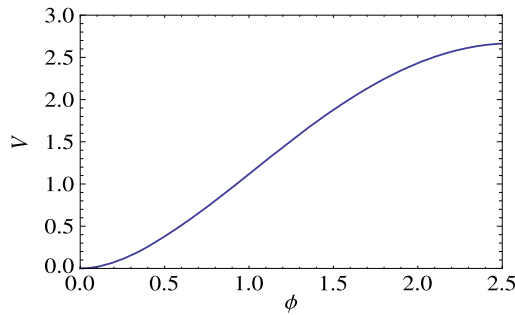


Fig. 5 V versus ϕ for $\beta = 1$ and $\alpha = 1/12$

$$p_\phi = -\frac{\dot{\phi}^2}{2} - V(\phi) = -\frac{2}{9\alpha} \frac{e^{3\sqrt{\frac{1}{6\alpha}}t} (2\beta + e^{\frac{1}{\sqrt{6\alpha}}t})}{(\beta + e^{\frac{1}{\sqrt{6\alpha}}t})^4}. \quad (23)$$

From above solutions we observe that all the physical parameters have only α -terms for the particular values of γ and n . Therefore, we shall find that the EU is possible for any positive values of α . It is difficult to express the phantom potential V in terms of ϕ explicitly. Now from the numerical investigation we have plotted V against ϕ for some particular values of α and β in Fig. 5. From figure, it is to be seen that V always increases as ϕ increases from zero at infinite past to a flat potential at late time. We find that ρ_ϕ grows with time whereas p_ϕ is always negative during the evolution of the universe. The energy dominance condition $\rho \geq |p|$ violates at late times. The model has no time-like singularity. The value of EoS parameter is given by

$$\omega_\phi = -1 - 2\beta e^{-\frac{1}{\sqrt{6\alpha}}t}, \quad (24)$$

which shows that it is less than -1 for any values of t but attains to -1 at late time. The solutions are stable for any values of α for any time t . We can say that the EU is possible in phantom scalar field model in HD theory for any positive values of α . It expands exponentially and finally accelerates at late time.

3 Tachyonic (normal and phantom) field

3.1 Action and field equations

The gravitational action for higher derivative theory of gravity with a tachyonic field ψ , minimally coupled to gravity in the units $8\pi G = 1$ and $c = 1$, takes the following form

$$I = - \int \left[\frac{1}{2} (R + \alpha R^2) + V(\psi) \sqrt{1 - \epsilon \psi_{,\mu} \psi^{,\mu}} \right] \times \sqrt{-g} d^4x, \quad (25)$$

where $V(\psi)$ is relevant tachyonic potential of tachyonic field, $\epsilon = \pm 1$ correspond to normal and phantom tachyonic

fields, respectively and other symbols have their usual meaning.

The energy momentum tensor $T_{\mu\nu}$ of tachyonic field is given as

$$T_{\mu\nu} = V(\psi) \left[\frac{\epsilon \psi_{,\mu} \psi_{,\nu}}{\sqrt{1 - \epsilon \psi_{,\mu} \psi^{,\mu}}} + g_{\mu\nu} \sqrt{1 - \epsilon \psi_{,\mu} \psi^{,\mu}} \right]. \quad (26)$$

The field equations (2) with energy momentum tensor (26) for the line element (4) in HD theory yield

$$3H^2 - 18\alpha [2\ddot{H}H - \dot{H}^2 + 6\dot{H}H^2] = \frac{V(\psi)}{\sqrt{1 - \epsilon \dot{\psi}^2}}, \quad (27)$$

$$2\dot{H} + 3H^2 - 6\alpha [2\ddot{H}H + 12\ddot{H}H + 18\dot{H}H^2 + 9\dot{H}^2] = V(\psi) \sqrt{1 - \epsilon \dot{\psi}^2}. \quad (28)$$

The equation of state (EoS) parameter ω_ψ for the tachyonic field is given by

$$\omega_\psi = -1 + \epsilon \dot{\psi}^2. \quad (29)$$

It can be seen that $\omega_\psi > -1$ or < -1 according as normal tachyon ($\epsilon = +1$) or phantom tachyon ($\epsilon = -1$).

The energy conservation equation for tachyonic field is given as

$$\frac{\ddot{\psi}}{1 - \epsilon \dot{\psi}^2} + 3\epsilon H \dot{\psi} = -\frac{V'(\psi)}{V(\psi)}, \quad (30)$$

where a prime denotes derivative with respect to ψ .

Solving (27) and (28), we get

$$\epsilon \dot{\psi}^2 = \frac{-2\dot{H} + 12\alpha [\ddot{H}H + 3\ddot{H}H + 6\dot{H}^2]}{[3H^2 - 18\alpha \{2\ddot{H}H + 6\dot{H}H^2 - \dot{H}^2\}]}, \quad (31)$$

and

$$V(\psi) = \sqrt{3H^2 - 18\alpha (2\ddot{H}H + 6\dot{H}H^2 - \dot{H}^2)} \times \sqrt{2\dot{H} + 3H^2 - 6\alpha (2\ddot{H}H + 12\ddot{H}H + 18\dot{H}H^2 + 9\dot{H}^2)}. \quad (32)$$

3.2 Cosmological solution

In the following subsections, we examine the possibility of EU scenario for normal and phantom tachyons, respectively.

3.2.1 Normal tachyonic field ($\epsilon = +1$)

From (31) and (32), by use of (10), we get the following expressions for tachyonic field and tachyonic potential, respectively as

$$\dot{\psi}^2 = \frac{\frac{-2n\beta\gamma^2 e^{\gamma t}}{(\beta+e^{\gamma t})^2} - \frac{12n\alpha\beta\gamma^4}{(\beta+e^{\gamma t})^4} [(3n-1)e^{3\gamma t} - (9n-4)e^{2\gamma t} - \beta^2 e^{\gamma t}]}{\frac{3n^2\gamma^2 e^{2\gamma t}}{(\beta+e^{\gamma t})^2} - \frac{18n^2\alpha\beta\gamma^4}{(\beta+e^{\gamma t})^4} [2(3n-1)e^{3\gamma t} + \beta e^{2\gamma t}]}, \quad (33)$$

$$V(t) = \left[\frac{3n^2\gamma^2 e^{2\gamma t}}{(\beta+e^{\gamma t})^2} - \frac{18n^2\alpha\beta\gamma^4}{(\beta+e^{\gamma t})^4} \{2(3n-1)e^{3\gamma t} + \beta e^{2\gamma t}\} \right]^{\frac{1}{2}} \left[\frac{n\gamma^2 (3ne^{2\gamma t} + 2\beta e^{\gamma t})}{(\beta+e^{\gamma t})^2} - \frac{6n\alpha\beta\gamma^4}{(\beta+e^{\gamma t})^4} \{2(9n^2-6n+1)e^{3\gamma t} + (21n-8)\beta e^{2\gamma t} + 2\beta^2 e^{\gamma t}\} \right]^{\frac{1}{2}}. \quad (34)$$

We observe that $\dot{\psi}^2$ is negative during the evolution of the universe and hence ψ becomes imaginary. Therefore, in this case the EU is not possible.

3.2.2 Phantom tachyonic field ($\epsilon = -1$)

In this case, the tachyonic field ($\dot{\psi}^2$) is given by

$$\dot{\psi}^2 = \frac{\frac{-2n\beta\gamma^2 e^{\gamma t}}{(\beta+e^{\gamma t})^2} - \frac{12n\alpha\beta\gamma^4}{(\beta+e^{\gamma t})^4} [(3n-1)e^{3\gamma t} - (9n-4)e^{2\gamma t} - \beta^2 e^{\gamma t}]}{\frac{-3n^2\gamma^2 e^{2\gamma t}}{(\beta+e^{\gamma t})^2} + \frac{18n^2\alpha\beta\gamma^4}{(\beta+e^{\gamma t})^4} [2(3n-1)e^{3\gamma t} + \beta e^{2\gamma t}]}. \quad (35)$$

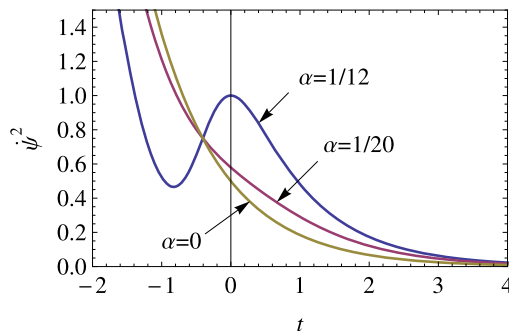


Fig. 6 $\dot{\psi}^2(t)$ versus t for $\beta = 1$, $\gamma = 1$ and $n = 4/3$

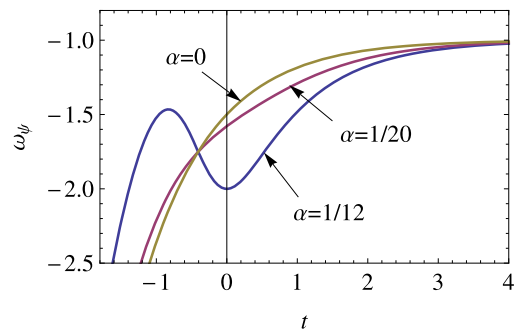


Fig. 8 ω_ψ versus t for $\beta = 1$, $\gamma = 1$ and $n = 4/3$

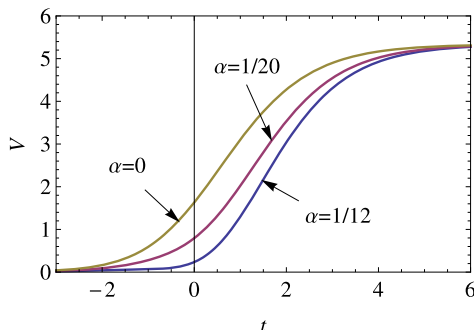


Fig. 7 $V(t)$ versus t for $\beta = 1$, $\gamma = 1$ and $n = 4/3$

Figure 6 shows that $\dot{\psi}^2$ is positive through out the evolution of the universe for small values of α . It is infinite at infinite past and decreases with time, tending to zero in late

time. $\dot{\psi}^2$ decreases sharply in Einstein gravity ($\alpha = 0$) as compared to the HD theory.

The tachyonic potential has the same expression (34) since it is independent of ϵ . It increases from zero at infinite past to a maximum constant value in late time as we can see in Fig. 7. The energy density for tachyonic field is positive through out the evolution. It is zero at infinite past and increases with time and finally attains a finite maximum value in late time. The model has no time-like singularity at any time. Therefore, the EU can be described with phantom tachyonic field in HD theory for small values of α . The variation of EoS parameter ω_ψ with time is shown in Fig. 8. It is to be seen that $\omega_\psi < -1$ and it settles into a state with $\omega_\psi = -1$ in late time. The solutions are stable only for small values of coupling parameter α of HD theory. We conclude that the stability of the solution depends on the coupling pa-

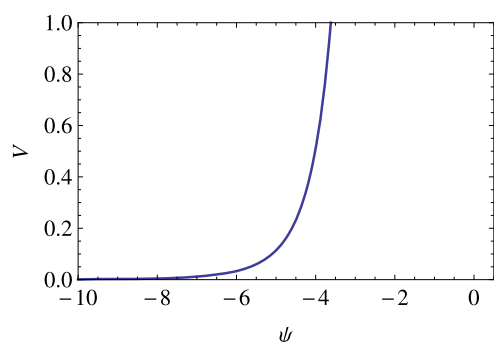


Fig. 9 V versus ψ for $\beta = 1$ and $\alpha = 1/12$

parameter α i.e., the solution is stable for small values of α whereas it gives unstable solution for large values of α .

3.2.3 Particular solution

Again, we solve the field equations (27) and (28) for the same particular values of γ and n , i.e., $\gamma = \frac{1}{\sqrt{6\alpha}}$ and $n = \frac{2}{3}$ as described in Sect. 2.2.3. Considering (17) and (18) the field equations (27) and (28) yield

$$\epsilon \dot{\psi}^2 = -2\beta e^{-\frac{1}{\sqrt{6\alpha}}t}, \quad (36)$$

and

$$V(t) = \frac{2}{9\alpha} \frac{\sqrt{e^{\frac{7}{\sqrt{6\alpha}}t} (2\beta + e^{\frac{1}{\sqrt{6\alpha}}t})}}{(\beta + e^{\frac{1}{\sqrt{6\alpha}}t})^4}. \quad (37)$$

We see that for normal tachyonic field ($\epsilon = 1$), $\dot{\psi}^2$ is negative for any positive values of α but it is positive for phantom tachyonic field ($\epsilon = -1$). Therefore, we shall find the solution for phantom tachyonic field. For $\epsilon = -1$ and considering the positive sign of $\dot{\psi}$ in (36) we integrate to get

$$\psi(t) = -\sqrt{48\alpha\beta} e^{-\frac{1}{\sqrt{6\alpha}}t}, \quad (38)$$

where the integration constant is taken to be zero for simplicity.

The potential function V can be expressed in terms of ψ as

$$V(\psi) = \frac{2\sqrt{(\frac{48\alpha\beta}{\psi^2})^7 (2\beta + \frac{48\alpha\beta}{\psi^2})}}{9\alpha(\beta + \frac{48\alpha\beta}{\psi^2})}. \quad (39)$$

Figure 9 shows the graph between V and ψ and it is to be seen that V increases as ψ increases. The energy density ρ_ψ and pressure p_ψ are respectively given by

$$\rho_\psi = \frac{V(\psi)}{\sqrt{1 + \dot{\psi}^2}} = \frac{2}{9\alpha} \frac{\sqrt{e^{\frac{7}{\sqrt{6\alpha}}t} (2\beta + e^{\frac{1}{\sqrt{6\alpha}}t})}}{(\beta + e^{\frac{1}{\sqrt{6\alpha}}t})^4 \sqrt{1 + 2\beta e^{-\frac{1}{\sqrt{6\alpha}}t}}}, \quad (40)$$

$$p_\psi = -V(\psi)\sqrt{1 + \dot{\psi}^2} = -\frac{2}{9\alpha} \frac{\sqrt{e^{\frac{7}{\sqrt{6\alpha}}t} (\beta + e^{\frac{1}{\sqrt{6\alpha}}t})(1 + 2\beta e^{-\frac{1}{\sqrt{6\alpha}}t})}}{(\beta + e^{\frac{1}{\sqrt{6\alpha}}t})^4}. \quad (41)$$

We find that ρ_ψ grows with time and becomes constant in late time whereas the pressure is always negative. The model has no time-like singularity.

From (29) and (36), the EoS parameter is given by

$$\omega_\phi = -1 - 2\beta e^{-\frac{1}{\sqrt{6\alpha}}t}, \quad (42)$$

which shows that it is always less than -1 but attains to -1 at late time. The solutions are stable for any values of α for any time t . We can say that the emergent-universe is possible with tachyonic phantom field for flat FRW model in HD theory for any positive values of α . It expands exponentially and finally accelerates at late time.

4 Conclusion

In this work, we have studied the possibility of an EU scenario with scalar (or tachyonic) field for a flat FRW model in higher derivative theory of gravity. The solutions have been obtained under the assumption that the dynamics of the universe expansion is determined only by scalar (or tachyonic) field. We have found that the EU scenario is not possible for normal (scalar or tachyon) field in HD theory due to the negativity of kinetic term since it is well noted that in most conventional models $\omega_\phi \geq -1$ and the kinetic term must be positive in case of normal (scalar or tachyon) field. However, the EU is possible for phantom (scalar or tachyon) field for a flat FRW model. The phantom solution (scalar or tachyon) presented in this paper represents a universe which begins with a finite size in the past, grows exponentially and accelerates in late time. The summary of the solutions for phantom (scalar and tachyon) fields are as follows:

In phantom scalar field, we have observed that $\dot{\phi}^2$ increases from zero at infinite past and attains a finite maximum value at finite time and then decreases to zero in late time. We have obtained the scalar potential in terms of cosmic time t and it has been found that it increases with time and attains maximum finite value in late future. Thus, a phantom field rolls to the maximum of its potential with positive potential energy where we find $\omega_\phi < -1$, but it settles into a state with $\omega_\phi = -1$ in late time. In general, the stability of the solution depends on the constraints of the arbitrary parameters. However, The solution is stable for small values of α but it is unstable for large values of coupling parameter. The time for instability can not be determined due to the complicated expressions for scalar field and scalar potential. More precisely, we have discussed the particular solution to describe the behavior of the model. The model has

no time-like singularity for any values of α and the universe accelerates at late time. We can say the EU is possible with phantom scalar field for a flat FRW model in HD theory.

In tachyon phantom field, the $\dot{\psi}^2$ -term decreases from infinity at infinite past to zero at $t = \infty$. It is always positive during the evolution for small values of α . The tachyonic potential increases from zero at infinite past to a flat potential in late time. The stability of the solution can be described as the same manner as discussed in the case of phantom scalar field. We have also discussed the particular solution and have found the expected solution in phantom tachyonic field for any values of α . The model has no time-like singularity at any time during the evolution of the universe. Therefore, the EU may be described in phantom tachyonic field. We find $\omega_\psi < -1$ but it settles into a state with $\omega_\psi = -1$ in late time. In both kinds of fields the energy density are zero at infinite past and grows with time and attains maximum finite value at late time. The models eventually evolve from a finite size in the infinite past into an inflationary stage and finally accelerate at late time. The models have no time-like singularity at any time. The coupling parameter α affects the evolution of the EU in phantom models (scalar or tachyon) as we can observe from the solutions obtained in Sects. 2.2.2 and 2.2.3. In Sect. 2.2.2 the EU is possible only for small values of α but the particular solution presented in Sect. 2.2.3 is true for any positive values of α . Similar interpretation may be given in case of tachyonic phantom field presented in Sects. 3.2.2 and 3.2.3. In the absence of HD theory, i.e., $\alpha = 0$, the solutions for scalar and tachyonic phantom fields as described in Sects. 2.2.2 and 3.2.2 reduce to the solutions obtained by Debnath (2008) in the absence of perfect fluid matter. It is clear that phantom models arising from scalar and tachyon fields with negative kinetic terms produce a rich set of behaviors.

Acknowledgements The authors are thankful to the referee for his constructive comments and suggestions which help us to improve the manuscript. The authors also express their sincere thanks to Prof. M. Sami, Director, Centre for Theoretical Physics, Jamia Millia Islamia University, India for useful discussions.

References

- Banerjee, A., Bandyopadhyay, T., Chakraborty, S.: *Gravit. Cosmol.* **13**, 290 (2007)
- Banerjee, A., Bandyopadhyay, T., Chakraborty, S.: *Gen. Relativ. Gravit.* **40**, 1603 (2008)
- Barrow, J.D., Mimoso, J.P.: *Phys. Rev. D* **50**, 3746 (1994)
- Barrow, J.D., Saich, P.: *Class. Quantum Gravity* **10**, 279 (1993)
- Beesham, A., Chervon, S.V., Maharaj, S.D.: *Class. Quantum Gravity* **26**, 075017 (2009)
- Caldwell, R.R.: *Phys. Lett. B* **545**, 23 (2002); [astro-ph/9908168](#)
- Caldwell, R.R., Kamionkowski, M., Weinberg, N.N.: *Phys. Rev. Lett.* **91**, 071301 (2003)
- Campo de, S., Herrera, R., Labrãna, P.: *J. Cosmol. Astropart. Phys.* **030**, 0711 (2007)
- Capozziello, S., Nojiri, S., Odintsov, S.D.: *Phys. Lett. B* **632**, 597 (2006); [hep-th/0507182](#)
- Chakraborty, S., Debnath, U.: *Int. J. Theor. Phys.* **50**, 80 (2011)
- Debnath, U., Chakraborty, S.: *Int. J. Theor. Phys.* **50**, 2892 (2011)
- Debnath, U.: *Class. Quantum Gravity* **25**, 205019 (2008)
- Elizalde, E., Nojiri, S., Odintsov, S.D.: *Phys. Rev. D* **70**, 043539 (2004); [hep-th/0405034](#)
- Ellis, G.F.R., Maartens, R.: *Class. Quantum Gravity* **21**, 223 (2004)
- Ellis, G.F.R., Madsen, M.S.: *Class. Quantum Gravity* **8**, 667 (1991)
- Ellis, G.F.R., Murugan, J., Tsagas, C.G.: *Class. Quantum Gravity* **21**, 233 (2004)
- Gonzalez, T., Quiros, I.: *Class. Quantum Gravity* **25**, 175019 (2008)
- Guo, Z., Zhang, Y.: *Phys. Rev. D* **71**, 023501 (2005)
- Hao, J., Li, X.: *Phys. Lett. B* **606**, 7 (2005)
- Hao, J.G., Li, X.-z.: *Phys. Rev. D* **66**, 087301 (2002)
- Harrison, E.R.: *Rev. Mod. Phys.* **39**, 862 (1967)
- Ibotombi Singh, N., Singh, S.S., Devi, S.R.: *Astrophys. Space Sci.* **334**, 187 (2011)
- Melchiorri, A., Mersini, L., Odman, C.J., Trodden, M.: *Phys. Rev. D* **68**, 043509 (2003)
- Mimoso, J.P., Wands, D.: *Phys. Rev. D* **51**, 477 (1995)
- Mukerji, S., Chakraborty, S.: *Astrophys. Space Sci.* **331**, 665 (2011)
- Mukerji, S., Chakraborty, S.: *Int. J. Theor. Phys.* **49**, 2446 (2010)
- Mukherjee, S., Paul, B.C., Dadhich, N.K., Maharaj, S.D., Beesham, A.: *Class. Quantum Gravity* **23**, 6927 (2006)
- Mukherjee, S., Paul, B.C., Maharaj, S.D., Beesham, A.: [gr-qc/0505103](#)
- Nojiri, S., Odintsov, S.D.: *Phys. Lett. B* **562**, 147 (2003a); [hep-th/0303117](#)
- Nojiri, S., Odintsov, S.D.: *Phys. Rev. D* **68**, 123512 (2003b)
- Nojiri, S., Odintsov, S.D.: *Gen. Relativ. Gravit.* **38**, 1285 (2006); [hep-th/0506212](#)
- Nojiri, S., Odintsov, S.D.: *J. Phys. Conf. Ser.* **66**, 012005 (2007a); [hep-th/0611071](#)
- Nojiri, S., Odintsov, S.D.: *Int. J. Geom. Methods Mod. Phys.* **4**, 115 (2007b); [hep-th/0601213](#)
- Nojiri, S., Odintsov, S.D.: *Phys. Rep.* **505**, 144 (2011); [arXiv:1011.0544 \[gr-qc\]](#)
- Padmanabhan, T.: *Phys. Rev. D* **66**, 021301 (2002); [hep-th/0204150](#)
- Padmanabhan, T.: *Phys. Rep.* **380**, 235 (2003); [hep-th/0212290](#)
- Paul, B.C., Ghose, S.: *Gen. Relativ. Gravit.* **42**, 795 (2010)
- Paul, B.C., et al.: *Mon. Not. R. Astron. Soc.* **413**, 686 (2011)
- Paul, B.C., et al.: *Mon. Not. R. Astron. Soc.* **407**, 415 (2010)
- Paul, B.C.: *Pramana J. Phys.* **53**, 833 (1999)
- Peebles, P.J.E., Ratra, B.: *Rev. Mod. Phys.* **75**, 559 (2003)
- Perlmutter, S., et al.: *Astrophys. J.* **517**, 565 (1999)
- Riess, A.G., et al.: *Astron. J.* **116**, 1009 (1998)
- Riess, A.G., et al.: *Astrophys. J.* **560**, 49 (2001)
- Riess, A.G., et al.: *Astrophys. J.* **607**, 665 (2004)
- Sahni, V., Starobinsky, A.A.: *Int. J. Mod. Phys. D* **9**, 373 (2000)
- Sahni, V., Sami, M., Souradeep, T.: *Phys. Rev. D* **65**, 023518 (2002)
- Sami, M.: *Mod. Phys. Lett. A* **19**, 1509 (2004a)
- Sami, M.: *Pramana J. Phys.* **62**, 765 (2004b)
- Schmidt, B.P., et al.: *Astrophys. J.* **507**, 46 (1998)
- Shapiro, I.L., Sola, J.: *Phys. Lett. B* **682**, 105 (2009)
- Singh, C.P., Singh, V.: *Mod. Phys. Lett. A* **26**, 1495 (2011)
- Singh, P., Sami, M., Dadhich, N.: *Phys. Rev. D* **68**, 023522 (2003)
- Spergel, D.N., et al.: *Astrophys. J. Suppl. Ser.* **148**, 175 (2003)
- Spergel, D.N., et al.: *Astrophys. J. Suppl. Ser.* **170**, 377 (2007)
- Starobinsky, A.A.: *Phys. Lett. B* **91**, 99 (1980)
- Tegmark, M., et al.: *Astrophys. J.* **606**, 702 (2004)
- Zimdahl, W., Pavón, D., Chimento, L.P.: *Phys. Lett. B* **521**, 133 (2001)
- Zlatev, I., Wang, L., Steinhardt, P.J.: *Phys. Rev. Lett.* **82**, 896 (1999)

Flow-based load-balancing architecture for the agile all-photonic network

Imad Khazali · Anjali Agarwal

Received: 20 March 2011 / Accepted: 6 December 2011
© Springer Science+Business Media, LLC 2011

Abstract A novel routing architecture that balances incoming Internet flows over the agile all-photonic network (AAPN) is proposed. The architecture is based on the adaptive highest random weight (adaptive HRW) algorithm proposed to design load-balanced Internet routers. Extensive numerical evaluation of static and adaptive variations of the routing architecture is studied, and their effect on the network performance in terms of packet drop and flow remapping is presented. The architecture can be seen as a combination of adaptive core node scheduling and adaptive load balancing at the edge nodes. It is stateless and can compute routes quickly based on the packet flow identifier.

Keywords Load balancing · Flow-based routing · Agile all-photonic network · PetaWeb network

1 Introduction

ISPs are facing challenges in provisioning their network resources due to the rapid growth in the Internet users and the complexity of its traffic patterns. Many emerging applications like voice over IP are characterized by highly variable traffic that is very difficult to predict and estimate. Research has been conducted to design high-speed, high-capacity agile networks that can handle the rapid growth in Internet users and their high traffic volume; the agile all-photonic network (AAPN) is an example of such networks [1,2]. The AAPN

research originates from the research into the PetaWeb network [3–6]. The AAPN project is the result of collaboration from five universities and seven telecommunication companies [7].

The AAPN network consists of a number of electro-photonic edge nodes that are interconnected by a number of photonic core nodes in an overlaid star topology, see Fig. 1. The network deploys the optical TDM technique at the edge and core nodes with each timeslot, T_s , taking $10\mu s$ to transmit. An edge node performs traffic aggregation where IP packet flows are terminated and put into timeslots before transmission. The timeslots are then sent to a virtual output queue (VOQ) that is associated with a destination edge node and is served by an outgoing wavelength to the core node. The network agility is provided by its ability to allocate bandwidth on demand at the timeslot granularity.

A core node is a layered space switch, where each space switch is used to switch timeslots on a specific wavelength, see Fig. 2. Timeslot allocation is performed every frame using schedulers running at the core nodes [8–11]. The frame is a fixed number of consecutive timeslots. A scheduler is associated with each wavelength and is responsible for allocating timeslots on that wavelength. The edge nodes signal their timeslot requests to the core nodes every frame [12]. Using the requests collected, the scheduler computes the allocation matrix used to reconfigure the space switch and signals it back to the different edge nodes.

2 Motivation and application

In [13], routing at the connection level has been studied and simulated. The methods perform connection admission control each time a new connection request is received; if no timeslot resources are available on the selected path, the

I. Khazali (✉) · A. Agarwal
Electrical and Computer Engineering Department,
Concordia University, 1515 St. Catherine West,
Montreal, H4G 2W1, Canada
e-mail: ikhazali@encs.concordia.ca

A. Agarwal
e-mail: aagarwal@encs.concordia.ca

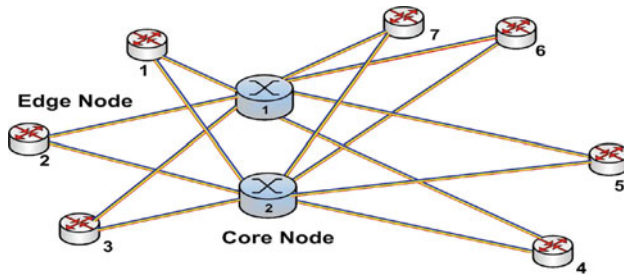


Fig. 1 AAPN with two core nodes interconnecting seven edge nodes

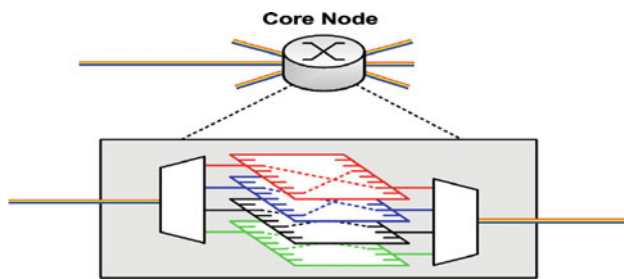


Fig. 2 AAPN layered core node has a space switch for each wavelength

connection is rejected. In [14], two-phase routing [15, 16] has been used to eliminate the need for adaptive scheduling at the core nodes. The method replaces the adaptive scheduler [8–11] with a fixed scheduler that can handle any input traffic matrix within the boundaries of the hose traffic model [17]. The method routes at the timeslot level and so requires resequencing at the destination edge nodes. Since the traffic travels the network twice, end-to-end delay becomes a serious issue when deployed in a WAN environment. In [18] and [19], routing and protection of MPLS LSPs over the AAPN network have been studied. The methods deploy and use the AAPN network as the OSPF backbone area.

Our work focuses on studying the problem of deploying AAPN as the backbone network for ISPs where IP routers are interconnected by the AAPN network, see Fig. 3. More specifically, it focuses on designing a routing architecture for balancing the Internet flows over the AAPN network while reducing packet reordering within one flow identified

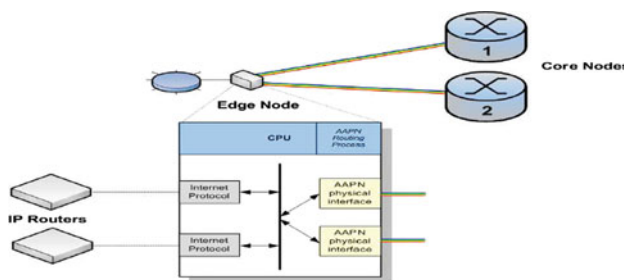


Fig. 3 AAPN network interconnects IP routers using the electro-phonic edge nodes

by common fields within the packet header. Since the number of flows is large in the backbone networks, storing flow state in lookup tables can limit the network performance. Hence, the routing architecture should eliminate the need for flow lookup tables.

The contribution of this paper is threefold. First, we extend the application of the highest random weight (HRW) algorithm to the area of load balancing in backbone networks. The algorithm has its root usage in the area of load balancing for Web caches [20] and was later extended for designing load-balanced IP routers [21]. Second, we propose a routing architecture that balances incoming Internet flows over the AAPN network. It is based on the adaptive HRW mapping algorithm [21]. We present an extensive numerical evaluation of static and adaptive variations of the routing architecture and study their effect on the network performance in terms of packet drop and flow remapping. Third, we describe an enhancement of the adaptive HRW algorithm, called minimal remapping adaptive load balancing. It uses a triggering policy that reduces the number of flows remapped while keeping the IP router balanced.

The rest of the paper is organized as follows: in Sect. 3, we present background information about the Adaptive HRW algorithm. In Sect. 4, we present the architecture for load-balancing incoming Internet flows over the AAPN network. Sect. 5 presents the adaptive HRW algorithm with the minimal flow remapping triggering policy. In Sect. 6, we present our simulation environment and results. Finally, in Sect. 7, we present our conclusions and future work.

3 Background: the adaptive HRW algorithm

The algorithm, [21], balances the incoming processing load among the different network processor units (NPUs) in the router. It dynamically maps incoming packet flows to NPUs using a weighted hash function while preserving the minimal disruption property in [20]. The mapping is performed using the HRW hash function over the flow identifier \mathbf{v} [20, 22]. Periodically, the workload intensity of each NPU is measured and forwarded to a central processor (CP).

3.1 Adaptive HRW mapping policy

Mapping of packets with a flow identifier vector \mathbf{v} is computed as follows:

$$f(\mathbf{v}) = j$$

$$\Leftrightarrow$$

$$x_j g(\mathbf{v}, j) = \max_{k \in \{1 \dots m\}} x_k g(\mathbf{v}, k) \quad (1)$$

where $x_j \in R^+$ is the weight assigned to NPU j and $j \in \{1 \dots m\}$, m is the number of NPUs, $g(\mathbf{v}, j)$ is a

pseudorandom function with $g : \mathbf{v} \times \{1 \dots m\} \rightarrow (0, 1)$ (i.e., $g(\mathbf{v}, j)$ is assumed to be a random variable in $(0, 1)$ with uniform distribution). The weights $\mathbf{x} = (x_1 \dots x_m)$ determine the fraction of the identifier vector space assigned to each NPU and has a 1-to-1 correspondence with the partition vector \mathbf{p} in [20].

3.2 Adaptive HRW triggering policy

The policy exploits two dynamic thresholds to determine whether an NPU is underutilized or overutilized. To evaluate the status of individual NPUs, periodic NPU workload intensity $\rho_j(t)$ is measured and filtered every ΔT :

$$\bar{\rho}_j(t) = \frac{1}{r} \rho_j(t) + \frac{r-1}{r} \bar{\rho}_j(t - \Delta T) \quad (2)$$

where $\bar{\rho}_j(t)$ is the filtered workload intensity and r is the filtering constant. A similar measure is used for the filtered total system workload intensity $\bar{\rho}(t)$:

$$\bar{\rho}(t) = \frac{1}{r} \rho(t) + \frac{r-1}{r} \bar{\rho}(t - \Delta T) \quad (3)$$

The policy uses the dynamic threshold $\varepsilon_\rho(t)$ defined in Eq. (4) and a fixed hysteresis bound $\varepsilon_h > 0$ to prevent adaptation within the interval defined in Eq. (5):

$$\varepsilon_\rho(t) = \frac{1}{2} (1 + \bar{\rho}(t)) \quad (4)$$

$$[(1 - \varepsilon_h) \bar{\rho}(t), (1 + \varepsilon_h) \bar{\rho}(t)] \quad (5)$$

3.3 Adaptive HRW adaptation policy

The policy preserves the minimal disruption property by having a subset of the elements in the weight vector \mathbf{x} multiplied by a constant factor α . The following equation is used to compute α when the system is underutilized (i.e., $\bar{\rho}(t) \leq 1$) and one or more NPUs are overutilized (i.e., $\bar{\rho}_j(t) > \varepsilon_\rho(t)$):

$$\alpha(t) = \left(\frac{\varepsilon_\rho(t)}{\min \{ \bar{\rho}_j(t), \bar{\rho}_j(t) > \varepsilon_\rho(t) \}} \right)^{1/m} \quad (6)$$

Conversely, α is computed in a symmetrical way when the system is overutilized (i.e., $\bar{\rho}(t) > 1$).

4 Adaptive routing architecture for the AAPN network

In this section, we describe the adaptive routing architecture for the AAPN network. The architecture is distributed and is implemented at the different edge nodes in the network. Figure 4 represents the block diagram of the routing architecture at the source edge node with ID equal to one. The diagram consists of two processing stages: a classification stage and a two-level mapping stage associated with every destination edge node in the AAPN network. At the classification stage, the destination edge node of the incoming packets is determined using the AAPN routing tables described in [23]. The classified packets associated with a destination edge node are then mapped twice: the first map $f_c(\mathbf{v})$, called core selection, routes the packets to a core node while, the second map $f_w^c(\mathbf{v})$, called wavelength selection, routes the

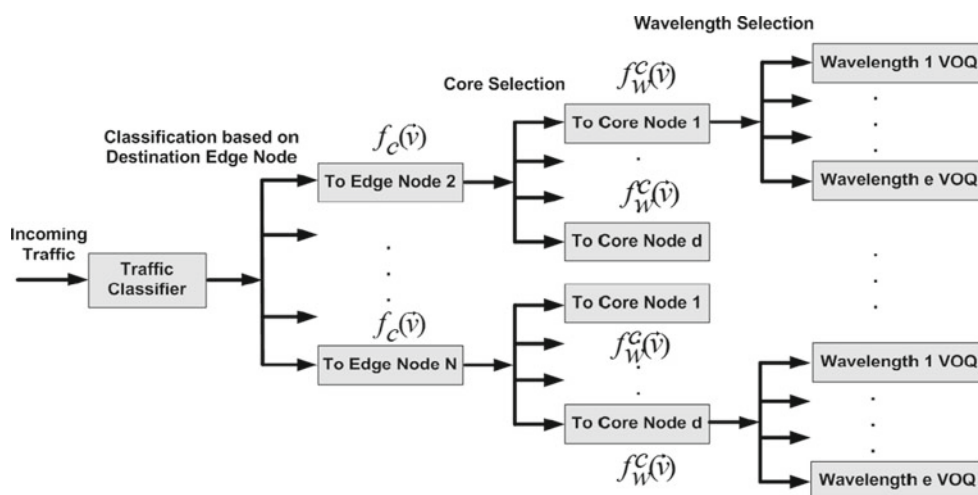


Fig. 4 Core and wavelength selections work in tandem with no interaction to balance the incoming Internet flows over the AAPN network. For a given source–destination edge node pair, $f_c(\mathbf{v})$ balances the Internet flows over the fiber link paths going through the different core nodes, then $f_w^c(\mathbf{v})$ balances the Internet flows mapped to the fiber link path

going through core node c over the different wavelengths in this path. The subscripts c in $f_c(\mathbf{v})$ and w in $f_w^c(\mathbf{v})$ are used to define core and wavelength selection types, while superscript c in $f_w^c(\mathbf{v})$ defines the instance of wavelength selection associated with core node c selected by the $f_c(\mathbf{v})$ mapping function

packets to a wavelength through core node c selected by $f_c(\mathbf{v})$. The mapped packets are then stored in the virtual output queue (VOQ) associated with the destination edge node on the selected wavelength. The $f_c(\mathbf{v})$ and $f_w^c(\mathbf{v})$ mappings route packets at the flow level and are computed using Eq. (1). Each core node is assigned a mapping weight from the weight vector $\mathbf{x} = (x_1 \dots x_d)$, where d is the number of core nodes. Each wavelength is assigned a mapping weight from the weight vector $\mathbf{y} = (y_1 \dots y_e)$, where e is the number of wavelengths through the core node. For AAPN networks with single wavelength per fibre, only the $f_c(\mathbf{v})$ mapping function is used.

Ideally, the two-level mapping functions should balance the incoming traffic over the different fibre links and wavelengths of the AAPN network, but in reality, the functions could result in gross imbalance due to the Internet flow duration distribution [24] and flow identification distribution [25]. Thus, an adaptation loop is needed to keep the fibre links, and wavelengths within, from being congested. It adapts the weight vectors \mathbf{x} and \mathbf{y} , based on the fibre links and wavelengths traffic loads, using Eq. (6). A traffic load is measured every frame and is defined as the percentage of timeslots requested per frame.

Compared to the Adaptive HRW algorithm, the mapping in AAPN consists of two functions working in tandem with no interaction. Also, in the adaptive HRW, the CP triggers adaptation of the weights based on the workload measurements of the set of NPU's, while in AAPN mappings, two sets of traffic load measurements are used to trigger weights adaptation. For the $f_c(\mathbf{v})$ function associated with a source–destination edge node pair, the two traffic load measurement sets are the set of traffic load measurement of the downstream fibre links associated with the source edge node and the set of traffic load measurement of the upstream fibre links associated with the destination edge node. For the $f_w^c(\mathbf{v})$ function associated a source–destination edge node pair and core node c , the two traffic load measurement sets are the set of traffic load measurement of the downstream wavelengths on the fibre link from the source edge node to core node c and the set of traffic load measurement of the upstream wavelengths on the fibre link from core node c to the destination edge node.

Notice that triggering weight adaptation by two interrelated sets of traffic load measurements could result in instability and oscillations (i.e., triggering adaption to balance the traffic load over the downstream set of fibre links (wavelengths) could result in imbalance on the upstream set of fibre links (wavelengths) and vice versa). For this, one major objective of the simulations study is to prove the stability of the weights adaption triggering policy.

The adaptation triggering policy for the AAPN network is different from the policy used in the adaptive HRW algorithm. The next two sections describe two variations of the AAPN adaptation policy.

4.1 AAPN adaptation triggering policy

The default triggering policy applies to the adaptation of both weight vectors \mathbf{x} and \mathbf{y} . The term channel is used in this section to generalize the description of the triggering policy, but when used for core selection, it means a fiber link, and when used for wavelength selection, it means a wavelength.

We categorize the channels into downstream and upstream types. A downstream channel connects a source edge node to a core node, while an upstream channel connects a core node to a destination edge node. The traffic load on a downstream channel originates at the source edge node and is destined to the other edge nodes, while the traffic load on an upstream channel originates at the source edge nodes and is destined to the destination edge node. The channel set is defined differently for the fiber links and wavelengths. The downstream fiber link set associated with an edge node is defined as the set of links connecting this edge node to all the core nodes, while the upstream fiber link set associated with an edge node is defined as the set of links connecting the core nodes to this edge node. The downstream wavelength set associated with an edge node is defined as the set of wavelengths connecting this edge node to a core node, while the upstream wavelength set associated with an edge node is defined as the set of wavelengths connecting the core node to this edge node.

The policy uses the two channel sets' traffic loads to adapt the weight vectors associated with a source–destination edge node pair. In cases where both traffic load sets require adaptation, only one set chosen randomly is allowed to trigger the adaptation. The traffic loads for the two sets of channels are measured at different points in the network. The downstream channel set traffic loads are measured at the source edge node, while the upstream channel set traffic loads are measured at the core nodes. Measurement and filtering are performed periodically every frame, while the computation of dynamic threshold, channel set average traffic load, and weight vectors adaptation is performed at the edge nodes every ΔT . ΔT is chosen to be an integer multiple of the frame size and greater than the maximum round trip signaling delay between the edge and core nodes. This gives the weight vector changes enough time to propagate and take effect at the core nodes.

The traffic load of channel j , $\rho_j(t_n)$, is computed every frame as follows:

$$\rho_j(t_n) = \frac{\lambda_j(t_n)}{F} \quad (7)$$

where $\lambda_j(t_n)$ is the total number of timeslots requested in the n th frame, t_n is a discrete time measured at the end of each frame, and F is the frame size in timeslots.

Notice that if channel j is a fiber link, then $\lambda_j(t_n)$ represents the total timeslots requested on all z wavelengths that goes through the fiber link and F is replaced by zF .

The channel filtered traffic load, $\bar{\rho}_j(t_n)$, is also computed every frame as follows:

$$\bar{\rho}_j(t_n) = \frac{1}{r} \rho_j(t_n) + \frac{r-1}{r} \bar{\rho}_j(t_n - t_{n-1}) \quad (8)$$

where $t_n - t_{n-1} = F * T_s$ is the frame size in seconds and r is the filtering constant computed using Eq. (9) to reduce the effect of short term fluctuations in the channel traffic load.

$$r = \frac{\Delta T}{F * T_s} \quad (9)$$

The channel set average traffic load, $\bar{\rho}(t_n)$, is computed every ΔT as follows:

$$\bar{\rho}(t_n) = \frac{\sum_{j=1}^L \bar{\rho}_j(t_n)}{L} \quad (10)$$

where t_n is the time at the end of the n th frame and L is the number of channels in the channel set.

Based on the computed values, a channel set is considered underutilized if $\bar{\rho}(t_n) \leq 1$ and overutilized if $\bar{\rho}(t_n) > 1$. A channel is considered overutilized if $\varepsilon_\rho(t_n) \leq \bar{\rho}_j(t_n)$ and underutilized if $\varepsilon_\rho(t_n) > \bar{\rho}_j(t_n)$ where the dynamic threshold, $\varepsilon_\rho(t_n)$, is computed every ΔT using Eq. (4).

The policy triggers adaptation of the weight vectors when imbalance occurs in the network. For example, assume that the upstream channel set going to a destination edge node is underutilized (overutilized) and one or more channels within the set are overutilized (underutilized), this will force all edge nodes to adapt their weight vectors to that destination edge node. In another example, assume that the downstream channel set coming from an edge node is underutilized (overutilized) and one or more channels within the set are overutilized (underutilized), this will force the edge node to adapt his weight vectors to all destination edge nodes.

4.2 AAPN minimal flow remapping triggering policy

The default triggering policy requires all edge nodes to adapt their weight vectors when the channel set is underutilized (overutilized) and one or more channels within the set is overutilized (underutilized). In this section, we describe a variation of the policy that triggers those edge nodes that are most responsible for the channel state. In this variation, not only a channel total traffic load is measured and filtered every frame, but the traffic load contributed by each source–destination edge node pair is also measured and filtered using Eq. (11). The equation is interpreted differently depending on the channel type. For a downstream channel l connecting a source edge node to a core node, $\bar{R}_x^l(t_n)$ and $R_x^l(t_n)$ are the filtered traffic load and the traffic load to destination edge node x in the n th frame, respectively. For an upstream channel l connecting a core node to destination edge node, $\bar{R}_x^l(t_n)$ and $R_x^l(t_n)$ are the filtered traffic load and

the traffic load from source edge node x in the n th frame, respectively.

$$\bar{R}_x^l(t_n) = \frac{1}{r} R_x^l(t_n) + \frac{r-1}{r} \bar{R}_x^l(t_n - t_{n-1}) \quad (11)$$

To identify those edge nodes responsible for channel l state, we define the following two dynamic thresholds that are computed every ΔT :

$$\begin{aligned} \varepsilon_u(t_n) &= \bar{R}^{\text{mean}}(t_n) + \bar{R}^{\text{SD}}(t_n) \\ \varepsilon_o(t_n) &= \bar{R}^{\text{mean}}(t_n) - \bar{R}^{\text{SD}}(t_n) \end{aligned} \quad (12)$$

where $\bar{R}^{\text{mean}}(t_n)$ is the mean value and $\bar{R}^{\text{SD}}(t_n)$ is the standard deviation of the filtered traffic loads at the end of the n th frame:

$$\bar{R}^{\text{mean}}(t_n) = \frac{\sum_x^N \bar{R}_x^l(t_n)}{N-1} \quad (13)$$

$$\bar{R}^{\text{SD}}(t_n) = \sqrt{\frac{\sum_x^N \left(\bar{R}_x^l(t_n) - \bar{R}^{\text{mean}}(t_n) \right)^2}{N-1}} \quad (14)$$

where N is the number of edge nodes in the network.

Based on the computed values, if the set of downstream channels from a source edge node is underutilized and one of the channels l is overutilized, then destination edge node x is contributing to the channel state if $\varepsilon_u(t_n) \leq \bar{R}_x^l(t_n)$. Conversely, if the set of downstream channels is overutilized and one of the channels is underutilized, then the traffic load to the destination edge node x is contributing to the channel state if $\varepsilon_o(t_n) \geq \bar{R}_x^l(t_n)$. The traffic load to the destination edge node x is not contributing to the channel state if $\varepsilon_o(t_n) < \bar{R}_x^l(t_n) < \varepsilon_u(t_n)$. Similar argument applies to the upstream channels where the traffic is going to a destination edge node.

5 Adaptive HRW with minimal flow remapping

The minimal flow remapping triggering policy can be used to enhance the adaptive HRW algorithm. In addition to measuring and filtering the workload intensity at each NPU, the workload intensity from each input port is also measured and filtered using an equation similar to (11); where l and x represent the NPU and input port respectively. The idea is that when weight vector adaption is needed, only the subset of input ports responsible for the NPU(s) state is forced to adapt their weight vectors. To do this, the CP uses dynamic thresholds similar to Eq. (12) to determine, for each NPU, which input ports are responsible for its state. For example, if the IP router is underutilized and one of the NPUs is overutilized, the CP determines which input ports are overutilizing that NPU and forces them to adapt their weight vectors.

6 Numerical results

The OPNET tool has been used to simulate an AAPN network with 16 edge nodes and 8 core nodes. Since core and wavelength selections work independently, fiber links with one wavelength are used. Each wavelength has a capacity of 1 Gb/s. The round trip delay, RTD , is set to 40 ms and the frame size on each wavelength, F , is set to 100 timeslots.

The objectives of the simulations are threefold. First, the performance of the routing architecture is studied and compared to the shortest path routing from the literature. Second, the performance of the routing architecture with three different channel set traffic load measurements is studied: using traffic load measurements from the downstream channel set, upstream channel set, and downstream and upstream channel sets. Third, the performance of the routing architecture with minimal flow remapping is studied. Any edge node can be selected to study the behavior; we choose edge node number 8.

6.1 Simulations input

Each edge node generates self-similar traffic represented by the H-FSNDP fractal point process [26]. In the H-FSNDP model, the flow arrival process follows a Poisson model and the flow duration is heavy tailed Pareto model. Packets' inter-arrival time within a flow is exponentially distributed. The following parameters describe the input traffic, the parameters are chosen to keep the load on the network close to 1.0:

1. Flow average arrival rate is 223,000 flow/s.
2. Hurst parameter is 0.8 and the Fractal Onset Time Scale is 0.001.
3. Average flow duration is 0.3 s.
4. Flow packet average arrival rate is 128 packets/s.
5. Packet size is exponentially distributed with average size of 1024 bits (i.e., on average, each timeslot carries $(10^9 * T_s)/1024 = 10$ packets).

The incoming flows at each edge node are uniformly distributed to all other edge nodes in the network. The flow identifier distribution is a truncated normal distribution $N(0, 1)$ out of the 32-bit integer space [21]. This approximates the distribution of IP source and destination addresses as described in [25].

6.2 AAPN routing architecture parameters

Link traffic loads at the edge and core nodes are computed every frame, where the frame length is equal to $100 * T_s = 1$ ms. The adaptation period, ΔT , is set to 100 ms (i.e., k is set to 2.5). The Fibonacci hashing used in [21] is used here to compute $g(\mathbf{v}, j)$. The filtering constant, r , is set to 100. The

hysteresis bound, ε_h , is set to 0.01 and the initial values for the adaptation weights are set according to the link capacities (i.e., $x_c = 1.0$) [20].

6.3 Routing architectures performance comparison simulations

The behavior of three different routing architectures are compared in this section: (1) a static version of the routing architecture with no adaptation (static load balancing); (2) an adaptive version of the routing architecture with adaptation based on the upstream and downstream link sets traffic load (adaptive load balancing); and (3) the shortest path routing, where the traffic between any edge node pair is sent through the core node that is part of the shortest path between the edge node pair.

Figure 5 shows the behavior of the different architectures when deployed in the AAPN network. Figure 5e, f show how the traffic load on the links remain within the closest vicinity of the average traffic load when the adaptive load balancing is deployed. They also show how stable the adaptive load balancing is even when the weights' adaptation is triggered by the downstream and upstream link sets traffic load. Figure 5a, b shows how spread the traffic loads are around the average (some links have zero traffic load); this is due to the combination of the shortest path routing and the flow duration Pareto distribution.

Figure 6 shows the requests dropped on the downstream and upstream links every ΔT period. As mentioned earlier, each request is for a timeslot, and each timeslot can carry up to 10 packets on average. The figures show how the adaptive load balancing outperforms the static load balancing. Table 1 summarizes the total requests dropped, as a percentage of the total requests sent on the downstream and upstream link sets, for the different architectures.

Figure 7a shows the number of flows appearing and the flows remapped every ΔT period when the adaptive load balancing is deployed. The thick line at the top is actually 15 lines, each representing the flows leaving edge node 8 and going to each of the other 15 edge nodes every ΔT . From the figure, the flows going to each node is around 6,000, which is expected due to the adaptive load balancing. Each curve at the bottom is associated with a destination edge node, it represents the number of flows remapped every ΔT . The figure shows the stability of remapping for the different destination edge nodes, and it also shows that less than 1% of the appearing flows is actually remapped.

6.4 Routing architecture with different link sets measurement simulations

The behavior of three different routing architectures are compared in this section: (1) an adaptive version of the routing

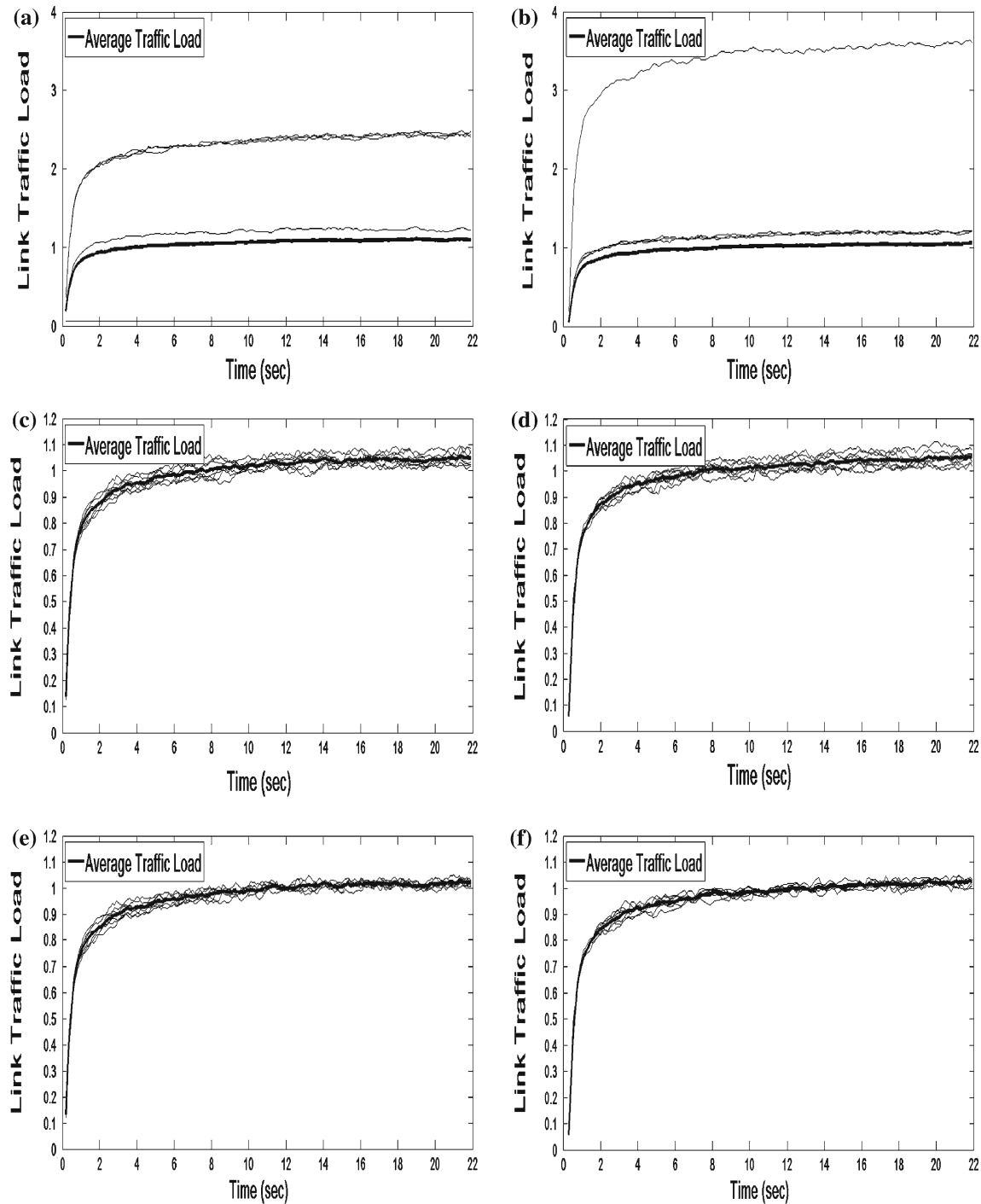


Fig. 5 **a, c, e** Shows the traffic load on the downstream links from edge node 8, while **b, d, f** shows the traffic load on the upstream links to edge node 8. Notice that the number of links in each set is equal to the number of core nodes (i.e., $L = 8$ links). The figures show the link traffic loads when shortest path routing (**a, b**), static load balancing

(**c, d**), and adaptive load balancing (**e, f**) are deployed. The average traffic load for the link sets is shown in **bold**; it is used as the ideal reference traffic load. Notice that the y-axes scale for (**a, b**) is higher than that for (**c-f**)

architecture with adaptation based on the downstream link set traffic load (downstream adaptive load balancing); (2) an adaptive version of the routing architecture with adaptation

based on the upstream link set traffic load (upstream adaptive load balancing); and (3) an adaptive version of the routing architecture with adaptation based on the downstream and

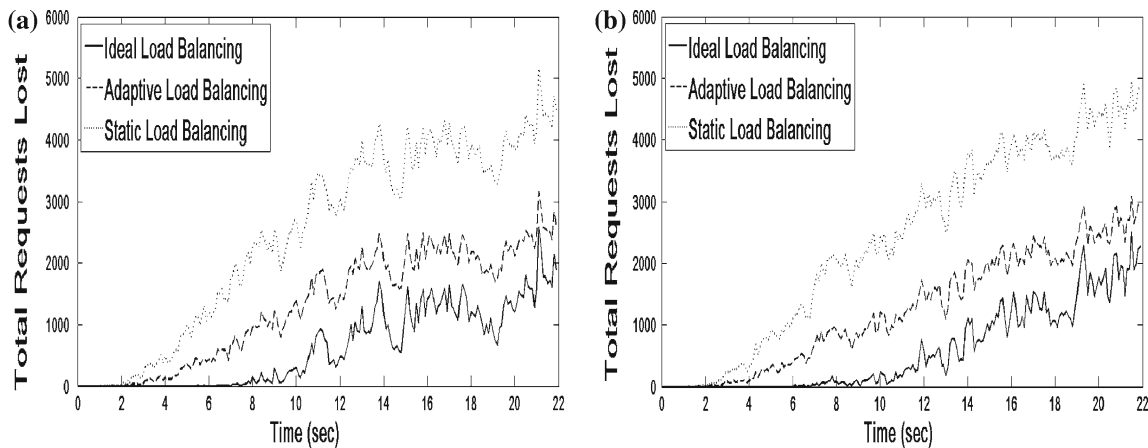


Fig. 6 **a** Shows the requests dropped on the downstream links of edge node 8, while **b** shows the requests dropped on the upstream links of edge node 8. The figures show the number of requests dropped every ΔT period when adaptive load balancing and static load balancing are deployed. The ideal load balancing is also shown for comparison. The ideal request drop is computed as the difference between the requests

received and the requests the link set can handle in ΔT period. The requests the link set can handle in $\Delta T = 0.1$ s are equal to *number of links in the link set (8) * number of frames in ΔT (100) * Frame size in requests (100)*; any requests received in excess of this value (i.e., 80,000) are dropped for the ideal load balancing

Table 1 Requests dropped comparison between the static and adaptive load balancing

	Downstream links (%)	Upstream links (%)
Ideal LB	0.80	0.76
Adaptive LB	1.67	1.60
Static LB	3.10	3.00

upstream link sets traffic load (adaptive load balancing from the previous section).

Figure 8 shows the behavior of the routing architecture when the downstream adaptive load balancing and the upstream adaptive load balancing are deployed. Figure 8a shows how the traffic load on the downstream links remain within the closest vicinity of the average traffic load when the adaptation triggering policy is based on traffic loads from the downstream links, while Fig. 8b shows how the traffic load on the upstream links spreads around the average traffic load. Figure 8c shows how the traffic load on the upstream links remain within the closest vicinity of the average traffic load when the adaptation triggering policy is based on traffic loads from the upstream links, while Fig. 8d shows how the traffic load on the downstream links spreads around the average traffic load. Compared to Fig. 5, it is clear that the adaptive load balancing outperforms the downstream and upstream load balancing by keeping the traffic load within the closest vicinity of the average traffic load for both the downstream and upstream link sets.

Table 2 summarizes the total requests dropped, as a percentage of the total requests sent on the downstream and

upstream link sets, for the different architectures. Compared to Table 1, it shows that the total requests dropped for the upstream links when the downstream adaptive load balancing is deployed and for the downstream links when the upstream adaptive load balancing is deployed are worse than those for the static load balancing.

6.5 Routing architecture with minimal remapping performance simulations

In this section, the behavior of the minimal remapping load-balancing routing architecture is studied and compared to the adaptive load-balancing routing architecture discussed perviously. As mentioned earlier, the objective of this architecture is to reduce the number of flows remapped while keeping the traffic load-balanced over the different links in the network.

Figure 7b shows the number of flows appearing and the flows remapped every ΔT period when the minimal remapping adaptive load balancing is deployed. Compared to the adaptive load-balancing remapping in Fig. 7, the figure shows significant reduction in flow remapping. When adding up the remapped flows over the simulation period, it was found that around 1 and 0.2% of the appearing flows are remapped when the default and minimal flow remapping triggering policies are deployed, respectively. This gives the minimal flow remapping triggering policy a significant reduction in flow remapping compared to the default triggering policy. It should be noted that the results for the minimal flow remapping triggering policy are also applicable to the load-balanced IP routers designed using the adaptive HRW algorithm [21].

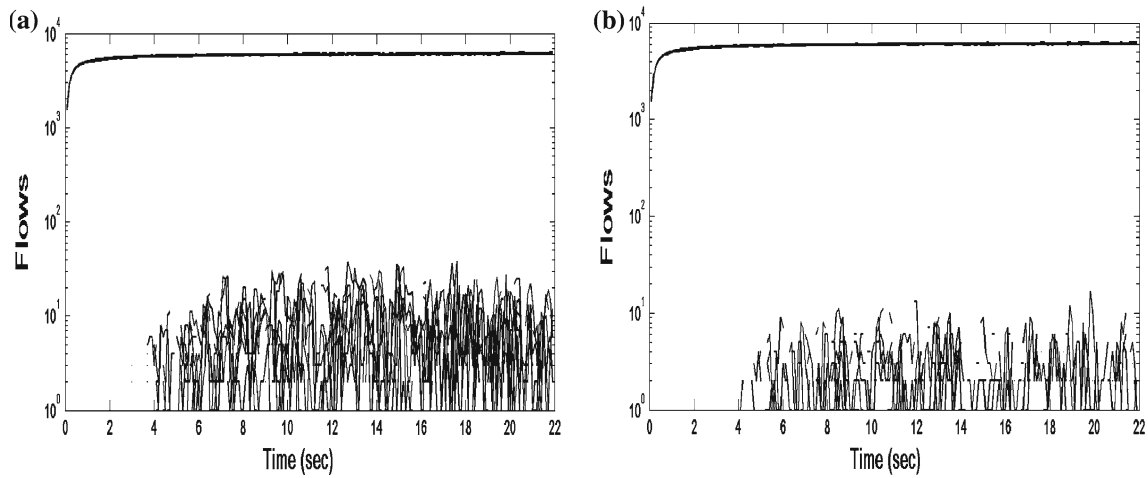


Fig. 7 The figure shows, in a logarithmic scale, the number of flows appearing and the flows remapped every ΔT period for edge node 8 when the adaptive load balancing (a) and the minimal remapping adaptive load balancing (b) are deployed

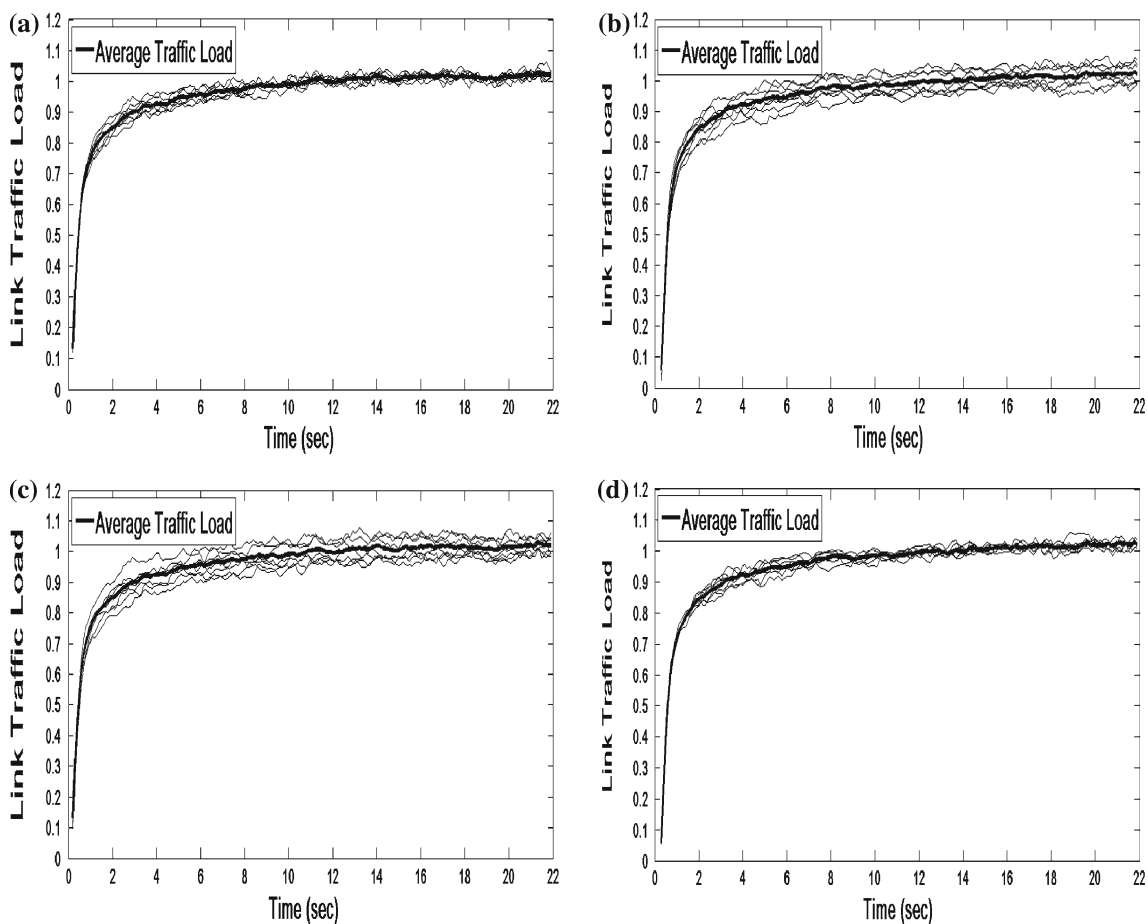


Fig. 8 a, c shows the traffic load on the downstream links from edge node 8, while b, d shows the traffic load on the upstream links to edge node 8. The figures show the link traffic loads when the downstream link set traffic load (a, b) and the upstream link set traffic load (c, d)

are used to trigger vector weights adaptation. The average traffic load for the link sets is shown in **bold**; it is used as the ideal reference traffic load

Table 2 Requests dropped comparison between the downstream, upstream, and adaptive load balancing

	Downstream links (%)	Upstream links (%)
Downstream adaptive LB	1.68	3.40
Upstream adaptive LB	3.50	1.63
Adaptive LB	1.67	1.60

Figure 9 shows how the traffic load on the downstream and upstream link sets remain within the closest vicinity of the average traffic load when the minimal remapping load balancing is deployed.

Table 3 summarizes the total requests dropped, as a percentage of the total requests sent on the downstream and upstream link sets, for the adaptive load balancing and the minimal remapping adaptive load balancing. It shows that the minimal remapping adaptive load balancing has a total request drop that is very close to that of the adaptive load balancing.

7 Conclusions and future work

A novel routing architecture that balances incoming Internet flows over the agile all-photonic network (AAPN) is proposed. The architecture is based on the adaptive highest random weight (adaptive HRW) algorithm proposed to design load-balanced Internet routers. It assigns traffic load-balancing weights to each source–destination edge node pair in the network. The weights are adapted based on the traffic load of the downstream and upstream links in the network. The architecture can be seen as a combination of adaptive core node scheduling and adaptive load balancing at the edge nodes.

Table 3 Requests dropped comparison between the minimal adaptive load balancing and adaptive load balancing

	Downstream links (%)	Upstream links (%)
Minimal adaptive LB	1.68	1.63
Adaptive LB	1.67	1.60

It is stateless and can compute routes quickly based on the packet flow identifier.

We presented an extensive numerical evaluation of static and adaptive variations of the routing architecture and studied their effect on the network performance in terms of packet drop and flow remapping. The first part of the simulation results shows the stability of the adaptive load-balancing routing architecture even when the weights adaptation is triggered by two different groups of traffic load. It also shows that the load on the links remain within the closest vicinity of the average load when the adaptive load-balancing and minimal remapping adaptive load-balancing architectures are deployed with a small fraction of flows remapped. Performance measurements, in terms of requests dropped, show that the adaptive load-balancing architecture significantly outperforms the static load-balancing architecture. The second part of the simulation results shows that neither the downstream nor the upstream load-balancing architecture is enough to ensure balancing on all the links (wavelengths) in the network; the adaptive load-balancing architecture outperforms them both. The third part of the simulation shows that the minimal remapping adaptive load-balancing architecture enhances the adaptive load-balancing architecture while reducing the number of flows remapped.

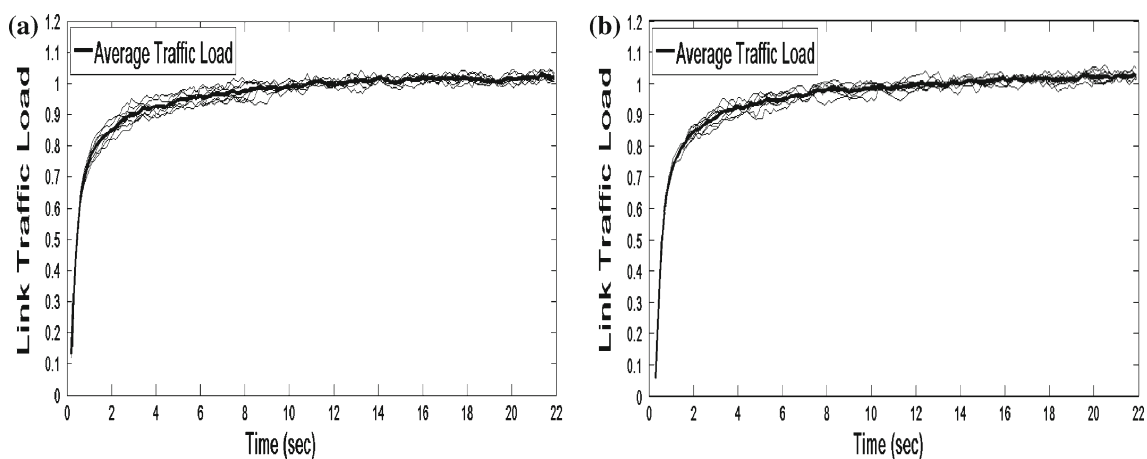


Fig. 9 **a** Shows the load on the downstream links from edge node 8, while **b** shows the load on the upstream links to edge node 8. The average load for the link sets is shown in *bold*; it is used as the ideal reference load

An enhanced version of the adaptive HRW algorithm that uses the minimal flow remapping triggering policy to reduce flow remapping while keeping the IP router balanced is also described. Even though the policy is simulated in the AAPN network, results should also be applicable the adaptive HRW algorithm and the IP router architecture in [21].

Acknowledgments The authors would like to thank OPNET Inc for their university program that gave the access to the OPNET tool.

References

- [1] Bochmann, G., et al.: The Agile All-Photonic Network: An Architectural Outline. IEEE QBSC (2004)
- [2] Mason, L., Vinokurov, A., Zhao, N., Plant, D.: Topological design and dimensioning of agile all-photonic networks. J. Comput. Netw. **50**, 268287 (2006)
- [3] Vickers, R., Betas, M.: PetaWeb Architecture. Toward Natural Networks: International Telecommunication Network Planning Symposium (2000)
- [4] Reinert, A., Sanso, B., Secci, S.: Design optimization of the PetaWeb architecture. IEEE/ACM Trans. Netw. **17**, 332–345 (2009)
- [5] Vickers, R., Beshai, M.: Agile Optical-Core Distributed Packet Switch”. U.S. patent no. 6486983 (2002)
- [6] Blouin, F.J., Lee, A.W., Lee, A.J.M., Beshai, M.: Comparison of two optical-core networks. J. Opt. Netw. **1**(1), 56–65 (2002)
- [7] AAPN Project. <http://www.aapn.mcgill.ca>
- [8] Saberi, N., Coates, M.J.: Minimum Rejection Scheduling in All-Photonic Networks. IEEE BROADNETS (October 2006)
- [9] Saberi, N., Coates, M.J.: Scheduling in overlaid star all-photonic networks with large propagation delays. Photonic Netw. Commun. **17**(2), 157–169 (2009)
- [10] Saberi, N., Coates, M.J.: Bandwidth Reservation in Optical WDM/TDM Star Networks. IEEE QBSC (June 2006)
- [11] Peng, C., Bochmann, G.v., Hall, T.J.: Quick Birkhoff-von Neumann Decomposition Algorithm for Agile All-Photonic Network Cores. IEEE ICC (June 2006)
- [12] Khazali, I., Agarwal, A.: Control Messages Delivery Protocol. IEEE QBSC (May 2010)
- [13] Zheng, J., Peng, C., Bochmann, G.v., Hall, T.J.: Load Balancing in All-Optical Overlaid-Star TDM Networks. IEEE Sarnoff Symposium (March 2006)
- [14] Paredes, S.A., Hall, T.J.: A Load Balanced Agile All-Photonic Network. IEEE ISCC (July 2007)
- [15] Zhang-Shen, R., McKeown, N.: “Designing a Predictable Internet Backbone Network”. Third Workshop on Hot Topics in Network (HotNets-III), (November 2004)
- [16] Kodialam, M., Lakshman, T.V., Sengupta, S.: Efficient and Robust Routing of Highly Variable Traffic. Third Workshop on Hot Topics in Networks (HotNets-III) (November 2004)
- [17] Fingerhut, J.A., Suri, S., Turner, J.S.: Designing least-cost non-blocking broadband networks. J. Algorithms **24**(2), 287–309 (1997)
- [18] He, P., Bochmann, G.v. Routing of MPLS Flows Over an Agile All-Photonic Star Network. IASTED international conference CSA (2006)
- [19] He, P., Bochmann, G.v.: Inter-Area Shared Segment Protection of MPLS Flows Over Agile All-Photonic Star Networks. IEEE Globecom (2007)
- [20] Ross, K.W.: Hash routing for collections of shared web caches. IEEE Netw. **11**(6), 37–44 (1997)
- [21] Kencl, L., Le Boudec, J.Y.: Adaptive load sharing for network processors. IEEE/ACM Trans. Netw. **16**(2), 293–306 (2008)
- [22] Thaler, D.G., Ravishankar, C.V.: Using name-based mappings to increase hit rates. IEEE/ACM Trans. Netw. **6**(1), 1–14 (1998)
- [23] Khazali, I., Vickers, R.: A Reliable Routing Protocol for Agile All-Photonic Networks. IEEE CCECE (May 2008)
- [24] Shi, W., MacGregor, M.H., Gburzynski, P.: Load balancing for parallel forwarding. IEEE/ACM Trans. Netw. **13**(4), 790–801 (2005)
- [25] WAN Traffic Distribution by Address Size, Fix-West Trace. National Lab. For Applied Network Research (NLNR) (May 1997). <http://www.nlanr.net/NA/Learn/Class>
- [26] Ryu, B., Lowen, S.: Fractal Traffic Models for Internet Simulation. IEEE ISCC (July 2000)

Author Biographies



Imad Khazali received his B.Sc. degree in Computer Engineering from Jordan University in Science and Technology (JUST), Jordan, in 1995, and M.Eng. degree in Electrical and Computer Engineering from Concordia University. Presently, he is a Ph.D. student in the Department of Electrical and Computer Engineering at Concordia University, Montreal, Canada. Imad's research interests are in Control Planes for Optical Networks and MPLS Traffic Engineering. He has an industrial experience as a Software Engineer responsible for analyzing, designing, and developing networking protocols such as NetBIOS and SMB protocols. He also worked as an Embedded Software Engineer where he published two white papers in software implementation of AFDX avionics end systems and switches.



Anjali Agarwal received her B.E. degree in Electronics and Communication Engineering from Delhi College of Engineering, India, in 1983, M.Sc. degree in Electrical Engineering from University of Calgary, Canada, in 1986, and Ph.D. degree in Electrical and Computer Engineering from Concordia University, Canada, in 1996. Presently, she is an Associate Professor in the Department of Electrical and Computer Engineering at Concordia University, Montreal, Canada. She has an industrial experience as well as an academic experience. She was a Protocol Design Engineer with Harris Communications, Montreal, where she was providing specifications and design issues for TCP/IP and Voice over IP support for Broadband Wireless Access products. She was with Marconi Communications, Montreal, as Software Engineer, where she was involved in specification, design, development, implementation and maintenance of large-scale real-time embedded software for SONET applications. Dr. Agarwal's current research interests are Voice over Data Networks, Real Time Multimedia Communication over Internet, IP telephony, Quality of Service, and communication protocols.

FRW models with particle creation in Brans-Dicke theory

C.P. Singh

Received: 21 August 2011 / Accepted: 6 December 2011
© Springer Science+Business Media B.V. 2011

Abstract The thermodynamical effect of particle creation on the early evolution of Friedmann-Robertson-Walker universe is analyzed in the context of open thermodynamical systems within the framework of Brans-Dicke theory. The field equations are solved exactly using the “gamma-law” equation of state $p = (\gamma - 1)\rho$, where the adiabatic parameter γ depends on the scale factor of the universe. We assume the functional form of γ in such a way that it describes a unified description of two early phases of the evolution of the universe, viz. *inflationary phase* and *radiation-dominated phase*. The role of Brans-Dicke scalar and creation of matter particles is investigated during the expansion of the universe. It is found that the expansion of the universe is driven by the particle creation in each phase. The physical and geometrical behaviors of the solutions are discussed in detail.

Keywords FRW model · Brans-Dicke theory · Power-law expansion · Particle creation

1 Introduction

In Einstein’s general relativity, the gravitational constant G , velocity of light c and cosmological constant Λ are all proper constants. A conceptually simple way to extend Einstein’s theory of general relativity is to suppose that the gravitational term G is time dependent. The concept of a time—dependent gravitational constant G was first introduced by

Dirac (1937, 1938) based on the large number hypothesis (LNH). A time-dependent G then follows as a natural consequence of the LNH. In the past there were some interesting attempts to generalize the general theory of relativity with variable G . One of the important modifications were proposed by Brans and Dicke (1961), known as Brans-Dicke (BD) scalar-tensor theory of gravitation. In this gravitational theory, in addition to the space time metric, a scalar field ϕ is introduced as a dynamical variable. The scalar field ϕ has the dimension of inverse of the gravitational constant and its role is confined to its effects on gravitational field equations. The introduction of the scalar field in this theory makes it more consistent with Mach’s principle since Mach’s principle is not substantiated by general relativity. In BD theory, a dimensionless free coupling parameter ω is introduced between the scalar and tensor components of gravitation. From observational point of view, the BD theory is consistent for $\omega \geq 500$ (Will 1981). However, there is no restriction on the value of ω from a cosmological stand point, and BD theory goes over to general relativity at the limit of $\omega \rightarrow \infty$, $\phi = \text{const.} = G^{-1}$. A detailed survey of the Brans-Dicke (BD) theory have been done by Singh and Rai (1983).

It is generally accepted that BD scalar-tensor theory plays an important role in the present view of the very early universe. More recently the interest of this kind of theory was renewed, owing to its association with superstring theories, extra-dimensional theories and models with inflation or accelerated expansion. The simplest inflationary models (Domini et al. 1983; Mathiazhagen and Johri 1984), extended inflation (La and Steinhardt 1989) and hyper extended inflation and extended chaotic inflation (Linde 1990; Steinhardt and Accetta 1990) are based on BD theory and other general scalar-tensor theories. Uehara and Kim (1982) have studied BD theory with cosmological constant Λ and presented exact solutions for spatially flat Friedmann-Robertson-Walker

C.P. Singh (✉)
Department of Applied Mathematics,
Delhi Technological University
(Formerly Delhi College of Engineering), Bawana Road,
Delhi 110 042, India
e-mail: cpsphd@rediffmail.com

(FRW) model in matter-dominated universe. Johri and Sudharsan (1989), and Banerjee and Beesham (1996) have considered BD cosmology with a causal viscous fluid in full theory of non-equilibrium thermodynamics. They have found exact solutions for a spatially flat FRW model by making the assumption of scalar field ϕ with some power of scale factor of the FRW model. Chakraborty and Shah (1995) have studied FRW models in BD theory whereas Singh et al. (1997) have discussed FRW models with causal viscous fluid in BD theory. Reddy and Rao (1981, 2006), Banerjee and Santos (1982), Singh et al. (1983), Reddy (2003), Reddy et al. (2007), Rao et al. (2009), Rathore and Mandawat (2009), and Singh and Sharma (2010) have investigated several aspects of the cosmological models in BD theory in different physical context. Berman (2008) has discussed the shear and vorticity in an accelerating BD lambda-universe with torsion. El-Nabulsi (2010a, 2010b, 2011) have investigated the Gauss-Bonnet corrections in modified BD theory and discussed their findings in detail.

The problem of particle creation in the universe has recently attracted a lot of interest in cosmology. Prigogine et al. (1988, 1989) have investigated the role of irreversible processes in creation of matter out of gravitational energy in the context of general relativity. It was shown that thermodynamics of open systems, when applied to cosmology, leads to a reinterpretation in Einstein's equations of the matter energy stress tensor. The universe starts from random vacuum fluctuation and the cosmic expansion is driven by the creation of matter particles. In other words, the process of particle creation out of gravitational energy is basically an irreversible phenomenon, capable of explaining the entropy burst in the expanding universe. A detailed study of the thermodynamics of the particle creation with changing specific entropy have been discussed by Calvão et al. (1992), Lima and Germano (1992), Lima et al. (1991, 1996), Zimdahl et al. (1996). Johri and Desikan (1996) have studied Friedmann-Robertson-Walker (FRW) models with particle creation.

After the discovery of the accelerating universe the particle creation was reconsidered to explain it and got unexpected results. The particle creation pressure, which is negative, might play the role of dark energy component. Lima and Alcaniz (1999), and Alcaniz and Lima (1999) have discussed FRW models with matter creation and analyzed the results through the observations. It was shown that the models with particle creation are consistent with the observational data.

Sudarshan and Johri (1994), Zimdahl and Pavón (1994), and Triginer and Pavón (1994) have discussed the effect of bulk viscosity on the cosmological evolution of open thermodynamic systems which allow for simultaneous particle creation and entropy production. Their investigations reveal that the production of specific entropy is independent of the

nature of the creation rate and depends only upon the coefficient of the bulk viscosity. This suggests that the bulk viscosity and particle creation are not only independent processes, but in general they lead to different histories of cosmic evolution.

Maniharsingh (1987, 1991) has obtained the dynamics of the particle creation in the slowly rotating FRW universe, using BD theory. Johri and Desikan (1994) have studied cosmological models with constant deceleration parameter in BD theory in the presence of particle creation. Ibochouba and Ali (1996) have investigated the dynamics of the particle creation in relativistic viscous fluid FRW models in BD theory. Desikan (1997), Johri and Pandey (1999), Singh and Beesham (1999), Singh et al. (2002) and Singh and Kale (2011) have studied the role of particle creation and bulk viscosity in isotropic and anisotropic models. Zimdahl et al. (2001) have tested the particle creation with SNe Ia data and got the result of the accelerating universe. Yuan et al. (2007) has studied the models with adiabatic particle creation and showed that the model is consistent with SNe Ia data. Liu and Liu (2011) have analyzed the reconstruction of dark energy and equilibrium thermodynamics in BD theory.

In the standard model, the history of the universe begins with the radiation phase and then evolves to the present matter-dominated era. In order to overcome some of the difficulties met by standard model, Guth (1981) proposed an inflationary phase and this would happen prior to the radiation-dominated phase. In general, the field equations are solved separately for the different epochs. However, Some authors have tried to solve the field equations in a unified manner. Madsen and Ellis (1988) presented the evolution of the universe for inflationary, radiation and matter-dominated phases in a unified manner by assuming (γ) of "gamma-law" equation of state $p = (\gamma - 1)\rho$ as a function of scale factor of the FRW metric. Later on, Israelit and Rosen (1989, 1993) used a different equation of state to describe the transition from pre-matter to radiation and then radiation to matter-dominated phase in a unified manner.

In a similar way, Carvalho (1996) has studied flat Friedmann-Robertson-Walker (FRW) model in general relativity by using the "gamma-law" equation of state $p = (\gamma - 1)\rho$, where γ varies with the cosmic time to describe the early phases (inflation and radiation) of the evolution of the universe in a unified manner. Therefore, it is not realistic to assume γ as a constant throughout the history of the universe. We can obtain a reasonably realistic model if we assume the universe evolves through the epochs each of which γ is constant. Ram and Singh (1999, 1997) have studied flat FRW model with variable equation of state parameter in BD theory. Recently, Singh and Beesham (2011) have studied the early universe cosmology with particle creation and discussed the kinematics tests of the findings.

In the present paper we study the role of irreversible processes, corresponding to the creation of matter out of gravitational energy in Brans-Dicke theory. Prigogine's hypothesis (1988, 1989) of creation of matter has been analyzed in Brans-Dicke theory. To accommodate the creation of new particles, the universe is regarded as an open thermodynamical system and the energy conservation equation is modified to incorporate the creation pressure term. It is supposed that Brans-Dicke scalar field is a function of scale factor. Exact solutions of the field equations are obtained using "gamma-law" equation of state in which the equation of state parameter depends on scale factor of the universe. A unified description of the early evolution of the universe has been presented in which an inflationary phase is followed by an radiation-dominated phase. We find that the expansion of the universe is driven by the particle creation in each phase. The physical and geometrical properties of the physical parameters have been discussed in detail.

2 Thermodynamics of particle creation

In the standard model, the universe is considered as a 'closed' system and the corresponding laws of thermodynamics have the form

$$d(\rho V) = dQ - pdV, \quad (1)$$

and

$$TdS = d(\rho V) + pdV, \quad (2)$$

where ρ is the energy density, p the thermodynamic pressure, V the volume containing N particles, Q is the heat during the cosmic time t , T the temperature and S is the entropy of the system.

From (1) and (2), we see that the entropy production is given by

$$TdS = dQ. \quad (3)$$

Consequently, for a closed adiabatic system ($dQ = 0$), the entropy remains constant. If one treats, following Prigogine et al. (1988, 1989) that, the expansion is described by an 'open' thermodynamic system, allowing for irreversible particle creation from the energy of gravitational field, one can account for entropy production right from the beginning and the second law of thermodynamics is also incorporated into the evolutionary equations in a more meaningful manner. In this case the number of particles N in a given volume V is not to be a constant.

Thus allowing for particle creation, the modification of (1), into account of variation of particle number, leads to

$$d(\rho V) = dQ - pdV + \frac{h}{N}dN, \quad (4)$$

where $h = (\rho + p)V$ is the total enthalpy of the system. For open system, adiabatic transformations ($dQ = 0$) reduce (4) to

$$d(\rho V) + pdV - \frac{h}{N}dN = 0. \quad (5)$$

Equation (5) can be rewritten as

$$d(\rho V) + (p + p_c)dV = 0, \quad (6)$$

where

$$p_c = -\frac{(\rho + p)V}{N} \frac{dN}{dV}. \quad (7)$$

Thus, the creation of particle corresponds to a supplementary pressure p_c . It is noted that (6) is equivalent to the conservation equation with additional pressure due to the particle creation and therefore this supplementary pressure must be considered as a part of the cosmological pressure entering into the Einstein field equations. p_c is negative or zero depending on the presence or absence of particle creation. In such a transformation the thermal energy received by the system is entirely due to the change of the number of particles. This change is due to the transfer of energy from the gravitational field of matter. Hence, the creation of particle acts as a source of internal energy.

Now, the entropy change dS , given in (2) in an 'open' system becomes

$$TdS = d(\rho V) + pdV - \mu dN, \quad (8)$$

where $\mu = \frac{h - TS}{N} \geq 0$ is the chemical potential associated to the non conservation of the particle number. Therefore, from (5) and (8), we get

$$\frac{dS}{S} = \frac{dN}{N}. \quad (9)$$

The second law of thermodynamics requires that $dS \geq 0$. We regard the second law of thermodynamics as one of the most fundamental laws of physics and it should hold whether creation of particle takes place or not. Therefore, from (9), we must have

$$dN \geq 0. \quad (10)$$

This inequality implies that the space-time can produce particle.

3 Field equations of BD theory

The field equations of Brans-Dicke theory in the unit $c = 1$ are given by

$$\begin{aligned}
 G_{ij} &= R_{ij} - \frac{1}{2}g_{ij}R \\
 &= -\frac{8\pi}{\phi}T_{ij} - \frac{\omega}{\phi^2}\left[\phi_{;i}\phi_{;j} - \frac{1}{2}g_{ij}\phi_{;k}\phi^{;k}\right] \\
 &\quad - \frac{1}{\phi}\left[\phi_{;ij} - g_{ij}\square\phi\right],
 \end{aligned} \quad (11)$$

and

$$\square\phi = \frac{8\pi}{(2\omega+3)}T_i^i, \quad (12)$$

where ϕ is the BD scalar, ω the BD coupling parameter, T_{ij} is the energy momentum tensor for perfect fluid and particle creation, which takes the form

$$T_{ij} = (\rho + p + p_c)u_i u_j - (p + p_c)g_{ij} \quad (13)$$

where p_c is the particle creation pressure given by (7) and u_i is four velocity satisfying the condition $u_i u^i = 1$.

Considering that our universe is homogeneous and isotropic, we work with the flat Friedmann-Robertson-Walker (FRW) space-time (Weinberg 1972)

$$ds^2 = dt^2 - R^2(t)\left[dr^2 + r^2(d\theta^2 + \sin^2\theta d\phi^2)\right], \quad (14)$$

where r , θ , and ϕ are dimensionless co-moving coordinates and $R(t)$ is the scale factor.

In this space-time, the Friedmann and BD scalar equations (11) and (12) take the form (see Ibochouba and Ali 1996; Tarachand and Ratnaprabha 1989; Obregon and Pimentel 1978; Montenegro and Carneiro 2007; Lee et al. 2011)

$$3H^2 = \frac{8\pi\rho}{\phi} - 3H\left(\frac{\dot{\phi}}{\phi}\right) + \frac{\omega}{2}\frac{\dot{\phi}^2}{\phi^2}, \quad (15)$$

$$\frac{\ddot{\phi}}{\phi} + 3H\frac{\dot{\phi}}{\phi} = \frac{8\pi}{(3+2\omega)\phi}[\rho - 3(p + p_c)], \quad (16)$$

where $H = \dot{R}/R$ is the Hubble parameter and an overdot denotes the derivative with respect to time t . Here we note that the case of $\omega = -3/2$ is not allowed. The energy conservation equation $T_{;j}^{ij} = 0$ leads to

$$\dot{\rho} + 3(\rho + p)H = -3p_c H. \quad (17)$$

In models with adiabatic creation, the balance equation for the particle number density n (Lima and Germano 1992; Desikan 1997) is given by

$$\frac{\dot{n}}{n} + 3H = \frac{\psi(t)}{n} = \frac{\dot{N}}{N} \quad (18)$$

where $n = \frac{N}{V}$ is the particle number density and $\psi(t)$ is the matter creation rate ($\psi > 0$ corresponds to particle creation

while $\psi < 0$ to particle decay). From (7) we see that the creation pressure p_c depends on the particle creation rate. We need to know the exact form of the function ψ the one which is determined from a more fundamental theory than involves quantum processes.

4 Solution of the field equations

We have five unknowns, namely, R, ϕ, p, ρ and p_c and three independent equations (15), (16) and (17). So, we have a freedom to choose two assumptions only. But it is very difficult to obtain the general exact solutions due to highly non-linearity of the field equations and we would try to obtain leaving (15) and we will use it get the relation between constants. Therefore, we have one more freedom to choose the assumption to solve the system of equations.

We take the simple phenomenological expression of the particle creation rate (Lima et al. 1996)

$$\psi(t) = 3\beta n H, \quad (19)$$

where the parameter β is a dimensionless constant, defined on the interval $[0, 1]$. The most interesting situations emerge during phase in which $\beta \approx 1$, i.e., of order of unity.

Further, We assume the following relation between the scale factor $R(t)$ and the BD scalar field ϕ (Johri and Sudharsan 1989; Banerjee and Beesham 1996):

$$\phi = \phi_0 R^\alpha \quad (20)$$

where ϕ_0 and α are constants. With (20), (15) becomes

$$\left(3 + 3\alpha - \frac{\omega}{2}\alpha^2\right)H^2 = \frac{8\pi\rho}{\phi_0 R^\alpha}, \quad (21)$$

which can be rewritten as

$$2\frac{H'}{H} = \frac{\rho'}{\rho} - \frac{\alpha}{R}, \quad (22)$$

where a prime denoted derivative with respect to scale factor R .

We suppose that the pressure p and energy density ρ are related through the “gamma-law” equation of state

$$p = (\gamma - 1)\rho. \quad (23)$$

In general, the value of γ is taken to be constant and lying in the interval $0 \leq \gamma \leq 2$. But our aim in this paper is to let the parameter γ depends on scale factor R to describe the early phases, inflationary and radiation-dominated evolution of the universe in a unified manner. We assume, following Carvalho (1996) that, the functional form of γ as

$$\gamma(R) = \frac{4}{3} \frac{A(R/R_*)^2 + (a/2)(R/R_*)^a}{A(R/R_*)^2 + (R/R_*)^a}, \quad (24)$$

where A is a constant and ‘ a ’ is free parameter related to the power of the cosmic time t during the inflationary phase. Here, R_* is a certain reference value of R . The function $\gamma(R)$ is defined in such a manner that when the scale factor R is less than R_* , i.e., when $R \ll R_*$, an inflationary phase ($\gamma \leq 2a/3$) can be obtained and for $R \gg R_*$ we have a radiation-dominated phase ($\gamma = 4/3$). The expression of $\gamma(R)$ in (24) is an increasing function of R . In the limit $R \rightarrow 0$, $\gamma(R) = \frac{2a}{3}$. Thus, 1 is the maximum value of ‘ a ’ for an inflation epoch to exist. As ‘ a ’ approaches to zero we have an exponential inflation ($\gamma = 0$). Therefore, a must lie in the interval $0 \leq a < 1$.

Using (7) and (23) into (17), we get

$$\dot{\rho} + 3(1 - \beta)\gamma\rho H = 0, \quad (25)$$

which can be written as

$$\frac{\rho'}{\rho} + 3(1 - \beta)\frac{\gamma(R)}{R} = 0. \quad (26)$$

From (22) and (26), we finally get

$$H' + \left[\frac{3}{2}(1 - \beta)\gamma(R) + \frac{\alpha}{2} \right] \frac{H}{R} = 0. \quad (27)$$

Substituting (24) into (27) and solving, we get

$$H = \frac{C}{R^{\alpha/2} [A(R/R_*)^2 + (R/R_*)^a]^{(1-\beta)}}, \quad (28)$$

where C is a constant of integration. If $H = H_*$ for $R = R_*$, we have a relation between constants A and C as

$$C = H_* R_*^{\alpha/2} (1 + A)^{(1-\beta)}. \quad (29)$$

An important observational quantity is the deceleration parameter $q = -\frac{R\ddot{R}}{\dot{R}^2}$. A unified expression of q for both inflationary and radiation-dominated phases can be expressed as a function of scale factor R as

$$q = \frac{(1 - 2\beta + \frac{\alpha}{2})A(R/R_*)^2 + (\frac{\alpha}{2} + a(1 - \beta) - 1)(R/R_*)^a}{A(R/R_*)^2 + (R/R_*)^a}. \quad (30)$$

Integrating (28) for $H = \dot{R}/R$, an expression for t in terms of the scale factor R , in case of ($a \neq 0$), is given by

$$Ct = \int R^{\frac{\alpha}{2}-1} [A(R/R_*)^2 + (R/R_*)^a]^{(1-\beta)} dR. \quad (31)$$

In the following subsections, we solve (31) for two early phases of the evolution of the universe according as $R \ll R_*$ or $R \gg R_*$.

4.1 Inflationary phase

For inflationary phase ($R \ll R_*$), the second term of the integral in (31) on right hand side dominates which gives the power-law solution of the scale factor ($a \neq 0$) as

$$R^{[a(1-\beta)+\frac{\alpha}{2}]} = R_*^{a(1-\beta)} \left[\left\{ a(1 - \beta) + \frac{\alpha}{2} \right\} Ct \right]. \quad (32)$$

The above equation shows that the dimension of the universe increases according to power-law inflation $R \propto t^{\frac{2}{2a(1-\beta)+\alpha}}$, where $0 \leq \beta < 1$. We see that the condition for expansion of the universe is $[2a(1 - \beta) + \alpha] > 0$. For $\beta = 0$ and $\alpha = 0$, the above (32) reduces to the standard FRW model (Carvalho 1996), i.e., $R \propto t^{1/a}$.

The Hubble parameter in terms of t is given by

$$H = \frac{2}{[2a(1 - \beta) + \alpha]} \frac{1}{t}. \quad (33)$$

The BD scalar is given by

$$\phi = \phi_0 \left[R_*^{a(1-\beta)} \left[\left\{ a(1 - \beta) + \frac{\alpha}{2} \right\} Ct \right] \right]^{\frac{2\alpha}{[2a(1-\beta)+\alpha]}}. \quad (34)$$

The energy density and particle creation pressure are obtained as

$$\rho = \rho_0 \left(3 + 3\alpha - \frac{\omega}{2}\alpha^2 \right) t^{\frac{2\alpha}{[2a(1-\beta)+\alpha]}-2}, \quad (35)$$

$$p_c = -\frac{2a}{3}\beta\rho_0 \left(3 + 3\alpha - \frac{\omega}{2}\alpha^2 \right) t^{\frac{2\alpha}{[2a(1-\beta)+\alpha]}-2}, \quad (36)$$

where

$$\rho_0 = \frac{\phi_0 [R_*^{a(1-\beta)} \{ [a(1 - \beta) + \frac{\alpha}{2}] C \}]^{\frac{2\alpha}{[2a(1-\beta)+\alpha]}}}{8\pi [a(1 - \beta) + \frac{\alpha}{2}]^2}.$$

For energy density to be positive, we must have $(6 + 6\alpha - \omega\alpha^2) > 0$. The particle number density is given by

$$n = n_{0i} \left(\frac{R}{R_*} \right)^{-3(1-\beta)}. \quad (37)$$

We note from (37) that the effect of particle creation is measured by the parameter β . The particle density $N = nR^3$ is given by

$$N = N_{0i} \left(\frac{R}{R_*} \right)^{3\beta}. \quad (38)$$

In the above expressions the subscript ‘ $0i$ ’ refers to the present observed values of the parameters during inflationary phase. It follows from (38) that N increases as some power of R . The BD scalar function ϕ increases with time. The energy density and particle creation are decreasing

functions of t for $a(1 - \beta) > 0$. As $t \rightarrow 0$, $\rho \rightarrow \infty$, thus the model has singularity at $t = 0$.

Let us consider the entropy behavior during the inflationary phase. From (9) and (38), one may write the entropy as

$$S = S_{0i} \left(\frac{R}{R_*} \right)^{3\beta}. \quad (39)$$

The entropy increases with the increase of the rate of creation of particle. For $\beta = 0$, i.e., if there is no creation of particle, we get $n = n_{0i} (R/R_*)^{-3}$, N and S would remain constant throughout the evolution of the universe and we would recover the standard FRW model of the universe. This is the case of an ideal gas and source term $\psi(t)$ and hence the creation pressure p_c vanish. We find that particle number density is decreasing function of time. If $\beta = 1$, the particle number density is uniform during the evolution of the universe which leads to the result that the particle production source term is determined by the expansion rate $\psi(t) = 3nH$.

Now, inserting the values of R , ρ , ϕ and p_c into (16) we obtain a relation between constants

$$\begin{aligned} & [(3 + 2\omega) + \{4 - 2a(1 - \beta)\}\omega]\alpha^2 \\ & + [(3 + 2\omega)\{6 - 2a(1 - \beta)\} - 6\{4 - 2a(1 - \beta)\}]\alpha \\ & - \{24 - 12a(1 - \beta)\} = 0, \end{aligned} \quad (40)$$

which is quadratic in α and gives the physically viable models for this constraints. It is readily seen from (30) that the deceleration parameter q in inflationary phase is given by

$$q = \left[a(1 - \beta) + \frac{\alpha}{2} - 1 \right], \quad (41)$$

which is constant and gives positive value for $[2a(1 - \beta) + \alpha] > 2$ and negative or zero for $[2a(1 - \beta) + \alpha] \leq 2$.

Figure 1 plots scale factor $R(t)$ versus cosmic time t for various values of constants. It is observed that the expansion of the universe inflates more rapidly due to particle creation (marginal thick line, i.e., $\alpha = 0$ and $\beta = 0.5$). The universe

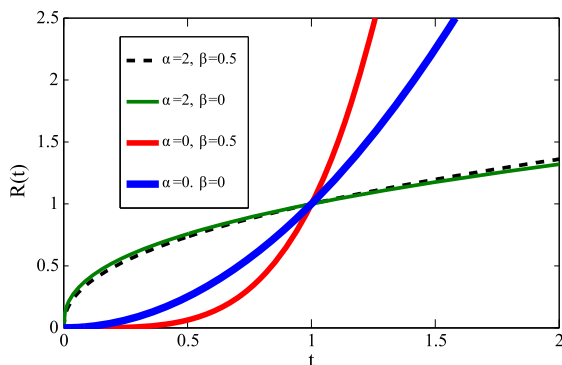


Fig. 1 $R(t)$ vs. t with $a = 0.5$

expands with more decelerated rate due to BD scalar field factor as shown by thin line ($\alpha = 2$ and $\beta = 0$). When both α and β are non-zero, the universe expands with decelerated rate as shown by dotted line but with slight change with $\beta = 0$ and $\alpha \neq 0$. The very thick line show the expansion of the universe when both $\alpha = 0$ and $\beta = 0$, i.e., the FRW model with perfect fluid only. One may say that the inflation of the universe is due to the particle creation. The BD scalar field factor decelerates the expansion of the universe.

4.2 Radiation-dominated phase

For radiation-dominated phase ($R \gg R_*$), the first term of the integrand in (31) on right hand side dominates over first term, which gives the power-law solution of the scale factor as

$$R^{[2(1-\beta) + \frac{\alpha}{2}]} = R_*^{2(1-\beta)} \left[\left\{ 2(1 - \beta) + \frac{\alpha}{2} \right\} C t \right]. \quad (42)$$

The above equation shows that the dimension of the universe increases according to power-law $R \propto t^{\frac{2}{4(1-\beta)+\alpha}}$, where $0 \leq \beta < 1$. For $\beta = 0$ and $\alpha = 0$, the above equation (42) reduces to the standard FRW model (Carvalho 1996), i.e., $R \propto t^{1/2}$.

The Hubble parameter in terms of t is given by

$$H = \frac{2}{[4(1 - \beta) + \alpha] t}. \quad (43)$$

The BD scalar is given by

$$\phi = \phi_0 \left[R_*^{2(1-\beta)} \left[\left\{ 2(1 - \beta) + \frac{\alpha}{2} \right\} C t \right] \right]^{\frac{2\alpha}{[4(1-\beta)+\alpha]}}. \quad (44)$$

It is straight forward to obtain the energy density, creation pressure, particle number density, particle number and entropy production as functions of the scale factor R and of the β parameter. These quantities are, respectively, given by

$$\rho = \rho_1 \left(3 + 3\alpha - \frac{\omega}{2}\alpha^2 \right) t^{\frac{2\alpha}{[4(1-\beta)+\alpha]} - 2}, \quad (45)$$

$$p_c = -\frac{4}{3}\beta\rho_1 \left(3 + 3\alpha - \frac{\omega}{2}\alpha^2 \right) t^{\frac{2\alpha}{[4(1-\beta)+\alpha]} - 2}, \quad (46)$$

$$n = n_{0r} \left(\frac{R}{R_*} \right)^{-3(1-\beta)}, \quad (47)$$

$$N = N_{0r} \left(\frac{R}{R_*} \right)^{3\beta}, \quad (48)$$

$$S = S_{0r} \left(\frac{R}{R_*} \right)^{3\beta}, \quad (49)$$

where

$$\rho_1 = \frac{\phi_0 [R_*^{2(1-\beta)} \{ [2(1 - \beta) + \frac{\alpha}{2}] C \}]^{\frac{2\alpha}{[4(1-\beta)+\alpha]}}}{8\pi [2(1 - \beta) + \frac{\alpha}{2}]^2}$$

and n_{0r} , N_{0r} and S_{0r} are constant of integrations.

Inserting the above solutions in to (16), a relation between the constants can be written as

$$[(3 + 2\omega) + 4\beta\omega]\alpha^2 + [2(3 + 2\omega)(1 + 2\beta) - 24\beta]\alpha - 24\beta = 0. \quad (50)$$

which is quadratic in α and gives the physically viable models for this constraints. From (30) the deceleration parameter q in this phase is given by

$$q = \left[(1 - 2\beta) + \frac{\alpha}{2} \right], \quad (51)$$

which is constant and gives positive for $(2 - 4\beta + \alpha) > 0$ and negative or zero for $(2 - 4\beta + \alpha) \leq 0$. The energy density is decreasing function of t for $0 < \beta < 1$. As $t \rightarrow 0$, $\rho \rightarrow \infty$, thus the model has singularity at $t = 0$. Equations (35) and (45) show that the densities in inflation and radiation, respectively, vary as $\rho \propto t^{\frac{2\alpha}{2\alpha(1-\beta)+\alpha}-2}$ and $\rho \propto t^{\frac{2\alpha}{4(1-\beta)+\alpha}-2}$. Hence, in a model with inflation and radiation, the transition from inflation to a radiation-dominated phase, in course of expansion, happens exactly as in the standard model. We also observe that the same expressions describe the evolution of the particle number density, number of particle and entropy production either for inflationary phase or radiation-dominated phase. The BD scalar has no effect on these thermodynamical quantities, these depend on the particle creation only.

In Fig. 2 a straight line shows the expansion of the universe due to particle creation ($\alpha = 0$ and $\beta = 0.5$). The BD scalar field increases the rate of expansion of the universe at early stages of the evolution. However, the universe expands with more decelerated rate after certain times of evolution. We see that $\alpha = 2$ and $\beta = 0.5$ make the expansion of the universe with less decelerated rate. Therefore, in this phase the expansion of the universe is also driven by the particle creation.

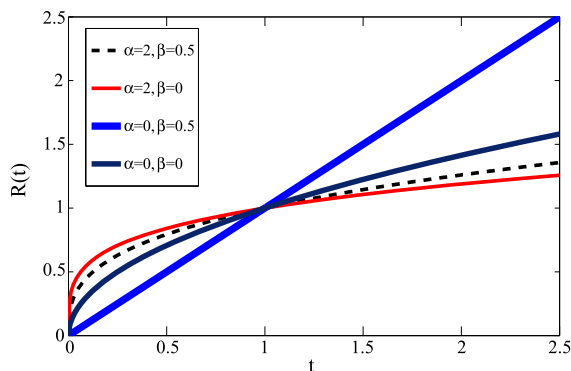


Fig. 2 $R(t)$ vs. t

5 Particular case

We now study the solution in the limit $a \rightarrow 0$ in inflationary and radiation-dominated phases.

In this case, (28) becomes

$$H = \frac{C}{R^{\alpha/2}[A(R/R_*)^2 + 1]^{(1-\beta)}}. \quad (52)$$

A unified expression for deceleration parameter in terms of scale factor has the form

$$q = \frac{(1 - 2\beta + \frac{\alpha}{2})A(R/R_*)^2 - (1 - \frac{\alpha}{2})}{A(R/R_*)^2 + 1}. \quad (53)$$

Again, in the limit of very small R ($R \ll R_*$), we get

$$R = \left(\frac{\alpha C}{2} t \right)^{\frac{2}{\alpha}}, \quad (54)$$

which is the power-law expansion for $\alpha > 0$. The expansion is due to BD scalar field only. The Hubble parameter is given by

$$H = \frac{2}{\alpha t} \quad (\alpha \neq 0). \quad (55)$$

The BD scalar field is obtained as

$$\phi = \phi_0 \left(\frac{\alpha C}{2} t \right)^2. \quad (56)$$

The scalar field increases as the square of the cosmic time t . The particle creation pressure p_c is zero where as the energy density is given by

$$\rho = \frac{(3 + 3\alpha - \frac{\omega}{2}\alpha^2)\phi_0 C^2}{8\pi}, \quad (57)$$

which shows that the energy density is constant through out the evolution of the universe. The particle number density, Number particle and entropy are respectively given by

$$n = n_1 (\alpha C t)^{-\frac{6(1-\beta)}{\alpha}}, \quad (58)$$

$$N = N_1 t^{\frac{6\beta}{\alpha}}, \quad (59)$$

$$S = S_1 t^{\frac{6\beta}{\alpha}}. \quad (60)$$

Hence, particle number density decreases whereas the number of particles and entropy increase in this phase. Here n_1 , N_1 and S_1 are arbitrary constants. For $\beta = 0$, we have $n \propto t^{-6/\alpha}$, and N and S are constants. Equation (16) gives

$$(1 + 2\omega)\alpha^2 - 2(3 - 2\omega)\alpha - 8 = 0, \quad (61)$$

which is quadratic in α and gives a relation between the constants.

In the limit of very large R ($R \gg R_*$), when the universe enters to radiation-dominated phase, we obtain

$$R^{[2(1-\beta)+\frac{\alpha}{2}]} = R_*^{2(1-\beta)} \left[\left\{ 2(1-\beta) + \frac{\alpha}{2} \right\} C t \right]. \quad (62)$$

The other results for various parameters are the same as obtained in Sect. 4.2. We see from (53) that the deceleration parameter varies from $q = -(1 - \frac{\alpha}{2})$ at $R = 0$ to $q = (1 - 2\beta + \frac{\alpha}{2})$ for radiation-dominated phase.

6 Conclusion

We have investigated zero curvature FRW model with particle creation in Brans-Bicke cosmology with “gamma-law” equation of state. We have assumed that the adiabatic parameter ‘ γ ’ varies continuously as a function of the scale factor to describe the early phases of the evolution of the universe in a unified manner. A class of models is obtained according to the value of the parameter ‘ a ’ which lies in the interval $0 \leq a < 1$. For ‘ a ’ in the interval $0 < a < 1$, γ slowly increases from $2a/3$ for $R \ll R_*$ to $4/3$ when $R \gg R_*$. The first period of evolution is describe as a power-law inflation with the scale factor varying according $R \propto t^{2/[2a(1-\beta)+\alpha]}$. This is then followed by a radiation era where scale factor is varying according $R \propto t^{2/[4(1-\beta)+\alpha]}$. Considering the energy conservation and particle creation rate we have obtained the solutions in early phases of the evolution of the universe. The role played by BD scalar field and particle creation in the expansion of the universe is investigated. The variation of scale factor with cosmic time have been shown in Figs. 1 and 2 during inflationary and radiation-dominated phases. We find that the acceleration is driven by particle creation where as the BD scalar decelerates the expansion of the universe at late times. For $a = 0$, the scale factor varies as $R \propto t^{2/\alpha}$. We have found that the Brans-Dicke scalar tensor theory modifies the solution for $a = 0$ as obtained by Carvalho (1996). The energy density is constant during the evolution of the universe. The possibility that $q < 0$ has come in this case with $\alpha < 2$, which indicates that the universe may accelerate. The particle number density decreases with time where as the particle number and entropy increase with time. We see that a unified description of the early evolution of the universe is possible with varying adiabatic parameter with irreversible open thermodynamics system in Brans-Dicke theory.

Acknowledgements It is my pleasure to thank referee for many valuable suggestions. Many thanks are due also to Prof. Shri Ram, my mentor and Prof. V.B. Johri whose works on the particle creation stimulate to take the interest in this work.

References

- Alcaniz, J.S., Lima, J.A.S.: *Astron. Astrophys.* **349**, 72 (1999)
- Banerjee, A., Santos, N.O.: *Nuovo Cimento B* **67**, 31 (1982)
- Banerjee, N., Beesham, A.: *Aust. J. Phys.* **49**, 899 (1996)
- Berman, M.S.: *Astrophys. Space Sci.* **317**, 279 (2008)
- Brans, C., Dicke, R.H.: *Phys. Rev.* **124**, 925 (1961)
- Calvão, M.O., Lima, J.A.S., Waga, I.: *Phys. Lett. A* **162**, 233 (1992)
- Carvalho, J.C.: *Int. J. Theor. Phys.* **35**, 2019 (1996)
- Chakraborty, S., Shah, M.F.: *Astrophys. Space Sci.* **226**, 73 (1995)
- Desikan, K.: *Gen. Relativ. Gravit.* **29**, 435 (1997)
- Dirac, P.A.M.: *Nature* **132**, 323 (1937)
- Dirac, P.A.M.: *Proc. R. Soc. Lond. Ser. A* **165**, 199 (1938)
- Dominici, D., Holman, R., Kim, C.W.: *Phys. Rev. D* **25**, 2983 (1983)
- El-Nabulsi, A.R.: *Astrophys. Space Sci.* **331**, 199 (2011)
- El-Nabulsi, A.R.: *Astrophys. Space Sci.* **327**, 111 (2010a)
- El-Nabulsi, A.R.: *Astrophys. Space Sci.* **327**, 167 (2010b)
- Guth, A.H.: *Phys. Rev. D* **23**, 347 (1981)
- Ibochouba, L., Ali, M.A.: *Astrophys. Space Sci.* **241**, 227 (1996)
- Israelit, M., Rosen, N.: *Astrophys. J.* **342**, 627 (1989)
- Israelit, M., Rosen, N.: *Astrophys. Space Sci.* **204**, 317 (1993)
- Johri, V.B., Sudharsan, R.: *Aust. J. Phys.* **42**, 215 (1989)
- Johri, V.B., Desikan, K.: *Gen. Relativ. Gravit.* **26**, 1217 (1994)
- Johri, V.B., Pandey, S.K.: *Int. J. Theor. Phys.* **38**, 1981 (1999)
- Johri, V.B., Desikan, K.: *Astrophys. Lett. Commun.* **33**, 287 (1996)
- La, D., Steinhardt, P.J.: *Phys. Rev. Lett.* **62**, 376 (1989)
- Lee, H.W., Kim, K.Y., Myung, Y.S.: *Eur. Phys. J. C* **71**, 1585 (2011)
- Lima, J.A.S., Calvão, M.O., Waga, I.: *Cosmology, Thermodynamics and Matter Creation*, vol. 317. World Scientific, Singapore (1991)
- Lima, J.A.S., Germano, A.S.: *Phys. Lett. A* **170**, 373 (1992)
- Lima, J.A.S., Germano, A.S., Abramo, L.R.W.: *Phys. Rev. D* **53**, 4287 (1996)
- Lima, J.A.S., Alcaniz, J.S.: *Astron. Astrophys.* **348**, 1 (1999)
- Linde, A.: *Phys. Lett. B* **238**, 160 (1990)
- Liu, X.-M., Liu, W.-B.: *Astrophys. Space Sci.* **334**, 203 (2011)
- Madsen, M.S., Ellis, G.F.R.: *Mon. Not. R. Astron. Soc.* **234**, 67 (1988)
- Maniharsingh, K.: *Astrophys. Space Sci.* **139**, 183 (1987)
- Maniharsingh, K.: *Astrophys. Space Sci.* **182**, 141 (1991)
- Mathiazhagen, C., Johri, V.B.: *Class. Quantum Gravity* **1**, L29 (1984)
- Montenegro, A.E., Carneiro, S.: *Class. Quantum Gravity* **24**, 313 (2007)
- Obregon, O.J., Pimentel, L.O.: *Gen. Relativ. Gravit.* **9**, 585 (1978)
- Prigogine, I., Geheniau, J., Gunzig, E., Nardone, P.: *Proc. Natl. Acad. Sci.* **85**, 7428 (1988)
- Prigogine, I., Geheniau, J., Gunzig, E., Nardone, P.: *Gen. Relativ. Gravit.* **21**, 767 (1989)
- Rao, V.U.M., Vinutha, T., Sireesha, K.V.S.: *Astrophys. Space Sci.* **323**, 401 (2009)
- Ram, S., Singh, C.P.: *Nuovo Cimento B* **114**, 245 (1999)
- Ram, S., Singh, C.P.: *Astrophys. Space Sci.* **254**, 143 (1997)
- Rathore, G.S., Mandawat, K.: *Astrophys. Space Sci.* **321**, 37 (2009)
- Reddy, D.R.K.: *Astrophys. Space Sci.* **281**, 365 (2003)
- Reddy, D.R.K., Rao, M.V.S.: *Astrophys. Space Sci.* **305**, 183 (2006)
- Reddy, D.R.K., Naidu, R.L., Rao, V.U.M.: *Int. J. Theor. Phys.* **46**, 1443 (2007)
- Reddy, D.R.K., Rao, V.U.M.: *J. Phys. Math. A* **14**, 1973 (1981)
- Singh, T., Rai, L.N.: *Gen. Relativ. Gravit.* **15**, 875 (1983)
- Singh, G.P., Beesham, A.: *Aust. J. Phys.* **52**, 1039 (1999)
- Singh, G.P., Deshpande, R.V., Singh, T.: *Astrophys. Space Sci.* **282**, 489 (2002)
- Singh, G.P., Ghosh, S.G., Beesham, A.: *Aust. J. Phys.* **50**, 1 (1997)
- Singh, G.P., Kale, A.Y.: *Astrophys. Space Sci.* **331**, 207 (2011)
- Singh, J.K., Sharma, N.K.: *Astrophys. Space Sci.* **327**, 293 (2010)
- Singh, C.P., Beesham, A.: *Astrophys. Space Sci.* **336**, 469 (2011)
- Singh, T., Rai, L.N., Singh, T.: *Astrophys. Space Sci.* **96**, 95 (1983)
- Steinhardt, P.J., Accetta, F.S.: *Phys. Rev. Lett.* **64**, 2740 (1990)

- Sudarshan, R., Johri, V.B.: Gen. Relativ. Gravit. **26**, 41 (1994)
 Triginer, J., Pavón, D.: Gen. Relativ. Gravit. **26**, 513 (1994)
 Tarachand, R., Ratnaprabha, A.: Astrophys. Space Sci. **155**, 233 (1989)
 Uehara, K., Kim, C.W.: Phys. Rev. D **28**, 2575 (1982)
 Weinberg, S.: Gravitation and Cosmology. Wiley, New York (1972)
 Will, C.: Theory and Experimental in Gravitational Physics. Cambridge University Press, Cambridge (1981)
 Yuan, Q., Tong, J., Ze-Long, Y.: Astrophys. Space Sci. **311**, 407 (2007)
 Zimdahl, W., Triginer, J., Pavón, D.: Phys. Rev. D **54**, 6101 (1996)
 Zimdahl, W., et al.: Phys. Rev. D **64**, 063501 (2001)
 Zimdahl, W., Pavón, D.: Mon. Not. R. Astron. Soc. **266**, 872 (1994)

Fuzzy Approach to Nodal Reliability Ranking for Radial Distribution Systems

¹Roma Raina and ²Mini Thomas

¹Member, IEEE & IASTED, romaraina@yahoo.com,

²Senior member, IEEE, , mini@ieee.org Rakesh Ranjan - r_ranjan66@yahoo.com

Abstract

Power distribution systems are always exposed to disturbances, which can lead to voltage instability and collapse. The most important task for a distribution engineer is to identify the sensitive nodes and rank them according to their severity. This paper presents the application of fuzzy logic to define percentage reliability and accordingly define nodal reliability ranking of each node, considering reliability as a function of voltage and Voltage Stability Index. The variation in percentage reliability is also calculated due to the impact of load variation. The proposed technique is useful to ensure the reliability of distribution system by predicting the nearness of voltage collapse with respect to existing load conditions and can be used as an early warning so that the necessary action can be taken in order to avoid the occurrence of voltage collapse. For the load flow calculation purpose, a three phase fuzzy load flow algorithm for unbalanced radial distribution systems is developed, which is based on algebraic recursive expression of the voltage magnitude.

Index Terms— Branch Voltage, Fuzzy set, Nodal Reliability Ranking, Three phase load flow, Voltage Stability Index.

I. INTRODUCTION

IN modern power system, voltage stability is a major concern as systems operate at points which are steadily approaching the maximum operating limits. Voltage instability can lead to blackouts which is a major concern in the planning and operation of power system. Voltage instability is characterized by the variation in voltage magnitude which gradually decreases to a dangerously low value accompanied by simultaneous decrease in the power transfer to the load end from the source. Hence it is important to have a reliable power system, which will maintain the voltages within the permissible limits to ensure high quality of service. To maintain voltage stability, it is desirable to estimate the effect of any unforeseen events and identify nodes which are most sensitive.

Chi-Wen Liu presents a neurofuzzy network proposed for voltage security monitoring using synchronized phasor measurement [1]. A work on knowledge based system for supervision and control of regional voltage profile and security is presented in [2]. Manjaree Pandit

et al present fast voltage contingency selection using fuzzy parallel self organizing hierarchical Neural Network [3]. M.Aruna presents a new reconfiguration algorithm that enhances

voltage stability and improves the voltage profile[4]. Work on reconfiguration of the networks has already been reported which defines that the voltage stability can be maximized for a particular set of loads in the distributed systems [5,6,7].

A method for detecting voltage collapse in radial distribution systems is presented where two indicators for evaluating voltage stability of radial distribution systems are derived [8]. An algorithm for optimal locations and sizing of static and/or switched shunt capacitors is reported, with a view to enhance voltage stability [9]. Voltage stability analysis of radial distribution networks, where a new voltage stability index is proposed for identifying the nodes that are on the verge of voltage collapse, but does not use a fuzzy approach for the analysis [10]. Shobha presents the fuzzy approach for ranking the contingencies using composite index [11], for transmission network.

Hence, the literature review shows that the work done are mainly focused on enhancement techniques of voltage stability and not much work has been reported on the reliability analysis, describing the status of each node for a distribution system.

This paper presents the application of Fuzzy Logic for determining the percentage reliability and nodal ranking, considering percentage reliability as a function of voltage, stability index independently and also as a function of both voltage and stability index. The variation in nodal reliability ranking due to the impact of load changes is studied and an acceptable percentage reliability cut-off level is also proposed.

The paper is organized as follows. In section II, the methodology used for nodal reliability ranking is discussed. The bus voltage and the stability index are expressed in fuzzy notation and further processed through fuzzy reasoning rules using fuzzy logic. Section III, IV & V elaborate the nodal voltages, voltage stability index (SI) and percentage reliability computations with results. Section VI concludes the paper.

II. METHODOLOGY OF NODAL RELIABILITY RANKING

In recent years, fuzzy system applications have received increasing attentions in various areas of power systems. Fuzzy set based reasoning approach has been developed for nodal reliability ranking, which is a process of indexing each node and rank them according to their severity. The bus voltage and the stability index are expressed in fuzzy notation and further processed using fuzzy reasoning rules.

Nodal reliability ranking is basically done using following steps;

- Using fuzzy modeled load flow algorithm to calculate nodal voltages
- Using fuzzy modeled load flow algorithm to calculate voltage stability index (SI).
- Using fuzzy If-Then rules to calculate node's percentage reliability.
- Rank the nodes based on above.

III. FUZZY MODELED LOAD FLOW ALGORITHM TO CALCULATE NODAL VOLTAGES

For nodal voltage calculation, this paper uses an algorithm, as described in this section [12], modified to suite the fuzzy model. The load flow calculation methodology uses the basic systems analysis method and circuit theory and requires only the recursive algebraic equations to get the voltage magnitudes, currents & power losses at all the nodes. This load flow methodology also evaluates the total real and reactive power fed through any node.

A simple circuit model of the system is shown in Figure 1. The calculation uses Carson & Lewis matrix method, which takes into account the self and mutual coupling effects of the unbalanced three phase line section.

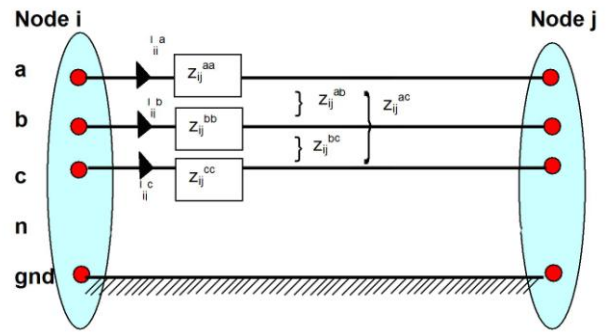


Fig. 1 – Three phase four wire line model

Using concept of simple circuit theory, the relation between the bus voltages and the branch currents in Figure 1 can be expressed as:

$$\begin{bmatrix} V_i^{ag} - V_j^{ag} \\ V_i^{bg} - V_j^{bg} \\ V_i^{cg} - V_j^{cg} \end{bmatrix} = \begin{bmatrix} V_j^a \\ V_j^b \\ V_j^c \end{bmatrix} = \begin{bmatrix} Z_{ij}^{aa} & Z_{ij}^{ab} & Z_{ij}^{ac} \\ Z_{ij}^{ba} & Z_{ij}^{bb} & Z_{ij}^{bc} \\ Z_{ij}^{ca} & Z_{ij}^{cb} & Z_{ij}^{cc} \end{bmatrix} \begin{bmatrix} I_{ij}^a \\ I_{ij}^b \\ I_{ij}^c \end{bmatrix} \quad (1)$$

Where

- V_i^{ag} = Voltage of phase a at node i with respect to ground
- V_i^{ab} = Voltage drop between two phases a and b at node i.
- V_{ij}^a = Voltage Drop between nodes i and j in phase a.
- I_{ij}^a = Current through phase a between nodes i and j.

Z_{ij}^{aa} = Self impedance between nodes i and j in phase a.

Z_{ij}^{ab} = Mutual impedance between phase a and b between nodes i and j.

P_i^a, Q_i^a, S_i^a = Real, reactive and complex power loads at phase a at ith bus.

S_{ij}^{phase} = Complex power at phase (a, b and c) between nodes i and j.

PL_{ij}^{phase} = Real power loss in the line between node i and j.

QL_{ij}^{phase} = Reactive power loss in the line between node i and j.

$SL_{ij}^{phase} = PL_{ij}^{phase} + jQL_{ij}^{phase}$

Rewriting (1)

$$\begin{bmatrix} V_j^a \\ V_j^b \\ V_j^c \end{bmatrix} = \begin{bmatrix} V_i^a \\ V_i^b \\ V_i^c \end{bmatrix} - \begin{bmatrix} Z_{ij}^{aa} & Z_{ij}^{ab} & Z_{ij}^{ac} \\ Z_{ij}^{ba} & Z_{ij}^{bb} & Z_{ij}^{bc} \\ Z_{ij}^{ca} & Z_{ij}^{cb} & Z_{ij}^{cc} \end{bmatrix} \begin{bmatrix} I_{ij}^a \\ I_{ij}^b \\ I_{ij}^c \end{bmatrix}$$

Following equations gives the branch currents between the nodes i and j:

$$\begin{aligned} I_{ij}^a &= (P_{ij}^a + jQ_{ij}^a) / V_j^a \\ I_{ij}^b &= (P_{ij}^b + jQ_{ij}^b) / V_j^b \\ I_{ij}^c &= (P_{ij}^c + jQ_{ij}^c) / V_j^c \end{aligned}$$

The real and reactive power losses in the line between buses i and j are written as;

$$\begin{aligned} SL_{ij}^a &= PL_{ij}^a + jQL_{ij}^a = V_i^a * (I_{ij}^a) - V_j^a * (I_{ji}^a) \\ SL_{ij}^b &= PL_{ij}^b + jQL_{ij}^b = V_i^b * (I_{ij}^b) - V_j^b * (I_{ji}^b) \\ SL_{ij}^c &= PL_{ij}^c + jQL_{ij}^c = V_i^c * (I_{ij}^c) - V_j^c * (I_{ji}^c) \end{aligned}$$

The program computes the real & reactive power and uses the formula given in equation no. (2) Receiving end power at any phase, say phase a, of line between the nodes i and j is expressed as:

$$P_{ij}^a + jQ_{ij}^a = \left[\sum_{K=\text{index of all nodes fed through the line between nodes i and j}} [P_{kj}^a + jQ_{kj}^a] \right] + \left[\sum_{\text{index of all lines connected between nodes m and n fed through the line between nodes i and j}} [PL_{mn}^a + jQL_{mn}^a] \right] \quad (2)$$

For modeling and simulation purpose this paper uses an input data for a 19 bus distribution system shown in Figure 2 [13]. Load data for the feeders are given in Appendix 1. Figure 3 shows the flow chart for simulation.

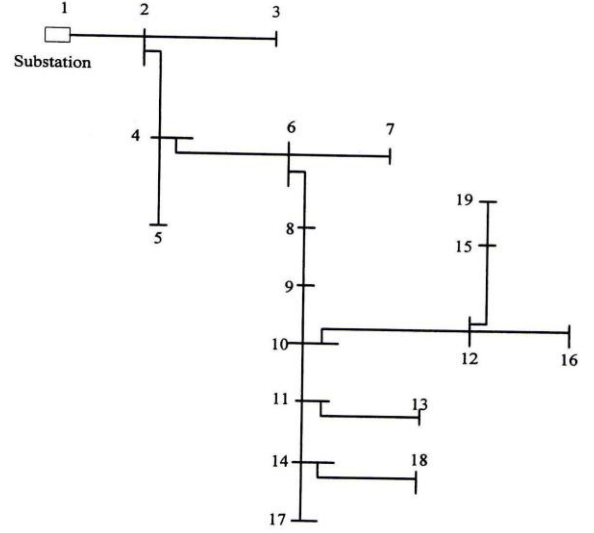


Fig. 2. - A practical 19 bus distribution feeder used for the modeling and simulation purpose.

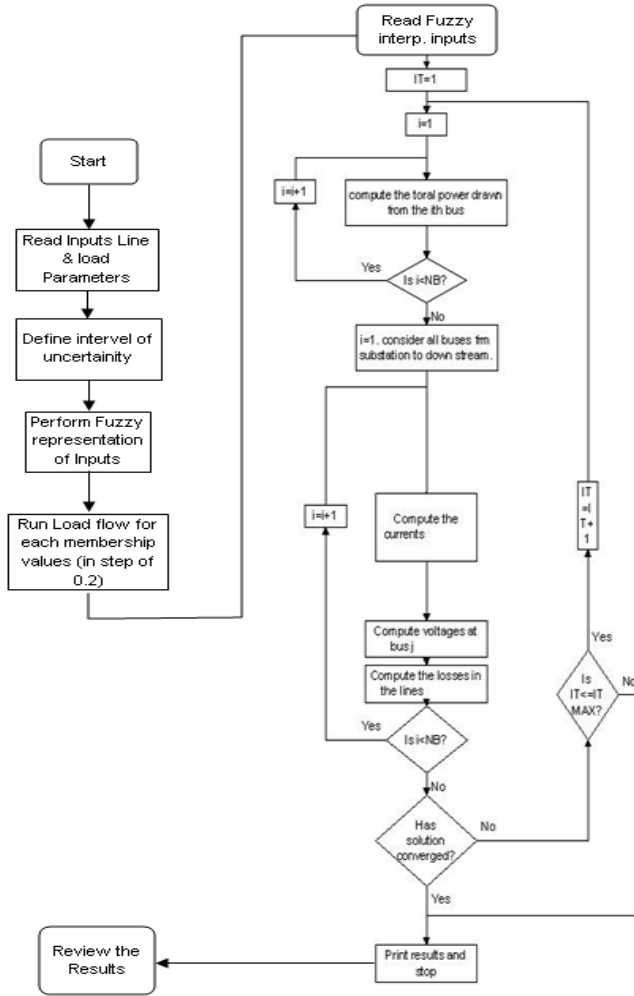
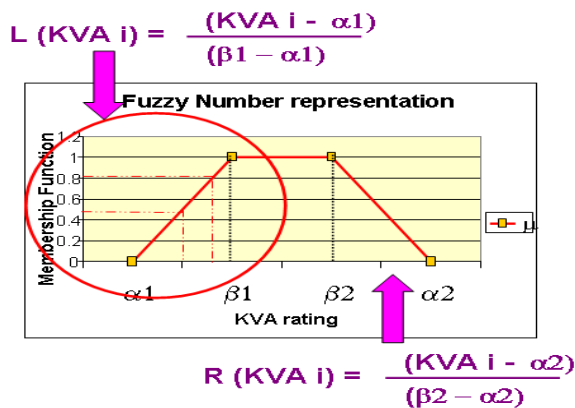


Fig. 3 - Typical Fuzzy Load Flow calculation chart used

Fig. 4 - Fuzzification of kVA rating
Where, $\alpha_1 = 20\%$, $\alpha_2 = 135\%$, $\beta_1 = 95\%$, $\beta_2 = 105\%$

For evaluation purpose, the feeder parameters are assumed unchanged and uncertainties are assumed only

to the connected load parameters. An uncertain load can be represented by a fuzzy number that is in fact a membership function over the real set. Fuzzy numbers may have variety of shapes but here trapezoidal membership function is chosen. This shape is chosen from the fact that there are several points whose membership degree is maximum ($\mu=1$).

A linguistic declaration such as “peak values of load will not occur below 20 Percentage or above 135 Percentage, and the least estimation is, say between 95 Percentage and 105 Percentage of the rated capacity” can be translated into a fuzzy number as shown in Figure 4 as per [14].

For each value of μ (KVA), two different values of KVA loads can be obtained i.e. the L (KVA) & the R (KVA). Therefore, for each membership value, two load flow runs are required. Membership function μ (KVA) is taken in steps of 0.2. Table 1 shows the calculated nodal voltages for loads at μ (KVA) of 0.4 (Left) & 0.6 (Left).

TABLE 1.
CALCULATED NODAL VOLTAGES FOR μ (KVA) OF 0.4 (LEFT) & 0.6 (LEFT)

Node no.	μ Membership function of voltage magnitude					
	0.4			0.6		
	Ph A	Ph B	Ph C	Ph A	Ph B	Ph C
1	1	1	1	1	1	1
2	0.991	0.992	0.997	0.988	0.989	0.995
3	0.989	0.991	0.992	0.986	0.988	0.989
4	0.987	0.988	0.991	0.983	0.984	0.987
5	0.987	0.988	0.988	0.983	0.984	0.984
6	0.985	0.986	0.987	0.980	0.981	0.983
7	0.985	0.985	0.986	0.980	0.981	0.981
8	0.980	0.981	0.985	0.974	0.975	0.979
9	0.975	0.975	0.980	0.967	0.967	0.973
10	0.968	0.968	0.974	0.958	0.957	0.965
11	0.967	0.967	0.968	0.956	0.956	0.957
12	0.967	0.967	0.968	0.957	0.956	0.957
13	0.966	0.966	0.967	0.955	0.955	0.956
14	0.966	0.966	0.967	0.955	0.955	0.956
15	0.966	0.965	0.967	0.955	0.954	0.956
16	0.967	0.966	0.967	0.956	0.955	0.956
17	0.965	0.965	0.966	0.954	0.954	0.955
18	0.965	0.965	0.966	0.954	0.953	0.955
19	0.965	0.965	0.965	0.954	0.953	0.954

Figure 5 shows the calculated nodal voltages for all KVA membership functions for Phase A. One can notice that for certain group of nodes, nodal voltages are more sensitive to

load variation and drops sharply. Similarly, fuzzy modeled load flow algorithm is used to calculate the nodal voltage trend and subsequently calculating the nodal ranking.

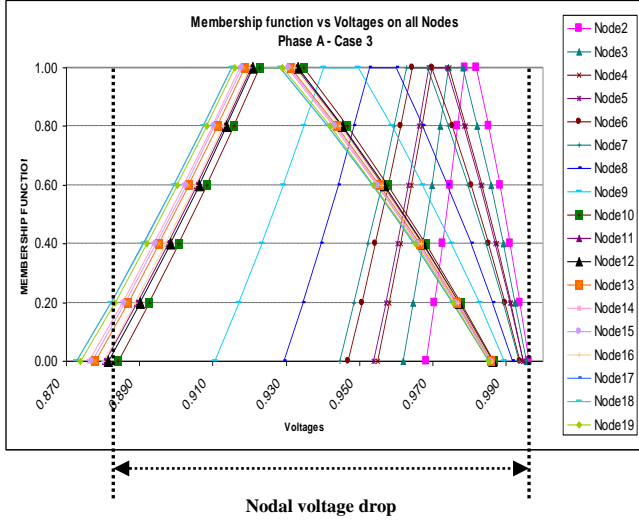


Fig. 5 - Calculated Nodal Voltages for all KVA Membership functions for Phase A

IV. FUZZY MODELED LOAD FLOW ALGORITHM TO CALCULATE VOLTAGE STABILITY INDEX (SI)

Voltage stability is the ability of a power system to maintain steadily acceptable bus voltage at each node under normal operating conditions, following load increases, system configuration changes or a disturbance. The progressive and uncontrollable drop in voltage eventually results in a wide spread voltage collapse.

This section calculates the voltage stability index (SI) for all the nodes of the radial distribution system using the load flow results. There are several methods to estimate or predict the voltage stability condition of a power system. This study utilizes the voltage stability index [15] in order to indicate the voltage stability condition at each bus of the system.

For a typical RDS, any line between the bus 'i' and 'j' can be represented by an equivalent single line represented as given in Figure 6.

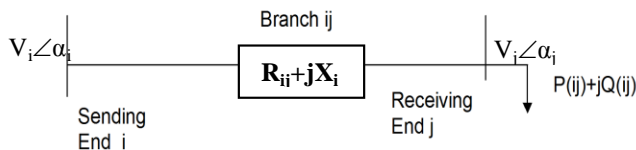


Fig. 6 - Electrical equivalent of one branch

The complex power flowing into the receiving end will be $P_{ij} + jQ_{ij}$, where P & Q stand for real and reactive power.

The governing circuit equations are:

$$V_i \angle \alpha_i - V_j \angle \alpha_j = I_{ij} (R_{ij} + jX_{ij}) \quad (3)$$

$$(V_i \angle \alpha_i)^* I_{ij} = P_{ij} - jQ_{ij}; \quad (4)$$

* = complex conjugate operation

By solving the above two equations and with the assumption that for a typical radial distribution system ($\angle \alpha_i - \angle \alpha_j$) is typically very small value, hence the assumption

$$\cos(\angle \alpha_i - \angle \alpha_j) \approx 1 \quad \& \quad \sin(\angle \alpha_i - \angle \alpha_j) \approx 0$$

With the above assumption, it is derived that

$$V_j^2 - V_i V_j + (P_{ij} R_{ij} + Q_{ij} X_{ij}) = 0 \quad (5)$$

Therefore,

$$V_j = \{V_i \pm \sqrt{V_i^2 - 4(P_{ij} R_{ij} + Q_{ij} X_{ij})}\} / 2 \quad (6)$$

Eq (6) results in two possible solutions for the receiving end voltage V_j . However, the feasible solution is the minimum of the two as the voltage towards the receiving end is typically lower than its sending end voltage.

Thus, V_j can be taken as,

$$V_j = \{V_i - \sqrt{V_i^2 - 4(P_{ij} R_{ij} + Q_{ij} X_{ij})}\} / 2 \quad (7)$$

Since the voltage magnitude is always the real quantity, hence;

$$V_i^2 - 4(P_{ij} R_{ij} + Q_{ij} X_{ij}) \geq 0 \quad (8)$$

From this, the stability index for the bus j (SI) is derived as

$$SI = \frac{V_i^2 - 4(P_{ij} R_{ij} + Q_{ij} X_{ij})}{V_i^2} \quad (9)$$

The value of SI varies from 0 to 1. For stable

operation of the RDS, stability Index should be nearing one. If the SI is nearing 0, this reflects an unstable bus.

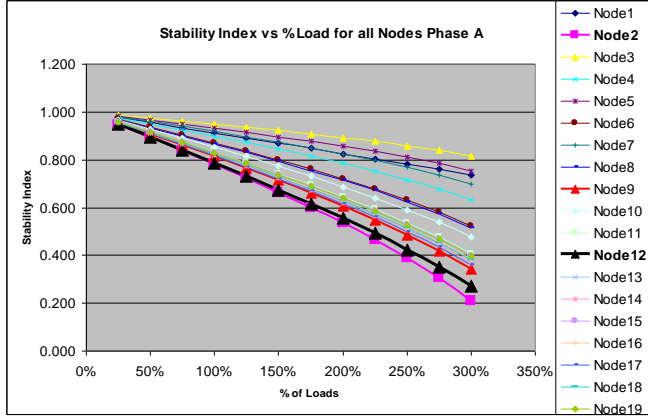


Fig. 7. - Stability Index variation with Load Changes

Figure 7 shows the typical variation of stability index based on load variation for all the nodes. One can note that for few nodes (e.g. Node 2, 12) stability index value dips sharply at higher loads tending towards instability.

V. FUZZY 'IF-THEN' RULES TO CALCULATE PERCENTAGE RELIABILITY OF A NODE.

This paper proposes fuzzy approach and uses voltage and SI of each node to calculate the percentage reliability and reliability ranking of the node. The bus voltage and the SI are selected as the crisp input parameters and expressed as fuzzy set notation.

The fuzzy 'If-Then' rules are used to evaluate the percentage-reliability of each node. Finally after defuzzification the crisp value of the output mentioning the percentage reliability of a node is calculated. Using the same methodology, individual impact of voltages and SI on the percentage reliability can also be calculated. For calculation purpose a trapezoidal membership functions is assumed for bus voltage and SI profile and are represented in fuzzy set notation. The bus voltage profiles are divided into five triangular membership functions, as indicated in Figure 8.

Fuzzy Interpretation of voltage (V);

If $V < 0.925$, then 'Unstable (UN)'

If $V = 0.9 - 0.95$, then 'Less Stable (LS)'

If $V = 0.925 - 0.975$, then 'Moderately Stable (MS)'

If $V = 0.95 - 1.0$, then, 'Stable (S)' &

If $V > 0.975$, then, 'Over range (Over)'.

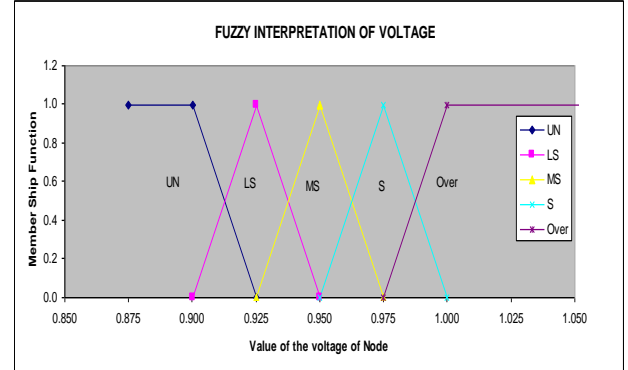


Fig. 8 - Fuzzy number representation

Similarly the 'SI' profiles are divided into five triangular membership functions using fuzzy set notations, as given in Figure 9.

Fuzzy Interpretation of SI;

If $SI < 0.85$, then 'Unstable (UN)'

If $SI = 0.8 - 0.9$, then 'Less Stable (LS)'

If $SI = 0.85 - 0.95$, then 'Moderately Stable (MS)'

If $SI = 0.9 - 1.0$, then, 'Stable (S)'

If $SI > 0.975$, then, 'Over range (Over)'

Using fuzzy 'If-Then' rules overall percentage reliability is calculated based on both the voltage and SI profiles.

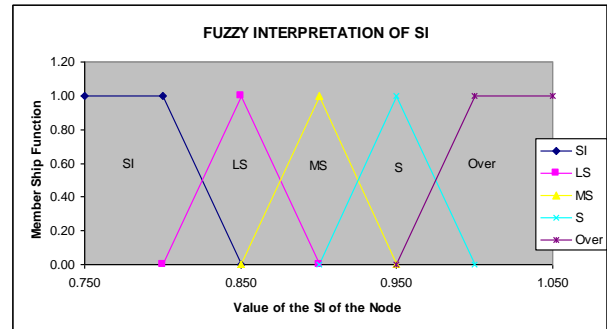


Fig. 9 - Fuzzy number representation

Fuzzy 'If then' rules shown in table 3 are used for calculation purpose;

Let for a node; Voltage = V and Stability Index = SI
Then the corresponding membership values for each zone of the five triangular membership functions can be defined as given in table 2.

TABLE 2.

CALCULATED NODAL VOLTAGES FOR μ (KVA)
OF 0.4 (LEFT) & 0.6 (LEFT)

	Membership Values	
	Voltage	SI
UN	Av	SIa
LS	Bv	SIb
MS	Cv	SIc
Stable	Dv	SId
Over	Ev	SIe

TABLE 3
'IF THEN' RULES

R1	If V<0.925	AND	SI<0.85	Then 'UN'	Min	Av & SIa
R2	If V=0.9-0.95	AND	SI<0.85	Then 'UN'	Min	Av & SIa
R3	If V=0.925-0.975	AND	SI<0.85	Then 'UN'	Min	Av & SIa
R4	If V=0.95-1.0	AND	SI<0.85	Then 'LS'	Min	Bv & SIb
R5	If V>0.975	AND	SI<0.85	Then 'LS'	Min	Bv & SIb
R6	If V<0.925	AND	SI=0.8-0.9	Then 'UN'	Min	Av & SIa
R7	If V=0.9-0.95	AND	SI=0.8-0.9	Then 'LS'	Min	Bv & SIb
R8	If V=0.925-0.975	AND	SI=0.8-0.9	Then 'LS'	Min	Bv & SIb
R9	If V=0.95-1.0	AND	SI=0.8-0.9	Then 'MS'	Min	Cv & SIc
R10	If V>0.975	AND	SI=0.8-0.9	Then 'S'	Min	Dv & SId
R11	If V<0.925	AND	SI=0.85-0.95	Then 'UN'	Min	Av & SIa
R12	If V=0.9-0.95	AND	SI=0.85-0.95	Then 'MS'	Min	Cv & SIc
R13	If V=0.925-0.975	AND	SI=0.85-0.95	Then 'MS'	Min	Cv & SIc
R14	If V=0.95-1.0	AND	SI=0.85-0.95	Then 'S'	Min	Dv & SId
R15	If V>0.975	AND	SI=0.85-0.95	Then 'S'	Min	Dv & SId
R16	If V<0.925	AND	SI=0.9-1.0	Then 'UN'	Min	Av & SIa
R17	If V=0.9-0.95	AND	SI=0.9-1.0	Then 'MS'	Min	Cv & SIc
R18	If V=0.925-0.975	AND	SI=0.9-1.0	Then 'S'	Min	Dv & SId
R19	If V=0.95-1.0	AND	SI=0.9-1.0	Then 'S'	Min	Dv & SId
R20	If V>0.975	AND	SI=0.9-1.0	Then 'S'	Min	Dv & SId
R21	If V<0.925	AND	SI>0.975	Then 'UN'	Min	Av & SIa
R22	If V=0.9-0.95	AND	SI>0.975	Then 'MS'	Min	Cv & SIc
R23	If V=0.925-0.975	AND	SI>0.975	Then 'S'	Min	Dv & SId
R24	If V=0.95-1.0	AND	SI>0.975	Then 'S'	Min	Dv & SId
R25	If V>0.975	AND	SI>0.975	Then 'O'	Min	Ev & SIv

The strengths for five triangular membership functions are shown in equation no (10).

Formula	Output Strength
UNs	$(R1^2+R2^2+R3^2+R6^2+R11^2+R16^2+R21)^{0.5} = a$
LSs	$(R4^2+R5^2+R7^2+R8^2)^{0.5} = b$
MSs	$(R9^2+R12^2+R13^2+R17^2+R22^2)^{0.5} = c$
Ss	$(R10^2+R14^2+R15^2+R18^2+R19^2+R20^2+R23^2+R24^2)^{0.5} = d$
Over (s)	$(R25^2)^{0.5} = e$

(10)

TABLE 4
OUTPUT RANGE CONSIDERED FOR RANKING & PERCENTAGE
RELIABILITY CALCULATION.

Output Range

Unr	=	0	=	0%
LSr	=	0.3	=	30%
MSr	=	0.5	=	50%
Sr	=	0.9	=	90%
Over@	=	1	=	100%

Table 4 shows the output ranges for percentage reliability assumed and uses defuzzification calculations given in equation (11) to find the crisp value of percentage reliability of each node.

$$\text{OUTPUT} = \frac{(\text{Unr} \cdot \text{UNs} + \text{LSr} \cdot \text{LSs} + \text{MSr} \cdot \text{MSs} + \text{Sr} \cdot \text{Ss} + \text{Over}(r) \cdot \text{Over}(s))}{(\text{Unr} + \text{LSr} + \text{MSr} + \text{Sr} + \text{Over}(r))} \quad (11)$$

The above procedure is repeated for all the buses to calculate the output percentage reliability of the nodes.

According to the output range shown in table 4 the cut-off level below 20 percentage (i.e 0.2) is assumed as unreliable node and prone for voltage collapse. Further ranking of nodes is done on the basis of their percentage reliability calculated after defuzzification. The higher rank (i.e rank 1, 2, 3...) indicates unstable nodes.

The result based on above methodology is shown in table 5, which gives percentage reliability of each node for 19 bus system. The results shown are for two loads i.e. 82 percent and 111 percent of base loads. One can notice that as the load increases, the percentage reliability generally decreases. However certain nodes become more stable as the load increases. In reference example all the nodes from 10 to 19 tends to become unstable (below 20 percent) at higher loads. The percentage reliability depends on the output range assumed. A different output range will shift the reliability windows for nodes. One can run this simulation for various load combination.

Table 6 shows the nodal stability ranking. The ranking is based on the percentage reliability values. Table 6 depicts the rounded values; however for nodal ranking the actual percentage values are used. Values with lower percentage indicates a higher rank showing nodes towards instability. One can notice that ranking of

various nodes are different at different loads. Figure 10, shows the typical changes to nodal rankings based on load changes. The figure gives a snap shot of nodal ranking changes based on load variations. It may be noted that the loads connected away from the substation (Node 12, 13, 14, 16 & 17) tends to get unstable on higher loads. For Certain nodes (e.g node 2) ranking actually improves.

TABLE 5
‘PERCENTAGE RELIABILITY AS VOLTAGE & SI

Node	82% Load			111% Load		
	Phase A	Phase B	Phase C	Phase A	Phase B	Phase C
1	51%	51%	51%	51%	51%	51%
2	90%	90%	90%	51%	51%	51%
3	51%	51%	51%	90%	90%	86%
4	91%	90%	90%	50%	50%	50%
5	89%	87%	83%	79%	76%	73%
6	90%	89%	87%	50%	50%	50%
7	65%	50%	50%	66%	63%	59%
8	83%	76%	73%	47%	31%	30%
9	50%	47%	47%	51%	51%	51%
10	35%	30%	30%	28%	9%	11%
11	41%	35%	35%	8%	1%	3%
12	37%	33%	34%	0%	0%	0%
13	30%	30%	30%	1%	0%	0%
14	32%	31%	31%	1%	0%	0%
15	31%	30%	30%	1%	0%	0%
16	33%	32%	33%	2%	0%	2%
17	30%	30%	30%	0%	0%	0%
18	30%	30%	29%	0%	0%	0%
19	30%	30%	30%	0%	0%	0%
Un stable Zone						

TABLE 6
NODAL STABILITY RANKING BASED ON PERCENTAGE RELIABILITY

Node	82% Load			111% Load		
	Phase A	Phase B	Phase C	Phase A	Phase B	Phase C
1	12	13	13	14	14	14
2	17	18	18	14	14	14
3	12	13	13	19	19	19
4	19	19	19	12	12	12
5	16	16	16	18	18	18
6	18	17	17	13	13	13
7	14	12	12	17	17	17
8	15	15	15	11	11	11
9	11	11	11	14	14	14
10	8	4	4	10	10	10
11	10	10	10	9	9	9
12	9	9	9	3	5	4
13	1	5	5	6	8	7
14	6	7	7	5	1	1
15	5	6	6	7	6	5
16	7	8	8	8	1	8
17	4	2	3	1	1	1
18	3	1	1	2	4	3
19	2	3	2	4	7	6

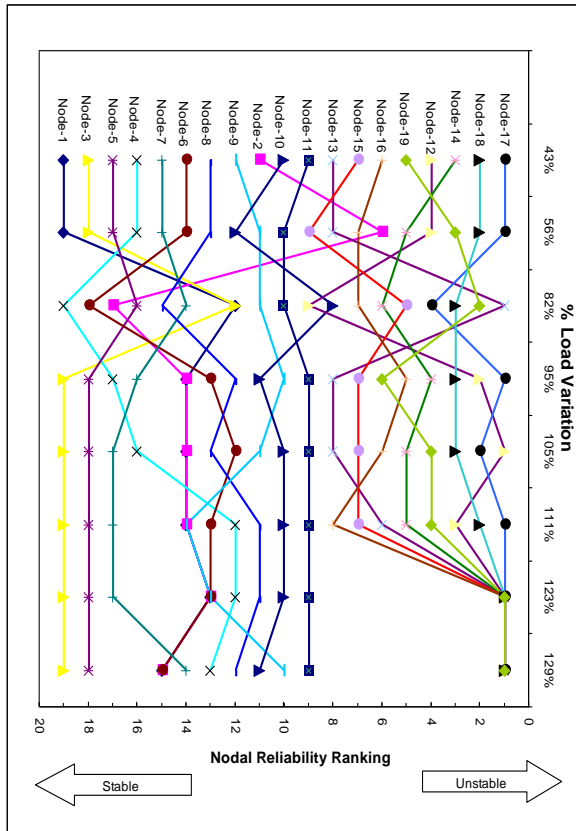


Fig. – 10 Typical changes to nodal rankings based on load changes

VI. CONCLUSION

This paper uses the application of fuzzy logic to define percentage reliability and accordingly define nodal reliability ranking for a typical RDS. The simulation uses fuzzy based load flow algorithm to calculate nodal parameters and voltage stability index, which are further used as an input to model the fuzzy based reliability ranking algorithm. The result shows the possible Nodal reliability distribution of all the nodes at glance and gives a good idea about the network as a whole.

Using the proposed methodology, all possible scenarios are modeled and comparison is drawn for a wide variation in loads. The proposed technique is useful to ensure the reliability of distribution system by predicting the nearness of voltage collapse with respect to existing load conditions and can be used as an early warning. This can also be used during initial stages of planning and design studies.

APPENDIX

Input Load & Line data table.

Table – A Load data

Node	Phase Load in KVA		
	A	B	C
2	64	32	64
3	68	32	60
4	25	35	40
5	40	32	28
6	26	19	18
7	60	50	50
8	46	33	21
9	76	92	82
10	21	26	16
11	46	46	68
12	60	50	50
13	27	33	40
14	19	19	25
15	27	30	43
16	48	64	48
17	40	30	30
18	33	33	34
19	54	62	44

Table – B Conductor data

Conductor type	Resistance PU/Km	Reactance PU/Km
1	0.008600	0.003700
2	0.012950	0.003680

Table – C Conductor Code & Distances

Sending End Node(IR)	Receiving End Node(IR)	Conductor Code	Distance in Km
1	2	1	3
2	3	2	5
2	4	1	1.5
4	5	2	1.5
4	6	1	1
6	7	2	2
6	8	1	2.5
8	9	1	3
9	10	1	5
10	11	1	1.5
10	12	1	1
11	13	2	5
11	14	1	3.5
12	15	1	4

Sending End Node(IR)	Receiving End Node(IR)	Conductor Code	Distance in Km
12	16	2	1.5
14	17	1	6
14	18	2	5
15	19	1	4

REFERENCES

- [1] Chi-wen Liu, Chen-Sung, Mu-Chun Su, “Neuro-Fuzzy Networks for Voltage Security Monitoring Based on Synchronized Phasor Measurements” IEEE transactions on power systems, vol13, No.2, Pages 326-332, May 1998.
- [2] Alessandro B. Marques, Glauco N. Taranto, Djalma M. falcao, “ A knowledge Based System for Supervision and Control of Regional Voltage Profile and Security”, IEEE transactions on power systems, vol20. No.4, Pg 400-407, Feb 2008.
- [3] Manjaree Pandit et al, M. Srivastav, L. Sharma “Fast Voltage Contingency Selection using Fuzzy Parallel Self Organizing Hierarchical Neural Network”, IEEE Transactions on power systems, Vol. 18, No.2, Pages 657-664, May 2003.
- [4] M. Aruna, P. Aravindhbabu, “A new reconfiguration scheme for voltage stability enhancement of radial distribution systems”, Energy Conversion and Management Volume 50, Issue 9, Sept 2009, Pages 2148-2151.
- [5] S. Senthil, P. Ajay-D-Vimal Raj, “Fuzzy logic based stability index power system voltage stability enhancement”, International journal of computer and electrical engineering, Vol.2, No.1, Pages.24-30 Feb, 2010
- [6] S. Sivanagaraju; N. Visali; V. Sankar; T. Ramana, “Enhancing Voltage Stability of Radial Distribution Systems by Network Reconfiguration”, Electric Power Components and Systems, Volume 33, Issue 5 March 2005, pages 539 – 550
- [7] Prasad, N. C. Sahoo, “Modeling and simulation for voltage stability enhancement in radial distribution systems by reconfiguration” International Association Of Science And Technology For Development archive Proceedings of the 19th IASTED International Conference on Modelling and Simulation table of contents Session: Energy

and power systems table of contents Pages: 394-399
Publication: 2008

- [8] Hamada, M.M. "Fast Detection of Voltage Collapse Proximity in Radial Distribution Systems", Universities Power Engineering Conference, sept.2006. UPEC '06. Proceedings of the 41st International Vol.3, Pg1006 – 1010.
- [9] Aravindhababu P. and Mohan G, "optimal capacitor placement for voltage stability enhancement in distribution systems", ARPJN Journal of Engineering and Applied Sciences, VOL. 4, NO. 2, Pages 88-92 APRIL 2009 ISSN 1819-6608
- [10] R. Ranjan; D. Das, "Voltage Stability Analysis of Radial Distribution Networks", Electric Power Components and Systems, Volume 31, Issue 5 May 2003 , pages 501 - 511
- [11] Shobha Shankar, A.P. Suma, T. Ananthapadmanabha, " Fuzzy approach to Contingency Ranking" International Journal of recent trends in Engineering, Vol.1, No.1 Pages 490-494, May 2009.
- [12] R.Ranjan, B.Venkatesh, A.Chaturvedi, "Power Flow solution of three phase unbalanced Radial Distribution Network", Journal of Electrical Power Components and Systems, USA, 32:421-433, 2004
- [13] D. Thukram, H.M W.Banda, and J. Jerome," A robust three phase power flow algorithm for radial distribution systems," Journal of Electrical Power Systems Research, vol.50, no. 3, pp.227-236, June 1999
- [14] D.Das, S. Ghosh, D.k. Srinivas, " Fuzzy Distribution Load Flow," Electrical Machines and power systems, 27:1215-1226, 1999.
- [15] N.C. Sahoo, K Prasad, " A Fuzzy genetic approach for network reconfiguration to enhance voltage stability in radial distribution systems", Energy Conversion & Management 47(2006) 3288-3306.

Author's Profile

Mini. S. Thomas (M-88, SM-99), graduated from university of Kerala, completed her M. Tech from IIT Madras both with gold medals & Ph.D from IIT Delhi all in Electrical Engineering. Her employment experiences include Regional Engineering College Calicut, Kerala, Delhi College of Engineering, New Delhi and presently as professor in the Faculty of Engg.

& Tech., Jamia Millia Islamia, New Delhi. Mini received the prestigious 'Career Award' for young teachers, instituted by Govt. of India for the year 1999. She has published 60 papers in International/National Journals & conferences. Her current research interests are in SCADA systems, smart grid and intelligent protection of power systems.

Prof. Rakesh Ranjan has received the Bachelor of Engineering (Electrical Eng.) from MIT Muzaffarpur, ME from BIT, Mesra, Ranchi and Ph.D. from BITS, Pilani, India. Dr. Ranjan has more than 20 years of teaching and research experience at Indian and foreign Universities. He has co-authored books entitled "Renewable Energy Resource", PHI, India, "Signals and Systems" published by McGraw-Hill, Singapore / Tata McGraw-Hill, New Delhi, India, on "Random Process and Queuing Theory", "Circuits and Signals" published by Pearson, Prentice Hall, Malaysia and "Schaum's Outlines on SIGNALS AND SYSTEMS" is published by Tata McGraw-Hill, New Delhi. He has contributed 23 research papers in international journals and 41 papers at international conferences in the area of Radial distribution systems

Roma Raina did her Bachelors in Controls & Instrumentation in 1994 from the Regional Engineering College Jalandhar (Punjab) and Masters in Controls & Instrumentation from Delhi college of Engineering in year 2005. She has 16 years of teaching experience. She is teaching at Manipal University's Dubai Campus. Specialization in control and instrumentation, Ms. Roma Raina has guided number of projects based on measurement, control and fuzzy logic. She is life time member of ISTE & member of IEEE & IASTED.

INVESTIGATION OF INSECTICIDAL ACTIVITY OF SOME α,β -UNSATURATED CARBONYL COMPOUNDS AND THEIR SYNERGISTIC COMBINATION WITH NATURAL PRODUCTS AGAINST *PHENACOCCLUS SOLENOPSIS* TINSLEY

Archna Rani^{1*}, Sapna Jain¹, Ram Das Gautam²

¹ Department of Applied Chemistry, Delhi Technological University (Formerly Delhi College of Engineering), Bawana Road, Delhi-110042, India

² Biological Control Laboratory, Division of Entomology, Indian Agricultural Research Institute, New Delhi-110012, India

Received: October 14, 2010

Accepted: November 2, 2011

Abstract: In continuation of our previous work, the current study explores an environmentally benign approach for the control of *Phenacoccus solenopsis* Tinsley (Hemiptera: Pseudococcidae) using a synergistic combination of α,β -unsaturated carbonyl compounds (1a-1e; 2a-2i) and the natural products, neem oil (N1) and nicotinic acid (N2). Our approach also evaluates the insecticidal activity of 3-(5-chloro-1,3-diaryl-1H-pyrazol-4-yl)-1-arylprop-2-en-1-one (2j-2o) consisting of bioactive moieties, viz., chalcone and pyrazole, in a single molecular structure. Compounds 2l and 2o exhibited maximum activity with 58% and 50 % of mortality, respectively, under laboratory conditions. Among various test combinations, 2a-N2 showed maximum insecticidal activity, with 54% mortality, comparable to that of the most active newly synthesized compound, 2l, followed by 1c-N1 and 2g-N2 with 52% mortality. The compound 2a was also found to be non-toxic to potato tuber used as a plant substrate in the current investigation.

Key words: insecticidal, *Solanum* mealy bug, chalcones, pyrazole, neem oil, nicotinic acid

INTRODUCTION

The *Solanum* mealy bug (SMB) or *Phenacoccus solenopsis* Tinsley (Hemiptera: Pseudococcidae) also known as cotton mealy bug is one of the most devastating of the sap sucking polyphagous pests. The insect was noted for the first time in USA in 1898, and then its distribution subsequently spread to Canada, Latin America, the Caribbean in Western Hemisphere, South Africa, Zimbabwe, the Hawaiian Islands, Italy, Taiwan, Kiribati, the Gilbert Islands, Sicily, Israel and very recently to India (Chen *et al.* 2002; Santa *et al.* 2002; Dov 2005; Gautam *et al.* 2007; Akintola and Ande 2008). Among various host plants, cotton, eggplant, and sunflower are the most preferred food plants for this mealy bug. This bug can damage up to 80% of crops (Nalwar *et al.* 2009). The main difficulty in managing the SMB is their high reproductive potential, and their ability to survive under extreme weather conditions. The mealy waxy coating on its body also makes it difficult to manage this bug.

Current management of these insects is mainly based on spraying with organophosphorous and organochlorine pesticides like chlorpyrifos, monocrotophos and endosulfan (Fig. 1a, b, c).

It is well documented that continuous use of these pesticides have created problem of resistance, and resurgence, and harmful impact on the environment as well as

on humans. The replacement of toxic chemicals with compatible, environmentally friendly natural products, have their own limitations viz., less potency, lesser availability, structural complexity and instability. This necessitates the development of newer approaches to control these kinds of pests. For this reason, the current investigation is focused on (i) fabrication of compounds incorporating various bioactive fragments in a single molecule to improve bioactivity and minimize possibilities of resistance, and (ii) a broad spectrum screening of already existing bioactive compounds in combination with natural products, to reduce the concentration of synthetic compounds and natural products, while preserving and/or improving the efficacy of the products.

Our previous studies have established the broad spectrum biological activities of α,β -unsaturated carbonyl compounds (1a-1e and 2a-2i) in combination with natural products viz., neem (*Azadirachta indica*) oil (N1), and nicotinic acid (N2). These combinations are known for their wide range of application in agriculture and pharmacology (Jermy 1990; Devkumar and Sukhdev 1993; Bodor and Offermanns 2008; Gupta *et al.* 2008), against human pathogenic bacteria, and plant pathogenic fungi (Rani *et al.* 2009a; Rani *et al.* 2009b). We extended our work to evaluate these synergistic combinations for insecticidal activity against *P. solenopsis*.

*Corresponding address:
archna.rani@gmail.com

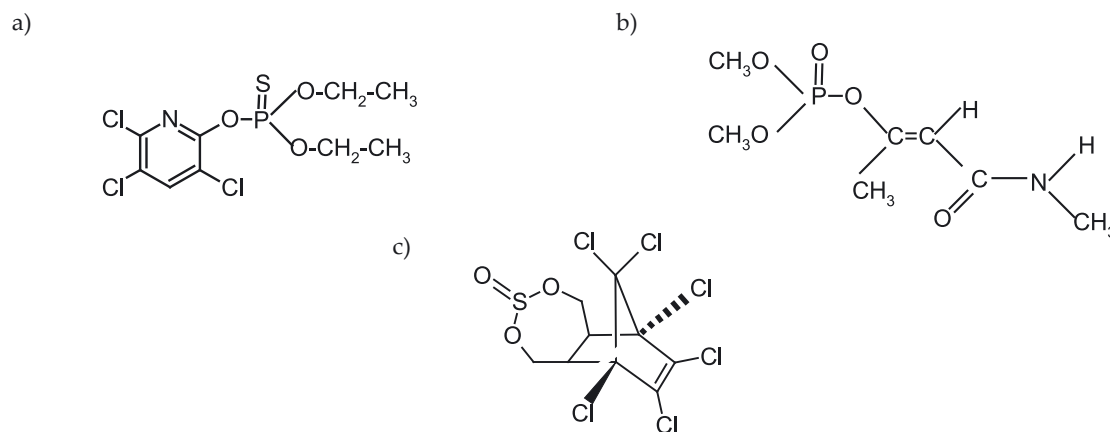


Fig. 1. a) Chlorpyrifos; b) Monocrotophos; c) Endosulfan

At the same time, chalcone derivatives containing pyrazole nucleus (2j-2o) were synthesized and screened against *P. solenopsis*.

These moieties are well documented for their multifaceted biological activities *viz.*, insecticidal (Dimmock *et al.* 1999; Shiga *et al.* 2003), antifungal (Akbas and Berber 2005; Lahtchev *et al.* 2008), antioxidant (Anto *et al.* 1995; Bhat *et al.* 2005; Arty *et al.* 2000), tyrosinase inhibitory (Dominguez *et al.* 2005), antimetabolic (Boumendjel *et al.* 2008), and antibacterial activity (Sivakumar *et al.* 2007; Rani and Jain 2008; Liu *et al.* 2008).

MATERIALS AND METHODS

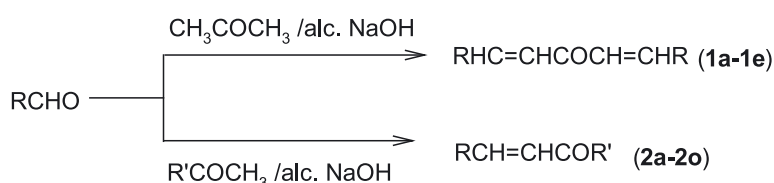
Synthesis

All of the reported structural modifications were carried out by classical aldol condensation involving base-catalyzed condensation of the desired carbonyl com-

pounds followed by dehydration forming α,β -unsaturated carbonyl compounds. The detailed synthetic route is described below.

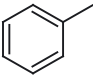
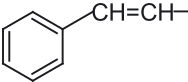
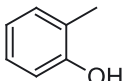
In the case of compounds 2j-2o, the desired aldehyde was obtained by following the reported method (Gupta *et al.* 2009).

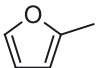
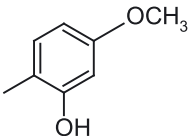
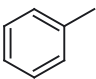
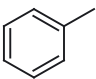
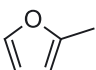
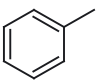
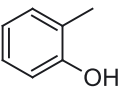
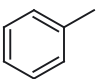
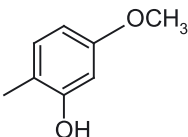
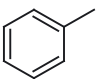
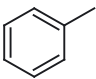
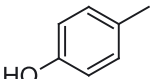
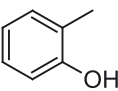
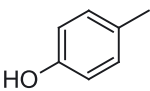
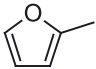
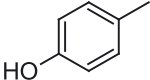
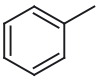
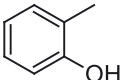
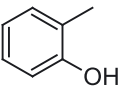
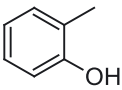
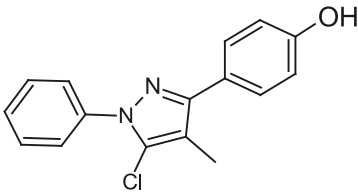
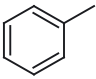
In a two-necked round-bottomed flask, equipped with a mechanical stirrer, a solution of the desired aldehyde (0.01 mol), was added to the required amount of alcoholic NaOH. Acetone (0.02 mol for 1a-1e) or the requisite aldehyde (0.01 mol for 2a-2o) was added slowly from a dropping funnel while being vigorously shaken. The reaction mixture was maintained at 25°C. The reaction was completed in 40-45 min with the formation of yellow precipitate. If no precipitation occurred, the reaction mixture was kept in a refrigerator overnight. The precipitate was filtered out and recrystallized using an appropriate solvent (Furniss *et al.* 2005) (Table 1).

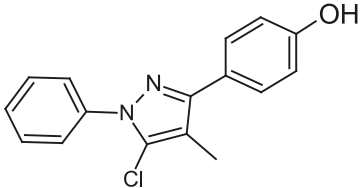
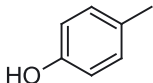
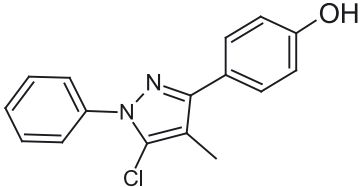
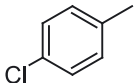
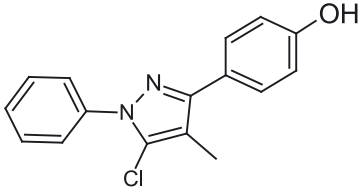
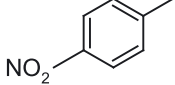
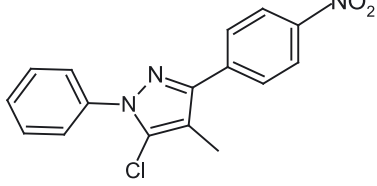
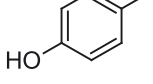
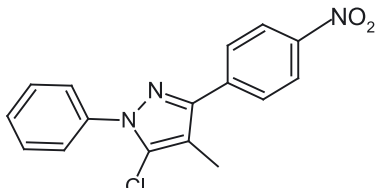
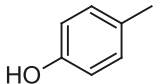


Scheme 1.

Table 1. Tested compounds

RHC=CHCOCH=CHR (1a-1e)			
Compound	R	R'	Compound name
1	2	3	4
1a		—	1,5-Diphenyl pent-1,4-diene-3-one
1b		—	1,9-Diphenylnon-1,3,6,8-tetraene-5-one
1c		—	1,5-bis(2-hydroxyphenyl)pent-1,4-diene-3-one

1	2	3	4
1d		–	1,5-Difurylpent-1,4-diene-3-one
1e		–	1,3-Bis(2-hydroxy,4-methoxyphenyl) prop-2-ene-1-one
RCH=CHCOR' (2a–2o)			
2a			1,3-di(phenyl)prop-2-ene-1-one
2b			1-furyl-3-phenylprop-2-ene-1-one
2c			1-phenyl, 3-(2-hydroxyphenyl) prop-2-ene-1-one
2d			1-phenyl-3(2-hydroxy-4-methoxy phenyl) prop-2-ene-1-one
2e			1-(4-hydroxyphenyl) 3-phenylprop-2-ene-1-one
2f			1-(4-hydroxyphenyl), 3-(2-hydroxyphenyl) prop-2-ene-1-one
2g			3-furyl-1-(4-hydroxyphenyl) prop-2-ene-1-one
2h			1-(2-hydroxyphenyl) 3-phenylprop-2-ene-1-one
2i			1,3 Bis -(2-hydroxyphenyl) prop-2-ene-1-one
2j			3-[5-chloro-3-(4-hydroxyphenyl)-1-phenyl-1-H-pyrazol-4-yl]-1-phenylprop-2-en-1-one

1	2	3	4
2k			3-[5-chloro-3-(4-hydroxyphenyl)-1-phenyl-1-H-pyrazol-4-yl]-1-(4-hydroxyphenyl)prop-2-en-1-one
2l			3-[5-chloro-3-(4-hydroxyphenyl)-1-phenyl-1-H-pyrazol-4-yl]-1-(4-chlorophenyl)prop-2-en-1-one
2m			3-[5-chloro-3-(4-hydroxyphenyl)-1-phenyl-1-H-pyrazol-4-yl]-1-(4-nitrophenyl)prop-2-en-1-one
2n			3-[5-chloro-3-(4-chlorophenyl)-1-phenyl-1-H-pyrazol-4-yl]-1-(4-hydroxyphenyl)prop-2-en-1-one
2o			3-[5-chloro-3-(4-nitrophenyl)-1-phenyl-1-H-pyrazol-4-yl]-1-(4-hydroxyphenyl)prop-2-en-1-one

Characterization

InfraRed Spectra were recorded on Perkin Elmer BX-II Spectrophotometer using KBr pellets. $^1\text{H-NMR}$ (CDCl_3) analysis was done with Model-Bruker ACP 300 and C H N analysis was done with Element analysensysteme GmbH VarioEL.

Insecticidal activity: determination of percentage of mortality

Preparation of test samples

A stock solution of each compound was prepared in acetone. The combination of bioactive compounds (1a, 2a, 2c, 2g) with natural products, neem oil (*A. indica*) (N1) which is available commercially in Ayurvedic medical stores without a prescription in India, and nicotinic acid (N2) purchased from CDH, 044069 were prepared in a 1:1 ratio.

Bioassay

The nucleus culture of *P. solenopsis* was sourced from the biological control laboratory, Division of Entomology, Indian Agricultural Research Institute (IARI), New Delhi. The mealy bugs were reared on sprouted potato tuber

at a temperature of $27\pm 2^\circ\text{C}$ with a relative humidity at $60\pm 5\%$ following the method described by Gautam 2008a.

Fresh pieces of sprouted potato tuber (2.5 cm x 2.5 cm) were taken in Petri plates. The desired dose of compounds (1000 ppm) dissolved in acetone, were sprayed on the tuber pieces and air dried to evaporate the acetone. Initially adults of *P. solenopsis* were treated, but no significant effect was observed on them as shown in figure 2 a and b, the treated females even laid young once. Henceforth, experiments were carried out on third instar larva nymphs.

With the help of a brush, a total of 10 third-instar nymphs were released on each healthy sprout of tuber piece for direct contact. Each treatment, including the control, was replicated 5 times. The insects used in the experiments were examined for mortality after 24, 48 and 72 hours of treatment while being viewed under binocular (LEICA EZ4-D), Division of Entomology, IARI, New Delhi. Percentage of Mortality was determined using the following formula:

Percentage of mortality = $\frac{\text{Total No. of Insects introduced} - \text{No. of insects alive after treatment}}{\text{Total No. of insects introduced}} \times 100$

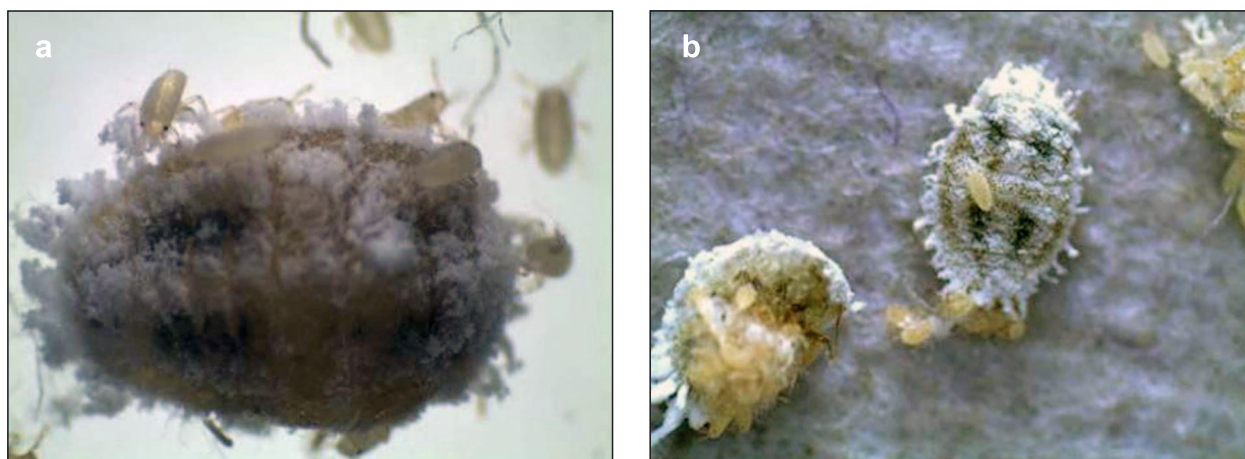


Fig. 2a, b. The adults remain unaffected after 72 hours of treatment of compounds

RESULTS

Characterization: compounds 2j-2o

The IR spectrum of all compounds showed characteristic bands at 2,900–3,100 and 1,610–1,570 cm^{-1} due to aromatic ring skeleton vibration. The shift in wave number from a normal range of >C=O band of 1,700 cm^{-1} to a range of 1,689–1,650 cm^{-1} , confirmed the presence of a conjugated carbonyl group. A band in the range of

2,900–3,100 cm^{-1} confirmed $-\text{CH}=\text{CH}-$ skeleton. Bands near 778 and 696 cm^{-1} signified the presence of monosubstituted benzene. The presence of $-\text{OH}$ group was confirmed by a band near 3,355 cm^{-1} and in 2m and 2o the band near 1,440 cm^{-1} corresponded to the nitro group. ^1H NMR and CHN results were found in accordance with their expected values (Table 2).

Table 2. Physical properties of compounds (2j–2o)

Compound	Melting point [°C]	Molecular formula	%C Observed (calculated)	%H Observed (calculated)	%N Observed (calculated)	Yield [%]	Rf
2j	116–118	$\text{C}_{24}\text{H}_{17}\text{ClN}_2\text{O}_2$	72.01 (71.91)	4.10 (4.27)	7.26 (6.99)	60	0.7
2k	160	$\text{C}_{24}\text{H}_{17}\text{ClN}_2\text{O}_3$	69.45 (69.15)	4.17 (4.11)	6.56 (6.72)	72	0.4
2l	110	$\text{C}_{24}\text{H}_{16}\text{Cl}_2\text{N}_2\text{O}_2$	66.18 (66.22)	3.77 (3.70)	6.35 (6.44)	69	0.9
2m	166	$\text{C}_{24}\text{H}_{16}\text{ClN}_3\text{O}_4$	65.32 (64.65)	3.65 (3.62)	9.35 (9.42)	73	0.9
2n	160	$\text{C}_{24}\text{H}_{16}\text{Cl}_2\text{N}_2\text{O}_2$	66.37 (66.22)	3.77 (3.70)	6.42 (6.44)	80	0.4
2o	200	$\text{C}_{24}\text{H}_{16}\text{ClN}_3\text{O}_4$	64.53 (64.65)	3.66 (3.62)	9.54 (9.42)	69	0.7

Insecticidal activity

The tested samples showed appreciable activity against third instar nymph of *P. solenopsis* (Fig. 3a and b). Insecticidal activity after 24, 48 and 72 hours of treatment of all the compounds and combinations on *P. solenopsis* are shown in table 3 and 4, respectively. After 24 h only four compounds 1c, 2g, 2l and 2o showed slight activity. After 48 h of treatment, activity of the aforesaid compounds had increased. Three more compounds 2c, 2j, 2k, also demonstrated mild activity.

After 72 h, the activity of compounds 2l and 2o became appreciable with 58 and 50% of mortality, respectively. Similarly the activities of 2c, 2g and 2j, also became

mentionable with the percentage of mortality in the range of 34–38%.

The natural products N1 and N2 showed 36 and 38% of mortality, respectively, when tested alone (Table 4). Among all combinations of N1 with compounds exhibiting insecticidal activity when tested alone (1a–1e; 2a–2i), a good synergistic influence was observed. Moderately active 1c and 2a (Fig. 4a, b), increased their activity almost 1.5 times. An increase in activity of 2g from 34 to 44% was also observed due to the presence of N1. Similarly, the insecticidal activity of 2a and 2g was increased almost 1.5 times by N2 (Fig. 4b, c).

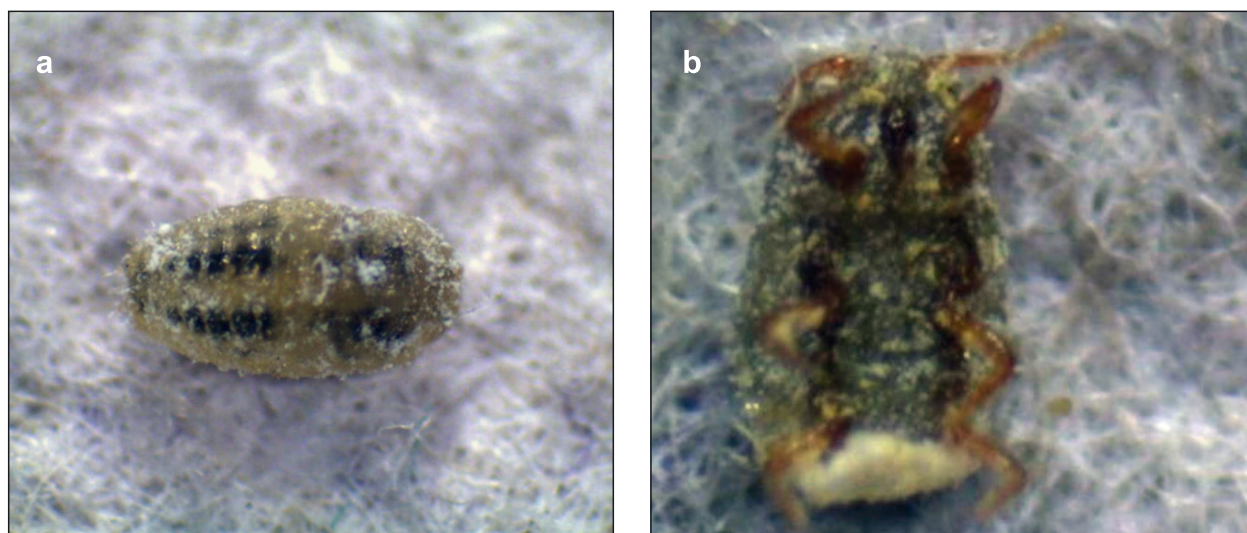


Fig. 3a and b. Effect of treatments on third instar nymph after 72 hours

Table 3. Insecticidal activity of synthetic compounds in terms of percentage of mortality

No.	Treatments	Percentage of mortality [%]			
		first observation (after 24 h)	second observation (after 48 h)	third observation (after 72 h)	total
1	1a	0.	0	0	0 \pm 0
2	1b	0	0	0	0 \pm 0
3	1c	10	10	10	30 \pm 4.082
4	1d	0	0	0	0 \pm 0
5	1e	0	0	0	0 \pm 0
6	2a	0	0	28	28 \pm 2.581
7	2b	0	0	0	0 \pm 0
8	2c	0	20	18	38 \pm 2.581
9	2d	0	0	0	0 \pm 0
10	2e	0	0	0	0 \pm 0
11	2f	0	0	0	0 \pm 0
12	2g	14	6	14	34 \pm 3.158
13	2h	0	0	0	0 \pm 0
14	2i	0	0	0	0 \pm 0
15	2j	0	20	14	34 \pm 3.158
16	2k	0	14	12	26 \pm 2.581
17	2l	18	14	26	58 \pm 2.581
18	2m	0	0	0	0 \pm 0
19	2n	0	0	0	0 \pm 0
20	2o	12	16	22	50 \pm 0

SEm \pm 0.892, CD (0.01%) is 3.32

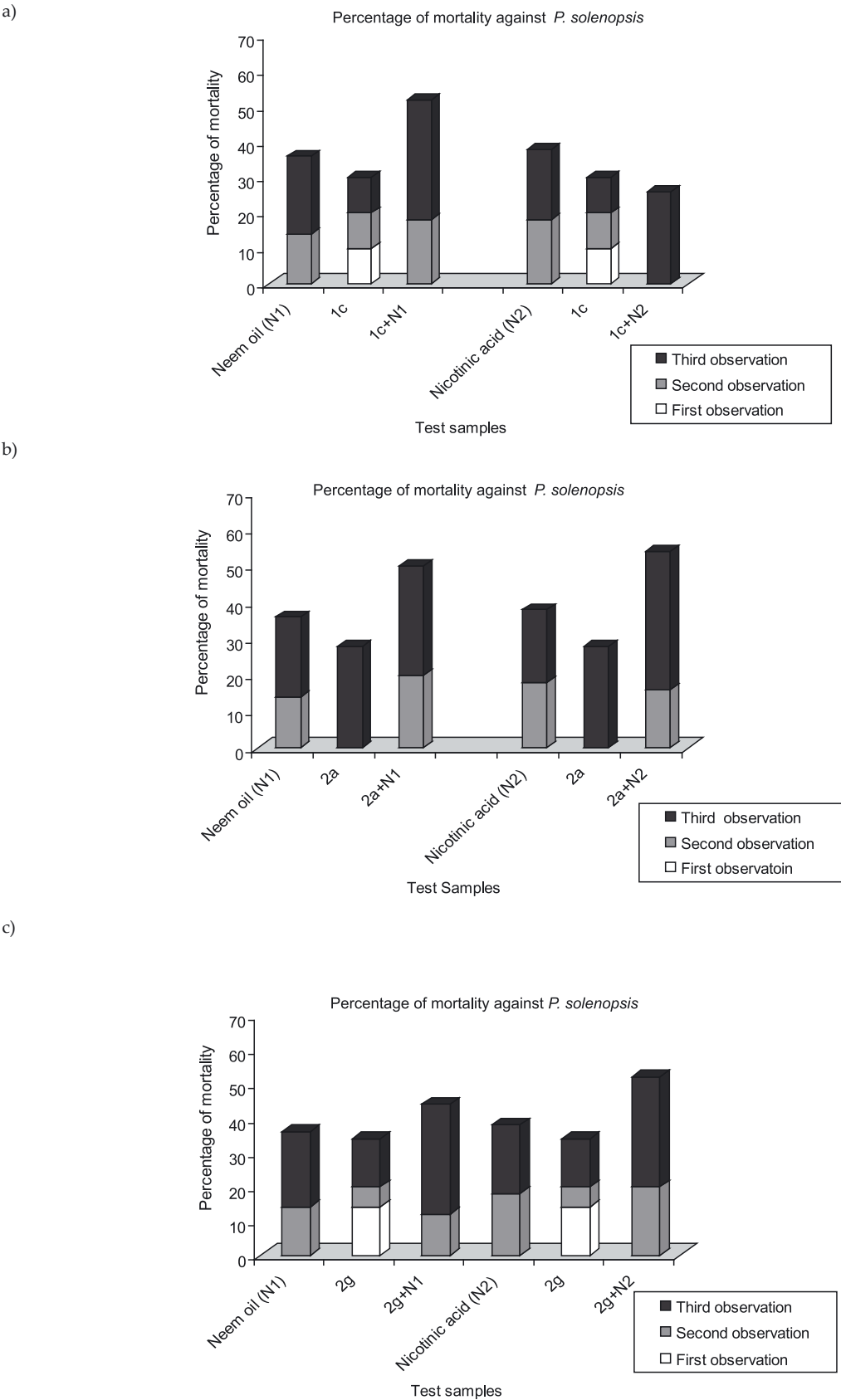


Fig. 4a, c. Graphs representing the percentage of mortality of compounds in combination with natural products

Table 4. Insecticidal activity of natural products and their combinations with bioactive compounds in terms of percentage of mortality

No.	Treatments	Percentage of mortality (%)			
		first observation (after 24 h)	second observation (after 48 h)	third observation (after 72 h)	total
1	neem oil (N1)	0	14	22	36 \pm 3.158
2	nicotinic acid (N2)	0	18	20	38 \pm 2.581
3	1c-N1	0	18	34	52 \pm 2.581
4	2a-N1	0	20	30	50 \pm 0
5	2c-N1	0	0	20	20 \pm 0
6	2g-N1	0	12	32	44 \pm 3.158
7	1c-N2	0	0	26	26 \pm 3.158
8	2a-N2	0	16	38	54 \pm 3.158
9	2c-N2	0	0	10	10 \pm 0
10	2g-N2	0	20	32	52 \pm 2.581

SEm \pm 1.15, CD (0.01%) is 4.42

DISCUSSION

Solanum mealy bug is an emerging pest problem and its host-range is expanding day by day (Gautam 2008b). It has the potential for spreading aggressively and causing devastating effects on crops. This may results in a reluctance on the part of farmers to grow certain crops like cotton and eggplant which are the preferred food plants for SMB. After the realization of adverse effects on the environment and humans associated with the use of conventional pesticides, the current binary approach was undertaken to explore a new path for the control of SMB. This new direction investigates the insecticidal potential of compounds. Such an approach is designed to incorporate well known bioactive structures, *viz.*, chalcones and pyrazole, in a single molecule, and insecticidal screening of a combination of synthetic compounds and natural products, known for their various biological activities.

Among various newly designed compounds, (2j–2o) 2l and 2o have shown considerable activity against the mealy bug. A reasonable structure relative interpretation

can be extracted by the fact that presence of an hydroxyl group at para position of benzene ring C (Fig. 5) and chloro group at para position of ring A, play an important role in the development of the activity in compound 2l, because removal or substitution of the chloro group with the hydroxy group diminishes the insecticidal activity (2j and 2k). Even swapping the chloro and the hydroxyl group completely inhibits the insecticidal activity of the resulting (Fig. 5) compound (2n). On the other hand, a reverse effect was observed with nitro and hydroxyl groups at these positions. In inactive compound 2m, the hydroxyl group is present at para position of ring C and nitro group at ring A, while in the active compound 2o, the hydroxyl group is at A ring and nitro group is at C ring. All these findings provide an insight for the designing of new and effective insecticides.

Our previous studies have established the promising antimicrobial activity of α,β -unsaturated carbonyl compounds in combination with natural products, neem oil and nicotinic acid (Rani *et al.* 2009a; Rani *et al.* 2009b). The next step was to explore the insecticidal efficacy of these

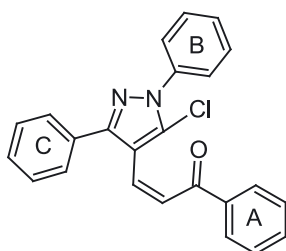


Fig. 5. Basic nucleus of compounds (2j–2o), representing the ring A, B, C



Fig. 6. Potato tuber after a 72 hour 2a test compound treatment

products. Good results were obtained – both of the natural products have shown good synergistic effect on insecticidal activity of 2a. Moreover, the insecticidal activity of combinations of mildly active synthetic compounds and natural products (2a-N1 and 2a-N2) was comparable to the activity of newly synthesized multi-structure containing compounds (2j–2o). It is worth mentioning, that compound 2a may be considered as ecologically safe as it can be synthesized by a simple and straightforward reaction without using harmful chemicals as solvent or catalyst. Compound 2a showed no toxicity on the plant substrate; the potato tuber remained green and healthy even after 72 h of treatment with the compound (Fig. 6). Also, the in vitro cell cytotoxicity of compounds with significant insecticidal activity, in combination, was investigated using the haemolytic assay (Bisht *et al.* 2007). The compounds exhibited negligible toxicity (7–14%) even up to high experimental concentrations *i.e.* 1000 ppm (Fig. 7) (Rani *et al.* 2010).

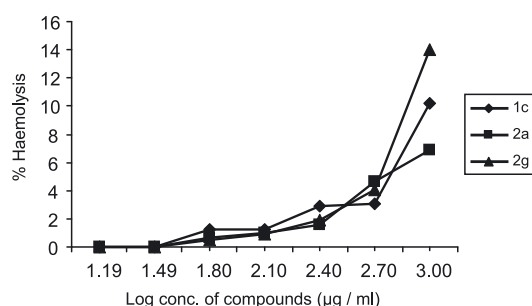


Fig. 7. Haemolytic activities of tested bioactive compounds

Based on such finding we may conclude that limited use of simple and safer chemicals in combination with natural products, is a greener and effective mode of control of noxious pests like *P. solenopsis*. This is the first study of this kind that can lead us towards the development of a new class of environmentally benign insecticides.

ACKNOWLEDGMENTS

The authors are grateful to Delhi Technological University (Formerly Delhi College of Engineering), Delhi for providing the facilities used during the studies. We are also grateful to Mrs. Usha Saxena for her helpfulness with the insecticidal activity parts of the experiment. S.J. is also grateful to the University Grant Commission for financial support.

REFERENCES

- Akintola J., Ande A.T. 2008. First record of *Phenococcus solenopsis* Tinsley (Hemiptera: Pseudococcidae) on *Hibiscus roosinensis* in Nigeria. *Agric. J.* 3 (1): 1–3.
- Akbas E., Berber I. 2005. Antibacterial and antifungal activities of new pyrazolo[3,4-*d*] pyridazin derivatives. *Eur. J. Med. Chem.* 40: 401–405.
- Anto R.J., Sukumaran K., Kuttan G., Rao M.N.A., Subaraju V., Kuttan R. 1995. Anticancer and antioxidant activity of synthetic chalcones and related compounds. *Cancer Lett.* 97 (1) 33–37.
- Arty I.S., Timmerman H., Samhoedi M., Sastrohamidjojo D., Sugiyanto, Goot H. Van Der 2000. Synthesis of benzylideneacetophenones and their inhibition of lipid peroxidation. *Eur. J. Med. Chem.* 35 (4): 449–457.
- Bhat B.A., Dhar K.L., Puri S.C., Saxenam A.K., Shanmugavel M., Qazi G.N. 2005. Synthesis and biological evaluation of chalcones and their derived pyrazoles as potential cytotoxic agents. *Bioorg. Med. Chem. Lett.* 15 (12): 3177–3180.
- Bisht G.S., Rawat D.S., Kumar A., Kumar R., Pasha S. 2007. Antimicrobial activity of rationally designed amino terminal modified peptides. *Bioorg. Med. Chem. Lett.* 17: 4343–4346.
- Bodor E.T., Offermanns S. 2008. Nicotinic acid: an old drug with a promising future. *Br. J. Pharmacol.* 153: 68–75.
- Boumendjel A., Boccard J., Carrupt P.A., Nicolle E., Blanc M., Geze A., Choisnard L., Wouessidjewe D., Matera E.L., Dumontet C. 2008. Antimitotic and antiproliferative activities of chalcones: forward structure-activity relationship. *J. Med. Chem.* 51 (7): 2307–2310.
- Chen S.P., Chen C.N., Wong C.Y. 2002. New record of a pest – *Phenacoccus solani* Ferris (Homoptera: Pseudococcidae) in Taiwan. *J. Agri. Res. China* 51 (2): 79–82.
- Devkumar C., Sukhdev 1993. *Neem Research and Development* (N.S. Radhwa, B.S. Parmar, eds.). Society of Pesticide Science New Delhi: 63–96.
- Dimmock J.R., Elias D.W., Beazely M.A., Kandepu N.M. 1999. Bioactivities of chalcones. *Curr. Med. Chem.* 6 (12): 1125–1150.
- Dominguez J.N., Leon C., Rodrigues J., Gamboa de Dominguez N., Gut J, Rosenthal P.J. 2005. Synthesis and antimalarial activity of sulfonamide chalcone derivatives. *Farmaco* 60 (4): 307–311.
- Ben-Dov Y. 2005. The *Solanum* mealybug, *Phenacoccus solani* Ferris (Hemiptera: Coccoidea: Pseudococcidae), extends its distribution range in the Mediterranean Basin. *Phytoparasitica* 33 (1): 15–16.
- Gautam R.D. 2008a. *Biological Pest Suppression*. Westville Publishing House Delhi, 304 pp.
- Gautam R.D. 2008b. *Solanum* mealy bug, *Phenacoccus solani* – an emerging threat to Indian agri-horticultural production and trade: management strategies. *Indian J. Appl. Entomol.* 22 (1): 1–7.
- Gautam R.D., Saxena U., Gautam S., Khan M.A., Gautam C.P.N. 2007. Studies on *Solanum* mealy bug, *Phenacoccus solani* Ferris (Hemiptera: Pseudococcidae), its parasitoid and predator complex, reproductive potential and utilization as laboratory prey for rearing the ladybird and green lacewing predators. *J. Entomol. Res.* 31 (3): 259–264.
- Gupta H., Bhandari D., Dua K., Sharma V.K., Sara U.V.S. 2008. Neem: a natural boon. *Pharmaceu. Rev. (E-Journal)* 6 (5).
- Jermy T. 1990. Prospects of antifeedant approach to pest control – a critical review. *J. Chem. Ecol.* 16 (11): 3151–3161.
- Lahtchev K.L., Batovska D.I., Parushev S.P., Ubiyovk V.M., Si-birny A.A. 2008. Antifungal activity of chalcones: A mechanistic study using various yeast strains. *Eur. J. Med. Chem.* 43 (10): 222–2228.
- Liu X.H., Cui P., Song B.A., Bhadury P.S., Zhu H.L., Wang S.F. 2008. Synthesis, structure and antibacterial activity of novel 1-(5-substituted-3-substituted-4,5-dihydropyrazol-1-yl)

- ethanone oxime ester derivatives. *Bioorg. Med. Chem.* 16: 4075–4082.
- Gupta M., Paul S., Gupta R. 2009. Microwave assisted one pot synthesis of antifungal active 1-substituted-3,7-dialkyl/aryl-4H-pyrazolo[4,5-f]-[1,2,4]triazolo[3,4-b]thiadiazepines using solid support. *Indian J. Chem.* 48 (B) March: 460–66.
- Furniss B.S., Hannaford A.J., Smith P.W.G., Tatchell A.R. 2005. *Vogel's Textbook of Practical Organic Chemistry*. 5th ed. Pearson Education: 1034–1035.
- Nalwar Y.S., Sayyed M.A., Mokle S.S., Zangwar P.R., Vibhute Y.B. 2009. Synthesis and insect antifeedant activity of some new chalcones against *Phenacoccus solanopsis*. *World J. Chem.* 4 (2): 123–126.
- Rani A., Jain S. 2008. Studies on *Enterococcus faecium* growth – inhibitory action of 1,5-bis(2-hydroxyphenyl)pent-1,4-diene-3-one and related compounds: a search for environmentally benign anti-bacterial agent. *Rasayan J. Chem.* 1 (4): 795–801.
- Rani A., Jain S., Dureja P. 2009a. Synergistic fungicidal efficacy of formulations of neem oil, nicotinic acid and *Ferula asafoetida* with α,β -unsaturated carbonyl compounds against *Sclerotium rolfsii* ITCC 5226 & *Macrophomina phaseolina* ITCC 0482. *J. Pestic. Sci.* 34 (4): 253–258.
- Rani A., Jain S., Dureja P., Kumar R., Kumar A. 2009b. Synergistic interaction between synthetic and natural products: a promising tool for the development of environmentally safe potent antimicrobial agents. *World Appl. Sci. J.* 5 (Special issue): 59–63.
- Rani A., Jain S., Kumar R., Kumar A. 2010. 1, 5-bis (2-hydroxyphenyl)pent-1,4-diene-3-one : a lead compound for the development of broad spectrum antibacterial agent. *South Afr. J. Chem.* 63: 31–35.
- Santa-Cecilia L.V.C., Reis P.R., Souza J.C. 2002. About the nomenclature of coffee mealybug species in Minas Gerais and Espírito Santo States, Brazil. *Neotrop. Entomol.* 31: 333–334.
- Shiga Y., Okada I., Ikeda Y., Takizawa E., Fukuchi T. 2003. Insecticidal Activity of *N*-Acyl-*N*-(4-aryloxybenzyl)pyrazole-5-carboxamides. *J. Pest. Sci.* 28: 313–314.
- Sivakumar P.M., Seenivasan S.P., Kumar V., Doble M. 2007. Synthesis, antimycobacterial activity evaluation, and QSAR studies of chalcone derivatives. *Bioorg. Med. Chem. Lett.* 17 (6): 1695–1700.

Power-Law Expansion and Scalar Field Cosmology in Higher Derivative Theory

C.P. Singh · Vijay Singh

Received: 17 October 2011 / Accepted: 26 December 2011
© Springer Science+Business Media, LLC 2012

Abstract In this paper we study the evolution of a flat Friedmann-Robertson-Walker model filled with a perfect fluid and a scalar field minimally coupled to gravity in higher derivative theory of gravitation. Exact solution of the field equations are obtained by the assumption of power-law form of the scale factor. A number of evolutionary phases of the universe including the present accelerating phase are found to exist with scalar field in the higher derivative theory of gravitation. The properties of scalar field and other physical parameters are discussed in detail. We find that the equation of state parameter for matter and scalar field are same at late time in each case. We observe that a higher derivative term can hardly be a candidate to describe the presently observed accelerated expansion. It is only the hypothetical fluids, which provide the late time acceleration. It is also remarkable that the higher derivative theory does not effect the radiating model of scalar field cosmology.

Keywords Cosmology · Power-law expansion · Scalar field · Higher derivative theory of gravity

1 Introduction

The observations related to supernova, cosmic microwave background (CMB) and galaxy clustering [1–3] indicate that the present universe is passing through a phase of the cosmic acceleration. It is also believed that the universe might have emerged from an inflationary phase in the past. A large number of cosmological models were proposed in Einstein's gravity with early inflationary scenario in the last three decades. However, the recent prediction that the present universe is passing through an accelerated phase of expansion, is interesting. This unexpected discovery of the accelerated expansion of the universe has opened one

C.P. Singh (✉) · V. Singh
Department of Applied Mathematics, Delhi Technological University (Formerly Delhi College of Engineering), Bawana Road, Delhi 110 042, India
e-mail: cpsphd@rediffmail.com

V. Singh
e-mail: gtrcosmo@gmail.com

of the most puzzling and deepest problems in cosmology today. The acceleration of the universe can be accounted for either modifying the gravity of Einstein equations or supplementing the energy momentum tensor by an exotic matter with negative pressure, popularly known as dark energy.

In the past few years a number of different alternative theories have been proposed to explain the cosmological problems of the universe [4–7]. The intension of introducing modified gravity models is that one may obtain a gravitational alternative to the conventional description of dark energy. Therefore, there is a resurgence of interest in such modified theories of gravitation.

One of the early attempts to modify Einstein gravitation theory known as higher derivative (HD) theory, is based on adding a scalar curvature term- (R^2) in the Einstein-Hilbert action. With an additional term- R^2 in modified gravity $(R + \alpha R^2)$, where α is constant, the higher derivative theory was introduced to obtain early inflation [8]. The structure and properties of the HD theory were further elaborated in subsequent works [9–12]. Starobinsky [13] studied the cosmological models in HD theory and found that this theory admits inflation in Einstein-Hilbert action. The work of Starobinsky came prior to the similar work on inflation proposed by Guth [14]. Cosmological inflation has become an integral part of the standard model of the universe. Apart from being capable of removing the shortcomings of the standard cosmology, inflation gives important clues for the structure formation of the universe. It is known that higher order gravity with suitable counter terms viz., $C^{\mu\nu\rho\delta}C_{\mu\nu\rho\delta}$, R^2 , and cosmological constant Λ added to the Einstein-Hilbert action, one gets a perturbation theory which is well behaved, formally renormalizable and asymptotically free [15].

The dynamics of the evolution of the universe are related to the scalar field cosmology. It is a common issue in cosmology to make use of scalar fields ϕ as the responsible agents of some of the most intriguing aspects of our universe [16]. Scalar fields are used as the inflation which seeds the primordial perturbations for the structure formation during an early inflationary epoch; as the cold dark matter, candidate responsible for the formation of the actual cosmological structure and as the dark energy component, which seems to be draining the current accelerated expansion of the universe. The cosmological models based on scalar fields have a long history, being used for exploration of possible inflationary scenario and for description of dark energy. In recent years cosmological model with a scalar field is a most natural basis for the inflationary model. Scalar fields provide the existence of the effective cosmological constant at the early stages of the cosmic evolution.

Cosmological models with perfect fluid as a source matter in HD theory have been studied by several authors [17–28] in order to obtain viable cosmological scenario of the early universe. However, in the early universe a number of processes might have occurred leading to a deviation from perfect fluid assumption, e.g., scalar field which is to be taken into account. Most of the studies have been come out with a minimally coupled scalar field representing quintessence. Ellis and Madsen [29] have considered perfect fluid Friedmann-Robertson-Walker (FRW) models with a minimally coupled scalar field and non-zero scalar potential. Barrow and Saich [30], Barrow and Mimoso [31], Mimoso and Wands [32], and Banerjee and Sen [33] have studied the scalar field models with perfect fluid in general relativity. Paul [34] has considered the cosmological model with scalar field in HD theory for power-law and exponential expansions of the universe. Recently, Singh et al. [35] have studied FRW model filled with viscous fluid and zero rest-mass scalar-field in HD theory.

Therefore, it is reasonable to explore higher derivative theory with scalar field and perfect fluid, which could explain an inflationary scenario of the early universe and accelerating phase of the universe at late time followed by a matter-dominated phase. A number of evolutionary phases of the universe including the present accelerating phase are found to exist

with scalar field in the higher derivative theory of gravitation. The properties of scalar field and other physical parameters are discussed in detail. Therefore, the motivation of this paper is to observe the effect of HD theory in different phases of the universe with a two matter component system. We would like to see whether the HD theory is responsible for the accelerated expansion of the universe at late time.

This work is organized as follows: The dynamics we consider here are governed by HD theory, thus the non-minimal gravitational action and the model are presented in Sect. 2, followed by a general solution of field equations in Sect. 3. We discuss the decelerated and accelerated phases of the universe with an equation of state for barotropic fluid in Sects. 3.1–3.4. Finally, the conclusion is presented in Sect. 4.

2 Higher Derivative Theory and Friedmann Equations

The gravitational action for a higher derivative theory of gravity with a scalar field ϕ , minimally coupled to gravity and matter fluid in the units $8\pi G = 1$ and $c = 1$, takes the following form [22, 23]

$$I = - \int \left[\frac{1}{2} (R + \alpha R^2) + L_m + \frac{1}{2} \phi_{,\mu} \phi^{,\mu} + V(\phi) \right] \sqrt{-g} d^4x, \quad (1)$$

where R is the scalar curvature, α is a constant, $V(\phi)$ is the scalar potential L_m is the Lagrangian density of matter which is assumed to be a barotropic fluid and g is the metric determinant. We see that the standard Einstein-Hilbert action is recovered by taking $\alpha = 0$.

We assume that the metric tensor $g_{\mu\nu}$ is the only independent variable and the variation of action (1) with respect to $g_{\mu\nu}$, gives the following set of field equations

$$R_{\mu\nu} - \frac{1}{2} g_{\mu\nu} R + \alpha \left[2R \left(R_{\mu\nu} - \frac{1}{4} g_{\mu\nu} R \right) + 2(R_{;\mu\nu} - g_{\mu\nu} \square R) \right] = -T_{\mu\nu}, \quad (2)$$

where a semi-colon represents the covariant derivative, \square is the covariant differential operator and $T_{\mu\nu}$ is the energy momentum tensor of a barotropic perfect fluid and a non-interacting scalar field with scalar potential. Thus, the energy momentum tensor, $T_{\mu\nu}$ is given by

$$T_{\mu\nu} = T_{\mu\nu}^{(m)} + T_{\mu\nu}^{(\phi)}. \quad (3)$$

The energy momentum tensor for a perfect fluid source is given by

$$T_{\mu\nu}^{(m)} = (\rho_m + p_m) u_\mu u_\nu + p_m g_{\mu\nu}, \quad (4)$$

where ρ_m is the energy density and p_m is the thermodynamic pressure of the fluid. u_μ is the four velocity of the fluid such that $u_\mu u^\mu = -1$, and in co-moving coordinates, one can choose $u^\mu = \delta_0^\mu$.

The energy momentum tensor for a minimally coupled scalar field ϕ , with self interacting potential $V(\phi)$, which follows (1) has the form

$$T_{\mu\nu}^{(\phi)} = \phi_{,\mu} \phi_{,\nu} - g_{\mu\nu} \left[\frac{1}{2} \phi_{,\sigma} \phi^{,\sigma} + V(\phi) \right]. \quad (5)$$

We assume that the barotropic fluid and scalar field are non-interacting, we have the following separate energy conservation laws:

$$T_{;\nu}^{\mu\nu(m)} = 0 = T_{;\nu}^{\mu\nu(\phi)}. \quad (6)$$

We consider a spatially homogeneous and isotropic flat Friedmann-Robertson-Walker metric for the universe as

$$ds^2 = -dt^2 + a^2(t)[dr^2 + r^2(d\theta^2 + \sin^2\theta d\phi^2)], \quad (7)$$

where $a(t)$ is the scale factor of the universe.

The scalar curvature for the metric (7) is

$$R = -6[\dot{H} + 2H^2], \quad (8)$$

where $H = \dot{a}/a$ is the Hubble parameter and an overdot denotes derivative with respect to the cosmic time t .

For the energy momentum tensor (3) and line element (7), the Friedmann equations in higher derivative theory (2) can be written as

$$3H^2 - 18\alpha[2\ddot{H}H - \dot{H}^2 + 6\dot{H}H^2] = \rho_m + \rho_\phi, \quad (9)$$

$$2\dot{H} + 3H^2 - 6\alpha[2\ddot{H} + 12\ddot{H}H + 18\dot{H}H^2 + 9\dot{H}^2] = -(p_m + p_\phi). \quad (10)$$

where ρ_ϕ and p_ϕ are respectively the energy density and pressure of the scalar field, which are given by

$$\rho_\phi = \frac{1}{2}\dot{\phi}^2 + V(\phi), \quad (11)$$

$$p_\phi = \frac{1}{2}\dot{\phi}^2 - V(\phi). \quad (12)$$

The evolution equation of the scalar field, describing its energy conservation as the universe expands, is

$$\dot{\rho}_\phi + 3H(\rho_\phi + p_\phi) = 0, \quad (13)$$

or written equivalently as

$$\ddot{\phi} + 3H\dot{\phi} + \frac{\partial V}{\partial \phi} = 0. \quad (14)$$

Finally, the equations closed by considering the evolution of the matter density

$$\dot{\rho}_m + 3H(\rho_m + p_m) = 0. \quad (15)$$

3 Solution of the Field Equations

As we see the field equations are highly non-linear. Therefore, in order to solve the field equations we consider the power-law expansion of the universe

$$a = a_0 \left(\frac{t}{t_0} \right)^n, \quad (16)$$

which is physically interesting since it gives rise to a constant deceleration parameter $q = -\frac{a\ddot{a}}{\dot{a}^2} = -1 + \frac{1}{n}$ with $0 < n < 1$ for an expanding universe and $n > 1$ for accelerated

expansion. Here a_0 and t_0 are the present values of a and t respectively and n is a positive constant, which determines the expansion during the different phases of the evolution of the universe.

The Hubble parameter is given by

$$H = \frac{n}{t}. \quad (17)$$

With (17) in (8) it becomes obvious that $R \propto t^{-2}$, consequently, $R^2 \propto t^{-4}$. We assume that the pressure and energy density are related by an equation of state

$$p_m = \omega \rho_m, \quad (18)$$

where ω is a constant known as the equation of state parameter and its value lies in the interval $-1/3 \leq \omega \leq 1$.

Using (17) and (18), (15) integrates to the form

$$\rho_m = \rho_{m0} t^{-3n(1+\omega)}, \quad (19)$$

where $\rho_{m0} = A(t_0^n/a_0)^{3(1+\omega)}$. Here A is a constant of integration. For energy density to be positive we must have $\rho_{m0} > 0$, i.e., $A > 0$.

Now, (9) can be rewritten as

$$\rho_\phi = 3H^2 - 18\alpha[2H\ddot{H} - \dot{H}^2 + 6\dot{H}H^2] - \rho_m. \quad (20)$$

Using (17) and (19), (20) gives

$$\rho_\phi = \frac{3n^2}{t^2} - \frac{\rho_{m0}}{t^{3n(1+\omega)}} + \frac{54\alpha n^2(2n-1)}{t^4}. \quad (21)$$

Also, (14) can be rewritten as

$$-3H\dot{\phi}^2 = \frac{d\rho_\phi}{dt}, \quad (22)$$

which gives

$$\dot{\phi}^2 = -\frac{1}{3H} \frac{d\rho_\phi}{dt}. \quad (23)$$

Using (17) and (21) into (23), the kinetic term in terms of t can be obtained as

$$\dot{\phi}^2 = \frac{2n}{t^2} - \frac{(1+\omega)\rho_{m0}}{t^{3n(1+\omega)}} + \frac{72\alpha n(2n-1)}{t^4}. \quad (24)$$

The scalar potential is given by

$$V(t) = \frac{n(3n-1)}{t^2} + \frac{(\omega-1)\rho_{m0}}{2t^{3n(1+\omega)}} + \frac{18\alpha n(2n-1)(3n-2)}{t^4}. \quad (25)$$

We observe that kinetic term and scalar potential have the term of $1/t^4$ due to the higher derivative gravity. The Einstein's solutions may be recovered for $n = 1/2$ and $\alpha = 0$. Equation (25) represents the scalar potential as a function of time t . Integration of (24) gives the scalar field as a function of time. Inverting this dependence we can obtain the time parameter

as a function of ϕ and substituting the corresponding formula into (25), one arrives to the uniquely reconstructed potential $V(\phi)$.

As $\dot{\phi}^2$ can not be negative, one has the condition

$$\frac{2n}{t^2} - \frac{(1+\omega)\rho_{m0}}{t^{2n(1+\omega)}} + \frac{72\alpha n(2n-1)}{t^4} \geq 0, \quad (26)$$

for the model to be consistent.

Finally, the time-dependent of the scalar field pressure can be extracted from (12), using (24) and (25), as

$$p_\phi = \frac{n(2-3n)}{t^2} + \frac{18\alpha n(2n-1)(4-3n)}{t^4} - \frac{\omega\rho_{m0}}{t^{3n(1+\omega)}}. \quad (27)$$

Thus, we can straight forward extract the time evolution of the scalar field equation of state (EoS) parameter as

$$\omega_\phi = \frac{p_\phi}{\rho_\phi} = \frac{\frac{n(2-3n)}{t^2} + \frac{18\alpha n(2n-1)(4-3n)}{t^4} - \frac{\omega\rho_{m0}}{t^{3n(1+\omega)}}}{\frac{3n^2}{t^2} - \frac{\rho_{m0}}{t^{3n(1+\omega)}} + \frac{54\alpha n^2(2n-1)}{t^4}}. \quad (28)$$

It is very difficult to integrate (24) for $\phi(t)$, in general. Therefore, it is reasonable to explore the above solutions with equation of state parameter ω for matter and powers n .

3.1 Solution with $\omega = -1/3$ and $n = 1$

In this case, we get $p_m = -\rho_m/3$, which is the inflationary phase. The scale factor varies as a linear inflation, i.e., $a \sim t$ (marginal inflation). The energy density varies as inverse of square of cosmic time t , i.e., $\rho_m \sim 1/t^2$. The deceleration parameter has the value $q = 0$, which shows the ‘coasting cosmology’, i.e., the universe inflates with marginal inflation.

In this phase, (24) gives

$$\dot{\phi}^2(t) = \left(2 - \frac{2\rho_{m0}}{3}\right) \frac{1}{t^2} + \frac{72\alpha}{t^4} \quad (\rho_{m0} \leq 3) \quad (29)$$

which, on integration, we get

$$\phi(t) - \phi_0 = \sqrt{B} \left[\log \left\{ 2Bt \left(1 + \sqrt{1 + \frac{72\alpha}{Bt^2}} \right) \right\} - \sqrt{1 + \frac{72\alpha}{Bt^2}} \right], \quad (30)$$

where ϕ_0 is a constant of integration and $B = (6 - 2\rho_{m0})/3$. We consider here and thereafter only positive sign without loss of generality.

From (25), the scalar potential is given by

$$V(t) = \left(2 - \frac{2\rho_{m0}}{3}\right) \frac{1}{t^2} + \frac{18\alpha}{t^4} \quad (31)$$

The kinetic term $\dot{\phi}^2(t)$ and potential function $V(t)$ decrease from large values to zero during the evolution of the universe.

Equations (21) and (27) give the scalar field energy density and pressure as

$$\rho_\phi = \frac{(3 - \rho_{m0})}{t^2} + \frac{54\alpha}{t^4}, \quad (32)$$

$$p_\phi = -\frac{1}{3} \left(\frac{3 - \rho_{m0}}{t^2} \right) + \frac{18\alpha}{t^4}. \quad (33)$$

In this case, the EoS parameters of scalar field is given by

$$\omega_\phi = \frac{-\frac{1}{3} \left(\frac{3 - \rho_{m0}}{t^2} \right) + \frac{18\alpha}{t^4}}{\frac{(3 - \rho_{m0})}{t^2} + \frac{54\alpha}{t^4}}, \quad (34)$$

From (32) and (33), we observe that both the physical quantities ρ_ϕ and p_ϕ decrease with time. When $t \rightarrow 0$, we have $\omega_\phi = 1/3$. Therefore, the EoS of scalar field is $p_\phi = (1/3)\rho_\phi$ and as $t \rightarrow \infty$, we get $\omega_\phi = -1/3$. Therefore, we find that $\omega = \omega_\phi$ at late time expansion.

3.2 Solution with $\omega = 1/3$ and $n = 1/2$

In this case one gets $p_m = \rho_m/3$, which is the usual EoS for radiation-dominated phase. The deceleration parameter is $q = 1$ and hence the universe expands with decelerated rate. The scale factor varies as $a \sim t^{1/2}$, which is a power-law expansion. The behavior of matter energy density is similar to the inflationary phase and varies as $\rho_m \sim 1/t^2$.

In this case, (24) becomes

$$\dot{\phi}^2(t) = \left(1 - \frac{4\rho_{m0}}{3} \right) \frac{1}{t^2} \quad \left(\rho_{m0} < \frac{3}{4} \right), \quad (35)$$

which on integration, we get

$$\phi(t) - \phi_1 = \sqrt{1 - \frac{4\rho_{m0}}{3}} \log t. \quad (36)$$

where ϕ_1 is a constant of integration. The scalar potential has the form

$$V(t) = \left(\frac{3 - 4\rho_{m0}}{12} \right) \frac{1}{t^2}, \quad (37)$$

It is observed from (36) and (37) that both the scalar field and scalar potential are independent of higher derivative term, hence it is evident that the higher derivative theory does not effect the behavior of the cosmological model in radiation-dominated phase. Therefore, the cosmological evolution is same as obtained for a radiation-dominated phase in Einstein gravity which we get even if $\alpha \neq 0$ in HD theory since all the corrections due to the α terms are zero identically.

Inverting (36), we find

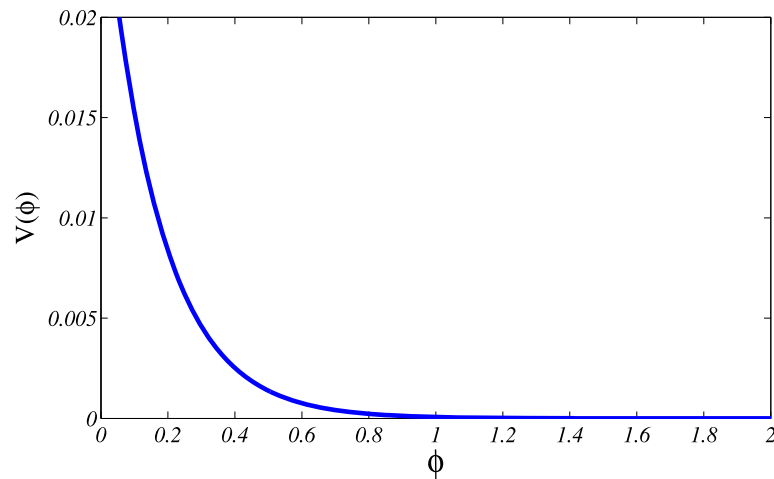
$$t(\phi) = \exp \left[\frac{1}{\sqrt{1 - \frac{4\rho_{m0}}{3}}} (\phi(t) - \phi_1) \right]. \quad (38)$$

Hence, (37) becomes

$$V(\phi) = \frac{(3 - 4\rho_{m0})}{12} \exp \left[-2 \sqrt{\frac{3}{3 - 4\rho_{m0}}} (\phi(t) - \phi_1) \right]. \quad (39)$$

The above equation shows that the scalar potential decreases exponentially with scalar field as shown in Fig. 1.

Fig. 1 Scalar potential $V(\phi)$ versus scalar field ϕ with $\phi_1 = 0$, and $\rho_{m0} = 2/3$



From (21) and (27), the scalar field density and pressure are respectively given by

$$\rho_\phi = \left(\frac{3}{4} - \rho_{m0} \right) \frac{1}{t^2}, \quad (40)$$

$$p_\phi = \frac{1}{3} \left(\frac{3}{4} - \rho_{m0} \right) \frac{1}{t^2}. \quad (41)$$

Thus, the scalar field and perfect fluid have the similar behavior during the decelerated phase of the radiating era. We find that scalar field and matter EoS parameters have the same constant value, viz., $\omega_\phi = \omega = 1/3$ at all times during the radiation phase. The universe decelerates throughout the evolution during radiation-dominated phase even if $\alpha \neq 0$ of HD theory.

3.3 Solution with $\omega = 0$ and $n = 2/3$

For these values of ω and n , we get $p_m = 0$, i.e., matter-dominated phase. The scale factor and matter energy density vary as $a \sim t^{2/3}$ and $\rho_m \sim 1/t^2$, respectively. The deceleration parameter has the value $q = 0.5$ and hence the universe expands with decelerated rate.

The kinetic term is given by

$$\dot{\phi}^2(t) = \left(\frac{4}{3} - \rho_{m0} \right) \frac{1}{t^2} + \frac{16\alpha}{t^4} \quad \left(\rho_{m0} < \frac{4}{3} \right), \quad (42)$$

Integrating (42), we get

$$\phi(t) - \phi_2 = \sqrt{C} \left[\log \left\{ 2Ct \left(1 + \sqrt{1 + \frac{16\alpha}{Ct^2}} \right) \right\} - \sqrt{1 + \frac{16\alpha}{Ct^2}} \right], \quad (43)$$

where ϕ_2 is a constant of integration and $C = (4 - 3\rho_{m0})/3$.

The scalar potential is

$$V(t) = \left(\frac{4 - 3\rho_{m0}}{6} \right) \frac{1}{t^2}. \quad (44)$$

One may observe that scalar field ϕ contains the term of coupling parameter α but scalar potential V is independent from higher derivative term. The behavior of scalar potential is similar to the Einstein gravity during the matter-dominated phase.

In this case, the scalar field density and pressure are respectively given as

$$\rho_\phi = \left(\frac{4}{3} - \rho_{m0}\right) \frac{1}{t^2} + \frac{8\alpha}{t^4}, \quad (45)$$

$$p_\phi = \frac{8\alpha}{t^4}. \quad (46)$$

Therefore, the EoS parameters for scalar field is given by

$$\omega_\phi = \frac{\frac{8\alpha}{t^4}}{\left(\frac{4}{3} - \rho_{m0}\right) \frac{1}{t^2} + \frac{8\alpha}{t^4}}, \quad (47)$$

Both the physical quantities, ρ_ϕ and p_ϕ are decreasing function of time. As $t \rightarrow 0$, we have $\omega_\phi = 1$, i.e., the scalar field cosmology goes to the solution of stiff matter ($p_\phi = \rho_\phi$). As $t \rightarrow \infty$, we get $\omega_\phi = 0$, which is same as ω of matter in the case of matter-dominated phase. The scalar field behaves as stiff matter at early time but in late time it behaves as matter in matter-dominated. The scalar field does not inflate the universe during the matter-dominated era even if $\alpha \neq 0$ of HD theory.

3.4 Solution with $\omega = -1/2$ and $n = 4/3$

In this case, we get $p_m = -\rho_m/2$, where $a \sim t^{4/3}$ and $\rho_m \sim 1/t^2$.

From (24), we have

$$\dot{\phi}^2(t) = \left(\frac{8}{3} - \frac{\rho_{m0}}{2}\right) \frac{1}{t^2} + \frac{160\alpha}{t^4} \quad \left(\rho_{m0} < \frac{16}{3}\right), \quad (48)$$

which on integration, we get

$$\phi(t) - \phi_3 = \sqrt{D} \left[\log \left\{ 2Dt \left(1 + \sqrt{1 + \frac{72\alpha}{Dt^2}} \right) \right\} - \sqrt{1 + \frac{72\alpha}{Dt^2}} \right], \quad (49)$$

where ϕ_3 is integration constant and $D = (16 - 3\rho_{m0})/6$.

From (25), we get

$$V(t) = \left(4 - \frac{3\rho_{m0}}{4}\right) \frac{1}{t^2} + \frac{80\alpha}{t^4} \quad (50)$$

From (49) and (50) it is observed that both scalar field and scalar potential depend on the coupling parameter associated with the higher derivative term. It is observed that $q = -0.25$ which reveals the case of quintessence phase of the accelerating universe. The solution obtained here describes a universe which is accelerating and compatible with the recent Ia supernova observations [1–3]. Let us see whether the acceleration is due to HD theory.

Equations (21) and (27) give

$$\rho_\phi = \left(\frac{16}{3} - \rho_{m0}\right) \frac{1}{t^2} + \frac{160\alpha}{t^4}, \quad (51)$$

$$p_\phi = -\frac{1}{2} \left(\frac{16}{3} - \rho_{m0}\right) \frac{1}{t^2}. \quad (52)$$

Fig. 2 Scalar field $\phi(t)$ versus time t with $\phi_0 = \phi_1 = \phi_2 = \phi_3 = 0$, $\alpha = 2$ and $\rho_{m0} = 2/3$

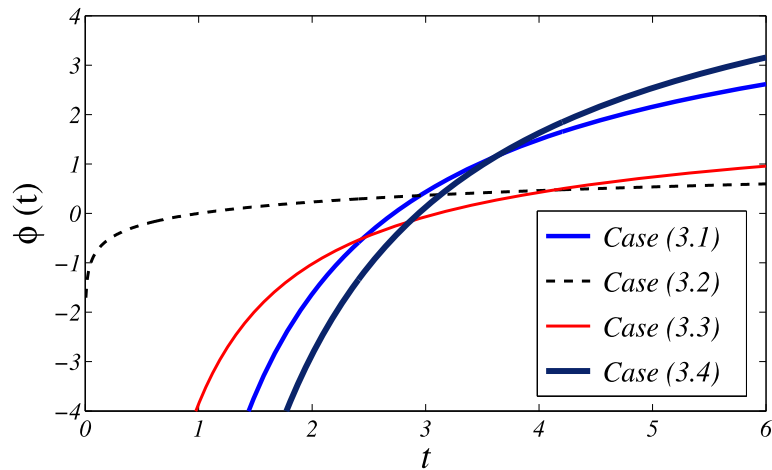
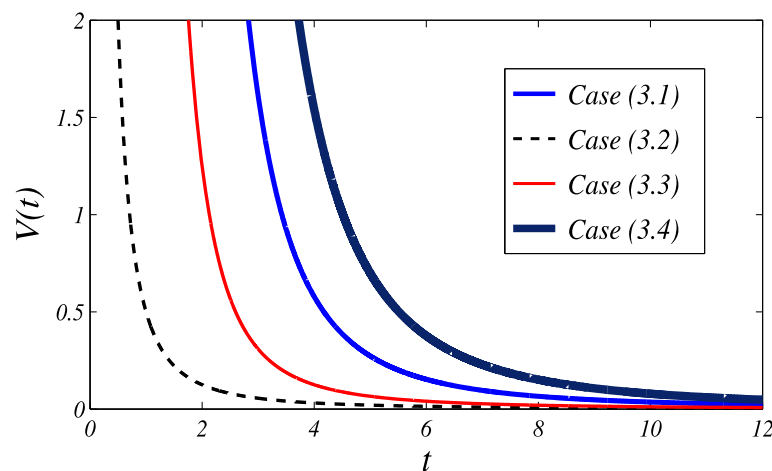


Fig. 3 Scalar potential $V(t)$ versus time t with $\alpha = 2$ and $\rho_{m0} = 2/3$



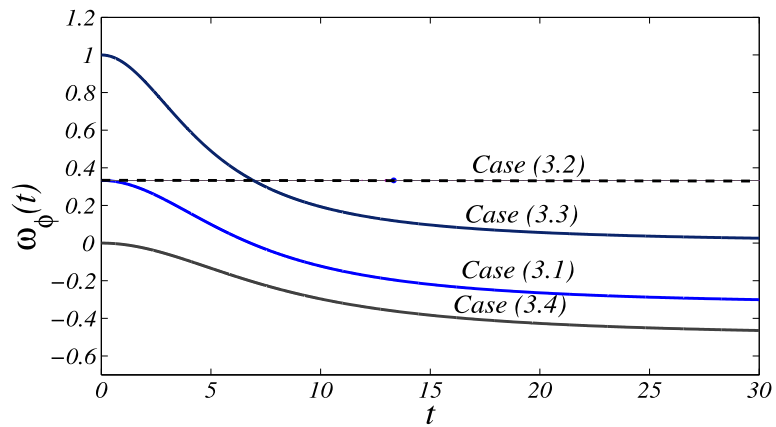
The scalar field EoS parameters is given by

$$\omega_\phi = \frac{-\frac{1}{2}(\frac{16}{3} - \rho_{m0})\frac{1}{t^2}}{(\frac{16}{3} - \rho_{m0})\frac{1}{t^2} + \frac{160\alpha}{t^4}}. \quad (53)$$

As $t \rightarrow 0$, we get $\omega_\phi = 0$ and as $t \rightarrow \infty$, we have $\omega_\phi = -1/2$, i.e., quintessence model ($\omega_\phi > -1$). The scalar field and perfect fluid have the same behavior at late time which accelerate the universe. We observe that the pressure, which is negative, does not contain the higher derivative term. It means that the higher derivative theory disappears at late time and it is only the hypothetical fluid, which has negative pressure, is responsible to give rise the accelerated expansion of the universe. The HD theory is not responsible to give rise the late time acceleration as we know that R^2 corrections become negligible for $t \rightarrow \infty$, it is only natural that the resulting equation of state for ϕ -component approaches that for matter.

Figures 2 and 3 plot scalar field $\phi(t)$ and scalar potential $V(t)$ with time t , respectively for the above discussed different phases of the universe. In Fig. 2, we observe that the scalar field increases with time with decelerated rate during all phases of the universe. However, in radiation-dominated phase it increases with more decelerated rate due to the absence of higher derivative term. In Fig. 3, the scalar field potential decreases gradually with time in inflationary phase, matter-dominated phase and accelerated phase as compared to the radiation-dominated phase where it behaves as general relativity. It decreases fast in radiation-dominated phase due to the absence of higher derivative term. Hence, the higher

Fig. 4 EoS of scalar field $\omega_\phi(t)$ versus time t with $\alpha = 2$ and $\rho_{m0} = 2/3$



derivative theory does not effect the behavior of scalar potential and scalar field in this phase. One gets the similar behavior to the Einstein gravity as shown in case (3.2) of Figs. 2 and 3.

Figure 4 plots $\omega_\phi(t)$ with t for certain values of the arbitrary constants for different phases of the universe. We can see that $\omega_\phi = \omega$ in the limit of $t \rightarrow \infty$ in all cases as discussed above since the R^2 corrections are negligible at late time which is consistent with the power-law assumption of scale factor.

4 Conclusion

We have studied cosmological scenarios obtained from a gravity model containing higher derivative terms in the curvature, a self-interacting scalar field and matter. A flat FRW metric is used, and solutions under the form of power-law are determined. Exact solution for scalar field density, scalar potential and some other parameters have been obtained for decelerated and accelerated phases of the universe. We have observed that the power-law cosmology is compatible with observations since it gives constant value of deceleration parameter to describe the decelerated and accelerated universes.

The field equations have been solved exactly for different phases of the evolution of the universe. During different phases of the universe we have noted that the physical quantities have the higher order term in inflationary, matter-dominated and accelerated phases whereas the higher derivative theory does not effect the behavior of the physical quantities in radiation-dominated phase. In this case we have obtained the solution similar to Einstein theory for the flat universe. We have observed that the scalar potential decreases gradually in inflationary, matter and accelerated phases than the radiation-dominated phase as shown in Fig. 3.

The model decelerates during radiation and matter-dominated phases ($0 < n < 1$) even in the presence of higher derivative terms. In case of $\omega = -1/2$; $n = 4/3$, i.e., in power law inflation it is observed that the HD theory is not responsible for late time acceleration of the universe. The late time acceleration is caused by the hypothetical fluid, which has negative pressure to give rise the accelerated expansion at late time where the higher gravity correction disappears. The scalar field act as a quintessence field at late time of the evolution of the universe. Therefore, the HD theory is useful to study the model in early time of the evolution of the universe. The parameter α when set equal to zero one gets the solution similar to the Einstein gravity in all the phases of the universe. In the absence of matter, the solutions reduce to the corresponding ones obtained by Paul [34] and further the case $\alpha = 0$ was discussed by Ellis and Madsen [29]. Thus, we conclude that the HD theory has its own significance to understand the behavior of the universe in the past and present.

References

1. Perlmutter, S., et al.: *Astrophys. J.* **517**, 565 (1999)
2. Riess, A.G., et al.: *Astrophys. J.* **560**, 49 (2001)
3. Garavich, P.M., et al.: *Astrophys. J.* **509**, 74 (1998)
4. Brans, C., Dicke, R.H.: *Phys. Rev.* **124**, 925 (1961)
5. Bergmann, P.G.: *Int. J. Theor. Phys.* **1**, 25 (1968)
6. Nerved, K.: *Astrophys. J.* **161**, 1059 (1970)
7. Wagoner, R.V.: *Phys. Rev. D* **1**, 3209 (1970)
8. Utiyama, R., De Witt, B.S.: *J. Math. Phys.* **3**, 608 (1962)
9. Stella, K.: *Gen. Relativ. Gravit.* **9**, 353 (1978)
10. Whitt, B.: *Phys. Lett. B* **145**, 176 (1984)
11. Utiyama, R.: *Prog. Theor. Phys.* **72**, 83 (1984)
12. Suen, W.M., Anderson, R.P.: *Phys. Rev. D* **35**, 2940 (1987)
13. Starobinsky, A.: *Phys. Lett. B* **91**, 99 (1980)
14. Guth, A.H.: *Phys. Rev. D* **23**, 347 (1981)
15. Nojiri, S., Odintsov, S.D.: *Phys. Rev. D* **77**, 026007 (2008)
16. Copeland, E.J., Sami, M., Tsujikawa, S.: *Int. J. Mod. Phys. D* **15**, 1753 (2006)
17. Billyard, A.P., Coley, A.A., Vanden Hoogen, R.J., Ibáñez, J., Olasagasti, I.: *Class. Quantum Gravity* **16**, 4035 (1999)
18. Copeland, E.J., Liddle, A.R., Wands, D.: *Phys. Rev. D* **57**, 4686 (1998)
19. Chimento, L.P., Jakubi, A.S.: *Int. J. Mod. Phys. D* **5**, 71 (1996)
20. Barrow, J.D.: *Class. Quantum Gravity* **10**, 279 (1993)
21. Chimento, L.P., Cossarini, A.E.: *Class. Quantum Gravity* **11**, 1177 (1994)
22. Kenmoku, M., Otsuki, K., Shigemoto, K., Uehara, K.: *Class. Quantum Gravity* **13**, 1751 (1996)
23. Paul, B.C., Mukherjee, S., Beesham, A.: *Mod Phys. D* **7**, 499 (1998)
24. Singh, G.P., Beesham, A., Deshpande, R.V.: *Pramana J. Phys.* **54**, 729 (2000)
25. Debnath, P.S., Paul, B.C.: *Int. J. Mod. Phys. D* **15**, 189 (2006)
26. Paul, B.C., Mukherjee, S.: *Int. J. Mod. Phys. D* **7**, 499 (1998)
27. Debnath, P.S., Paul, B.C.: *Phys. Rev. D* **76**, 123505 (2007)
28. Paul, B.C., Debnath, P.S.: [arXiv:1105.3307](https://arxiv.org/abs/1105.3307) [gr-qc]
29. Ellis, G.F.R., Madsen, M.S.: *Class. Quantum Gravity* **8**, 667 (1991)
30. Barrow, J.D., Saich, P.: *Class. Quantum Gravity* **10**, 279 (1993)
31. Barrow, J.D., Mimoso, J.P.: *Phys. Rev. D* **50**, 3746 (1994)
32. Mimoso, J.P., Wands, D.: *Phys. Rev. D* **51**, 477 (1995)
33. Banerjee, N., Sen, S.: *Phys. Rev. D* **57**, 4614 (1998)
34. Paul, B.C.: *Pramana J. Phys.* **53**, 833 (1999)
35. Singh Ibotombi, N., Singh, S.S., Devi, S.R.: *Astrophys. Space Sci.* **334**, 187 (2011)

Studies of Novel Chain Linked Biodegradable Polymers

A. P. Gupta · Anshu Dev · Vimal Kumar

© Springer Science+Business Media, LLC 2011

Abstract The synthesis of high-molecular-weight lactic acid based polymers by chain linked polymerization was investigated. Lactic acid based hydroxyl terminated telechelic prepolymer was synthesized and then the molecular weight was increased by chain linked polymerization using methylene diphenyldiisocyanate. All polymerizations were carried out in the melt, using tin octoate as catalyst. The products were characterized by Differential scanning calorimetry, nuclear magnetic resonance spectroscopy and size exclusion chromatography. With the increase in diisocyanate concentration, an increase in the glass transition temperature, molecular weight and molecular weight distribution was observed.

Keywords Biodegradable · Lactic acid · Chain linked polymer · Dynamic mechanical analysis

Introduction

Now a day's biodegradable materials are of prime interest for both environmental reasons and biomedical applications. Lactic acid is an attractive monomer in the synthesis of biodegradable polymers, being obtained from renewable resource. The polymer thus obtained i.e. polylactic acid (PLA) has wide number of applications on the basis of its properties. The degradation time for PLA varies from 2 months to 1 year in addition to good mechanical properties. Processing by conventional thermoplastic methods

like injection molding, thermoforming etc. make it an attractive alternative to the non-biodegradable plastics. In last few decades PLA have been studied extensively for a number of applications [1, 2]. To have good mechanical strength PLA should possess high molecular weight. Direct polycondensation of lactic acid is a low cost process to produce PLA; although a high-molecular-weight polymer cannot be produced by this method because of difficulty of removal of water from the polymerization reaction [3]. Furthermore, during the polycondensation, the molecular weight of poly (lactic acid) is reduced by depolymerization and other side reaction at higher temperature. On the other hand high molecular weight PLA is usually produced by the ring opening polymerization of lactide which is the dilactone of lactic acid [4] and synthesized from thermal cracking of low molecular weight PLA at higher temperature and low pressure. This process requires high energy and longer reaction time.

The chain coupling of low molecular weight PLA using chain extender can be a better alternative to obtain a polymer with high molecular weight [5]. These chain extension reaction are economically advantageous because they can be carried out in the melt, with only low concentration of chain extending agents, and because separate purification step are not required. Improved mechanical properties and the flexibility to manufacture copolymer with different co-monomers are other benefits of the use of chain extending agent. Typically chain extenders for polyesters, which contain -OH and -COOH groups, are diisocyanates, diepoxides, diboxzolines, dianhydride and bisketeneacetals. The very high reactivity of isocyanates has encouraged their use for coupling and chain extension of oligomers [6–8]. The self-condensation of lactic acid yields a glassy low molecular weight polymer with an equimolar concentration of hydroxyl and carboxyl end-groups. To achieve maximum molecular weight, both types of end group of the polymer need to be utilised. A difunctional

A. P. Gupta · A. Dev · V. Kumar (✉)
Department of Applied Chemistry and Polymer Technology,
Delhi College of Engineering, Faculty of Technology, University
of Delhi, Delhi 110042, India
e-mail: vimalkumar.7@gmail.com

prepolymer can be synthesised by modifying PLA oligomer by using small amount of di or multifunctional hydroxyl or carboxyl compounds so that they are solely hydroxyl or carboxyl terminated [9]; which can be further chain extended with the use of single type of chain extender. Moreover chain linked polymerization do not interfere with the biodegradable behaviour of the resulting polymer. Hetero-chain polymers, particularly those containing oxygen and/or nitrogen atoms in the main chain, are generally susceptible to hydrolysis. For hydrolysis to occur, the polymer must contain hydrolytically unstable bonds such as ester, amide, or urethane, and show some degree of hydrophilicity, as is the case with PEUs and PEAs [10, 11].

Different work can be seen in the literature for chain linking polymerization of lactic acid, however these works are mainly emphasized on the increase in the molecular weight and other properties but not the stoichiometry, even most of the work is based on NCO/OH ration above stoichiometry [3, 12–14]. Few authors have used different reactants like BOX or DL mentalic acid during the chain extension polymerization [15, 16]. Zhong et al. [13] study the chain linking polymerization with HDI with both hydroxyl and carboxyl chain ends results the formation of urethane linkage and amide formation. Cohn et al. [17] have investigated the chain linked polymerization with emphasizing on ratio of poly(ethylene oxide)/poly(L-lactic acid). Different author have studied various parameter of chain extension polymerization [5, 18] however to best of our knowledge the stoichiometry of PLA-PEG/MDI have not yet been emphasised.

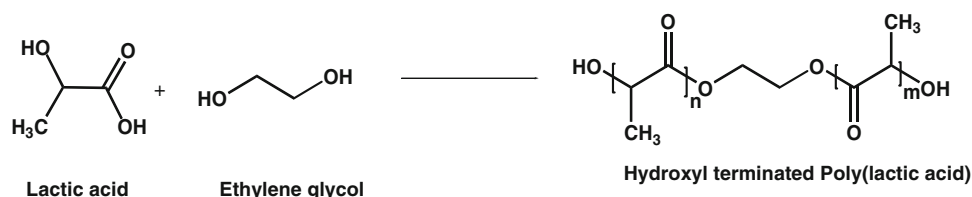
PLA is a rather brittle and rigid polymer, chain-linking by urethane linkage will make the polymer more brittle therefore; polyethylene glycol have been introduced in the polymer chain to increase the flexibility [19]. In the present work, the lactic acid was condensation-polymerized to a low-molecular-weight polymer which contains hydroxyl end group. In the second step, this polymer chains were joined together using difunctional linkers i.e., diisocyanates to get a polymer of higher molecular weight [8, 20].

Experimental

Material

Lactic acid (90% aqueous solution) was purchased from Merck, ethylene glycol and polyethylene glycol (6,000)

Fig. 1 Synthesis of hydroxyl terminated poly (lactic acid)



from Thomas Baker, tin octoate from Sigma Aldrich, chloroform from Thomas Baker was distilled over calcium chloride before used. Methylene diphenyldiisocyanate (MDI) from BASF was used as received.

Synthesis of Hydroxyl Terminated Poly (Lactic Acid) (HTPLA)

Polymerization was carried out in 250 mL round bottom flask with stirrer fitted with nitrogen purge assembly over thermostatic controlled heating. Water was removed from the lactic acid aqueous solution at 100 °C under reduced pressure for 4 h. Lactic acid based telechelic prepolymer was synthesized using ethylene glycol as diol and tin octoate as catalyst at 200 °C under the constant flow of nitrogen (Fig. 1). After 48 h polymer was put in aluminium tray and cooled over calcium carbonate. The polymer was placed in desiccator till further use. Acid value was found as 7.

Synthesis of Chain Linked Poly (Lactic Acid) (CLPLA)

Polymerization of CLPLA was carried out in 100 mL round bottom flask with stirrer and thermostatic controlled heating in melt under nitrogen blanket using PLAol with 20% (w/w of PLAol) polyethylene glycol and desired amount MDI (Fig. 2). The amount of MDI was calculated on theoretical basis of hydroxyl number and isocyanate content of MDI, where OH and NCO groups was calculate by titration using phthalic anhydride and dibutylamine respectively (Table 1). A yellowish polymer obtained was placed in desiccators till further use.

Measurements

Differential scanning calorimetry (DSC) was performed on a TA Q20 differential scanning calorimeter under a nitrogen atmosphere. The samples for DSC was weighed (~10 mg) on a small aluminum pan, followed by sealing the pan. The samples were scanned up to 190 °C at heating rate of 10 °C/min, Glass transition temperature (T_g) was taken at the mid-point of the T_g curve.

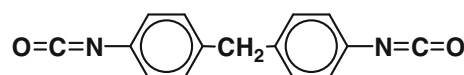


Fig. 2 Methylen diphenyldiisocyanate (MDI)

Table 1 OH/NCO ratio for polymer

Samples	NCO/OH ratio
CLPLA-1	0.8
CLPLA-2	1.0
CLPLA-3	1.2

Nuclear magnetic resonance (NMR) spectra were recorded on a Bruker Advanced II (400 MHz for proton) spectrometer using CDCl_3 and DMSO as a solvent for HTPLA and CLPLA respectively.

Molecular weights were determined by room temperature size exclusion chromatography (SEC) Perkin Elmer Series 200 Refractive Index detector. THF was used as solvent and eluent. The samples were filtered through a 0.5 μm filter. Monodisperse polystyrene standards were used for primary calibration, which means that the Mark Houwink constants were not used.

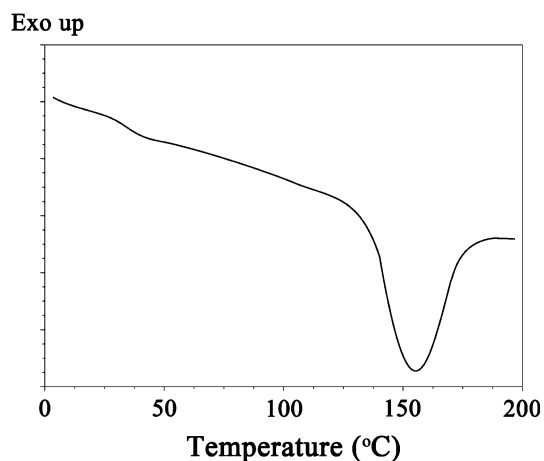
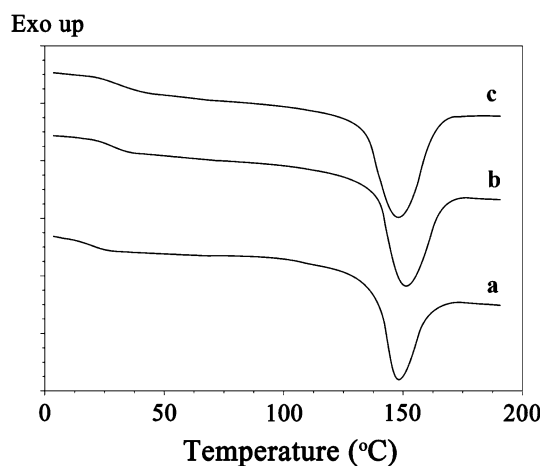
Result and Discussion

Differential Scanning Calorimetry

DSC results shows in a regular increase trend in the glass transition temperature of CLPLA. It was observed that an increase in the glass transition temperature (T_g) with the increase in MDI ratio (Table 2). Since, the molecular motions in CLPLA are dependent on the domain distribution of both hard and soft segments as well as the presence of urethane groups, with high polarity, increases the T_g . However, the CLPLA-1 showed a lower T_g than HTPLA, this is because of the plasticizing effect of the PEG (Fig. 3). In case of CLPLA-2, chain linkage had taken place resulted an increase in T_g . In case of CLPLA-3, additional MDI resulted in the crosslinking between different polymer chains making the polymer stiffer with higher T_g . T_g was increased from 20.2 to 32.8 $^{\circ}\text{C}$. No peak for the crystallization was observed in the single scan DSC thermogram (Fig. 4). Whereas melting was found irrespective of the ratio of MDI used.

Table 2 Glass transition temperature of CLPLA

Samples	T_g ($^{\circ}\text{C}$)	T_m ($^{\circ}\text{C}$)
HTPLA	36.1	156
CLPLA-1	20.2	148
CLPLA-2	31.2	152
CLPLA-3	32.8	148

**Fig. 3** Differential scanning calorimetry thermogram of HTPLA**Fig. 4** Differential scanning calorimetry thermogram of **a** CLPLA-1 **b** CLPLA-2 **c** CLPLA-3

Nuclear Magnetic Resonance (NMR) Spectroscopy

To study the reaction between isocyanate and hydroxyl group, lactic acid prepolymer (hydroxyl terminated polylactic acid having hydroxyl group at both ends of the polymer chain) were allowed to react with MDI in the different ratios. Figure 5 shows the ^1H -NMR spectrum of HT-PLA and CL-PLA. ^1H NMR spectra exhibited the signal of methine group at 5.1 ppm and the signal of methyl group at 1.5 ppm. The signal at 4.5 ppm characteristic of the hydrogen of methine group next to a hydroxyl end group was observed. However, the signal at 4.5 ppm was not observed in the spectra of all CL-PLA because MDI reacted with hydroxyl end groups of HT-PLA. Signals at 4.4 ppm are observed in due to $-\text{CH}_2-$ for PEG. The reactions of MDI with hydroxyl end group can be seen more clearly in the region 4.5–3.5 ppm. The formation of amide bonds can be seen as a broad peak at 6.21 ppm in

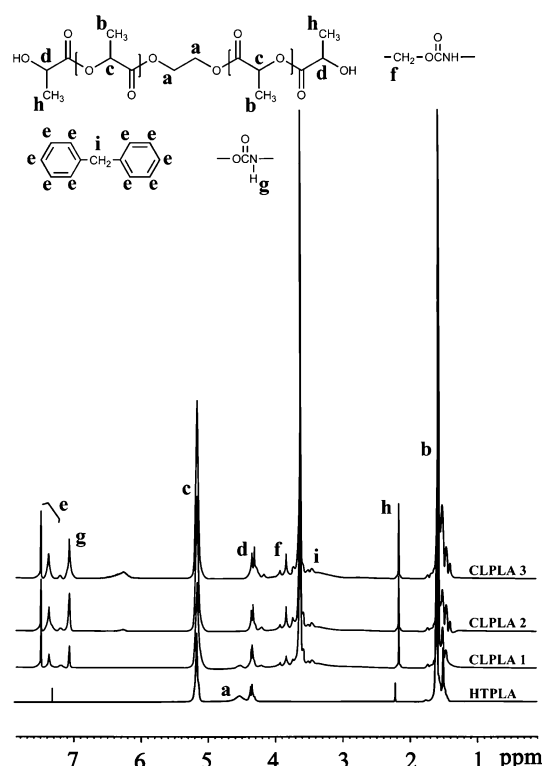


Fig. 5 ^1H -NMR of the HTPLA and CLPLA

CLPLA-2 and CLPLA-3. The chemical shift of hydrogen of the urethane bond formed by reaction of MDI with hydroxyl end group was observed at 7.0 ppm and the methin group next to urethane are observed at 3.8 ppm for all CLPLA. The signals at 7.5, 7.4 and 3.5 ppm in the spectrum of all CL-PLA were assigned to the units of MDI. In addition, some indications of side reactions, such as formation of allopanates and urea group in CLPLA-3, i.e. branching of the polymer was observed at broad shoulder on the NH peak at 6.50–6.26 ppm.

Size Exclusion Chromatography (SEC)

Molecular-weight measurements were done by SEC. The molecular weights and molecular weight distributions ($M\bar{n}/M\bar{w}$) were calculated. THF was used as an eluent. SEC results show the number average molecular weight of HT-PLA was 5,267, weight average molecular weight was 8,683 and polydispersity was 1.78 (Fig. 6).

After the chain linked polymerization a regular increasing trend in the number average molecular weight, weight average molecular weight and polymer discpensity was observed. This is because of the higher concentration of MDI. As the concentration of MDI increases in the polymer more hydroxyl chain ends are reacted to form a longer polymer chain. The number average molecular weight of the resulting polymer was increased to 36 K,

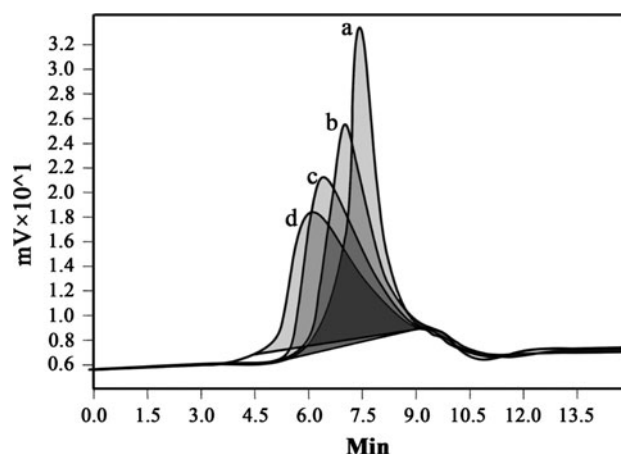


Fig. 6 SEC chromatogram of a HTPLA b CLPLA-1 c CLPLA-2 d CLPLA-3

Table 3 SEC results for the chain linked polymers

Samples	$M\bar{n}$	$M\bar{w}$	$M\bar{n}/M\bar{w}$
HTPLA	4,872	5,740	1.1
CLPLA-1	9,540	18,555	1.9
CLPLA-2	24,825	63,328	2.6
CLPLA-3	36,241	103,649	2.9

weight average molecular weight to 103 K and polydispersity to 2.9 (Table 3). It shows that the low molecular weight chain are linked together results an increase in the molecular weight of the final polymer.

Conclusion

This study investigated the sequential and simultaneous addition of highly reactive chain extender, MDI, for the chain linking of HTPLA. The development of polymer structure during polymerization and the reaction behavior of the different functional groups were characterized by NMR. The chain linked polymer shows an increase in the T_g value and SEC also show an increasing trend in the molecular weight of the resulting polymer. The results indicate that these increase in the properties of the resulting CLPLA very much depends on the ratio of MDI to HTPLA. As a conclusion from the present and our earlier work, we can state that at stoichiometry we get the maximum improvement in T_g and high molecular weight without crosslinking in the polymer structure. Above stoichiometry, crosslinking as allopanates linkage was observed. The chain linked polymerization not only allows the preparation of high molecular weight polymer with improved thermal and mechanical properties, but provides

the possibilities for variation in the polymer structure (like branching). This method also allows the introduction of different groups into PLA chain, which affects the properties of the final polymer.

Acknowledgments Authors acknowledge the support of the SAIF facility at Punjab University for the NMR studies and SICART-CVM, VV Nagar for the SEC studies.

References

- Gupta AP, Kumar V (2007) *Eur Polym J* 43(10):4053
- Dutta J, Dutta PK (2006) *Everyman's Sci XLI*(2):103
- Woo SI, Kim BO, Jun HS, Chang HN (1995) *Polym Bull* 35(4):415
- Kricheldorf HR, Kreiser-Saunders I, Boettcher C (1995) *Polymer* 36(6):1253
- Hiltunen K, Seppala JV, Harkonen M (1997) *J Appl Polym Sci* 63(8):1091
- Pitt CG, Gu Z-W, Ingram P, Hendren RW (1987) *J Polym Sci A Polym Chem* 25(4):955
- Storey RF, Wiggins JS, Puckett AD (1994) *J Polym Sci A Polym Chem* 32(12):2345
- Hiltunen K, Seppala JV, Harkonen M (1997) *J Appl Polym Sci* 64(5):865
- Hiltunen K, Harkonen M, Seppala JV, Vaananen T (1996) *Macromolecules* 29(27):8677
- Tuominen J, Kylma J, Kapanen A, Venelampi O, Itävaara M, Seppälä J (2002) *Biomacromolecules* 3(3):445
- Rehman I, Andrews EH, Smith R (1996) *J Mater Sci Mater in Med* 7(1):17
- Kylma J, Tuominen J, Helminen A, Seppala J (2001) *Polymer* 42(8):3333
- Zhong W, Ge J, Gu Z, Li W, Chen X, Zang Y, Yang Y (1999) *J Appl Polym Sci* 74(10):2546
- Gu SY, Yang M, Yu T, Ren TB, Ren J (2008) *Polym Int* 57(8):982
- Tuominen J, Kylma J, Seppala J (2002) *Polymer* 43(1):3
- Kylma J, Harkonen M, Seppala JV (1997) *J Appl Polym Sci* 63(13):1865
- Cohn D, Hotohely-Salomon A (2005) *Polymer* 46(7):2068
- Borda J, Bodnar I, Keki S, Sipos L, Zsuga M (2000) *J Polym Sci A Polym Chem* 38(16):2925
- Baiardo M, Frisoni G, Scandola M, Rimelen M, Lips D, Ruffieux K, Wintermantel E (2003) *J Appl Polym Sci* 90(7):1731
- Gupta AP, Kumar V (2010) *Des Monomers Polym* 13(1):65